CORRECTION METHODS FOR THE QUANTITATIVE EVALUATION OF THERMAL NEUTRON TOMOGRAPHY

A dissertation submitted to the

SWISS FEDERAL INSTITUTE OF TECHNOLOGY ZURICH

for the degree of

Doctor of Sciences

presented by

RENÉ KARIM HASSANEIN

Dipl. Phys. ETH

born June 14, 1966
citizen of Frauenfeld, TG

accepted on the recommendation of
Prof. Dr. Hannes Flühler, examiner
Dr. Eberhard Lehmann, co-examiner
Prof. Dr. Peter Böni, co-examiner

2006

Acknowledgements

First, I thank my PhD supervisor Hannes Flühler for the cordial admission into the soil physics group and for providing me permanently and patiently with physical knowledge, ideas and enthusiasm. Thanks to the always perfectly prepared experiments of Peter Lehmann, Andrea Carminati, Anders Kaestner and Massimo Guglielmetti, I always had enough "test" samples available and a steady motivation to make the quantifications perfect. Due to them, also a close collaboration with Insa Neuweiler, Milos Vasin and Azad Koliji has been established, that has resulted finally in very successful experiments.

Of course, I could carry out the PhD thesis only thanks to the cooperation with the Neutron Imaging Group NIAG and the exchange of ideas and measurements with other radiography groups. Particularly, I thank Eberhard Lehmann and Peter Vontobel for offering me the PhD position in the NIAG and for the many constructive discussions and suggestions. However, without the help of Gabriel Frei and George Necola, I could have performed not a single experiment. I thank also Guido Kühne for being a pleasant office mate and for the fruitful discussions about the neutron spectra and their interpretation.

Especially I thank for the possibilities to visit all the conferences, workshops and courses at home and abroad. A highlight have been the measurements at the Technische Universität München, where I was received frankly and cordially – thanks to the whole ANTARES team and Peter Böni. Also the exchange of ideas and measurements with Frikkie de Beer and Nikolay Kardjilov has been very productive. All these activities have been possible only due to support by the Swiss National Science Foundation.

I thank all my friends, who have accompanied me during my time as a PhD student and who have been there also in hard times. They have given me the necessary strength and much pleasure. Finally, I thank my parents, brothers and sisters for encouraging me during all the educations and understanding my decisions.

Zusammenfassung

Die thermische Neutronenradiographie und -tomographie hat sich als Methode für die zerstörungsfreie Prüfung von Materialien in den letzten Jahren bewährt. Die rein qualitative Betrachtung hat schon wertvolle Ergebnisse geliefert, vor allem weil Materialien (z.B. Metalle) durchdrungen werden können, die für Röntgenstrahlung undurchsichtig sind. Umgekehrt ist die Empfindlichkeit für gewisse leichte Elemente (z.B. Wasserstoff) sehr gross, die für die Röntgenstrahlung praktisch nicht sichtbar sind. Häufig sind die Anwender jedoch nicht nur an qualitativen sondern auch an quantitativen Aussagen interessiert. In der Bodenphysik beispielsweise ist der Wassergehalt in der Bodenstruktur mit einer hohen räumlichen Auflösung wichtig für die Untersuchung des Stofftransports. Dank den heutzutage verwendeten digitalen Detektorsystemen sind solche Auswertungen grundsätzlich möglich, da die Radiographien als Graustufenbilder dargestellt werden, deren Grauwert proportional zum einfallenden Neutronenfluss ist.

Trotzdem sind genaue Aussagen über den Materialgehalt einer Probe nicht leicht zu machen, da das exponentielle Abschwächungsgesetz für den Neutronenfluss nur in erster Näherung stimmt. Es gibt einige Effekte, die dieses einfache Gesetz verzerren oder ihm überlagert sind.

Die Hauptursache für diese Abweichungen ist, dass die Neutronen von den Atomen nicht nur absorbiert oder ungestört durchdrungen, sondern auch gestreut werden können. Viele relevante Materialien (z.B. Wasser) haben sogar eine viel höhere Wahrscheinlichkeit für Streuung als für Absorption. Die gestreuten Neutronen können auf den Detektor treffen, wo sie für einen zu hohen Messwert sorgen. Diese scheinbar hohe Transmission wird als zu geringe Dicke oder Dichte der gemessenen Probe interpretiert.

Ein weiterer Grund für die Abweichung vom exponentiellen Schwächungsgesetz ist das polyenergetische Spektrum des Neutronenstrahls. Da im thermischen Bereich die meisten Wirkungsquerschnitte für tiefere Energien zunehmen, kann für

diese kein allgemein gültiger Wert angegeben werden. Ebenso sind die Wirkungs-
querschnitte der Detektormaterialien energieabhängig. Diese spektralen Effekte
beeinflussen den effektiven Wirkungsquerschnitt, mit dem aus dem gemessenen
Neutronenfluss die quantitative Massendichte berechnet wird.

Damit diese störenden Effekte korrigiert werden können, müssen die Eigen-
schaften der experimentellen Anordnung bekannt sein. Für die Charakterisierung
des Neutronenstrahls ist vor allem das Energiespektrum wichtig, aber auch die
Strahlintensität und ihre räumliche Verteilung spielen eine Rolle für die erwarteten
Fehler. Und auch die Eigenschaften des Detektorsystems müssen bekannt sein.
Je nach Fragestellung des Experiments muss der geeignete Detektor gewählt wer-
den. Die hauptsächlichen Kriterien sind die räumlichen resp. zeitlichen Auflöse-
vermögen, zwischen denen ein Kompromiss gefunden werden muss. Für die Quan-
tifizierung der Radiographien ist vor allem die energieabhängige Absorptionsrate
und auch das Signal-Rausch-Verhältnis wichtig.

Die Verfälschung der reinen Transmissionswerte durch die Streuung wird korri-
giert, indem der Streuanteil berechnet und von der Radiographie subtrahiert wird.
Dazu muss die Streuung nach dem Entstehungsort in Hintergrund- und Proben-
streuung unterteilt werden. Die Hintergrundstreuung umfasst diejenigen Neutro-
nen, die an der Probe vorbeifliegen oder sie ungestört durchdringen und von der
Umgebung der Probe (z.B. Kamerabox) oder der Abschirmung auf den Detektor
gestreut werden. Die Probenstreuung besteht aus den Neutronen, die in der Probe
selbst gestreut werden und auf den Detektor treffen.

Die Hintergrundstreuung kann zu einem grossen Teil durch einen geeigneten ex-
perimentellen Aufbau vermieden werden. Um den verbleibenden Teil abschätzen zu
können, wird in einer Zusatzmessung die Probe durch einen Körper ersetzt, der für
Neutronen undurchdringlich ist. Der hinter diesem schwarzen Körper gemessene
Neutronenfluss wird der Hintergrundstreuung zugeschrieben. Er wird auf die In-
tensität der Probenradiographie skaliert und von dieser subtrahiert.

Für die Korrektur der Probenstreuung werden "Point Scattered Functions"
(PScF) mit Monte-Carlo-Simulationen berechnet. Diese beschreiben die Streuver-
teilung, die ein Neutronenstrahl aus einer Punktquelle beim Durchdringen einer
Materialschicht verursacht. Sie sind vom Neutronenspektrum, dem Probenmateri-
al, der Schichtdicke, dem Detektortyp und dem Proben-Detektor-Abstand abhän-
gig. Die PScF werden anhand der Massendichte von der Auswertung der unkor-
rigierten Radiographie gewählt, zur gesamten Probenstreuung hinter allen Bild-
punkten der Radiographie überlagert und von der ursprünglichen Radiographie

subtrahiert. So wird die Probenstreuung in einem iterativen Prozess mehrmals aus der immer genauer korrigierten Radiographie berechnet und subtrahiert.

Für die Korrektur der spektralen Effekte können ebenfalls die oben erwähnten Simulationen für die PScF verwendet werden. Sie liefern als Ergebnis auch die erwarteten Transmissionswerte für die Schichtdicken. Mit diesen Dicke-Transmission-Paaren als Referenzwerten wird auf die durchstrahlte Massendichte geschlossen, nachdem die Streuanteile von der Radiographie abgezogen worden sind.

Der Korrekturalgorithmus ist in Versuchen mit bekannten Proben getestet worden und erbringt Resultate, die auf ca. $\pm 5\,\%$ genau sind. Auch bei relevanten wissenschaftlichen und industriellen Experimenten ist der Algorithmus angewendet worden und hat verlässliche quantitative Materialgehalte geliefert. Die Korrekturmethode ist auch an weiteren Anlagen in München, Pretoria und Berlin erfolgreich getestet worden. Wenn die Anlageeigenschaften bekannt sind und dem Simulationsprogramm für die PScF und Transmissionswerte genaue Querschnittdaten zugrunde liegen, können die Radiographien mit derselben Genauigkeit quantifiziert werden wie an NEUTRA, wo der Algorithmus entwickelt worden ist.

Der Aufwand, den Algorithmus anzuwenden, hält sich in Grenzen, da einmal berechnete PScF für spätere Messungen immer wieder verwendet werden können. Auch die Rechenzeit von ca. 5 bis 30 s für die Korrektur einer Radiographie ist etwa gleich wie deren Aufnahmezeit. Damit steht ein Werkzeug zur Verfügung, das die quantitative Auswertung von Neutronenradiographien und -tomographien nach Materialgehalten erlaubt und somit ein grosses Bedürfnis der Anwender befriedigt.

Abstract

Thermal neutron radiography and tomography has proved itself as a method for non-destructive testing of materials in the last years. Even the purely qualitative inspection has provided valuable results, particularly because it is possible to penetrate materials (e.g. metals), that are opaque for X-rays. On the other hand, the sensitivity for certain light elements (e.g. hydrogen) is very high, while they are almost invisible for X-rays. Often the users are not only interested in qualitative but also in quantitative statements. For example in the soil physics, it is decisive to know the water content within the soil structure with a high spatial resolution for the investigation of the solute transport. Due to the digital detector systems used nowadays, such evaluations are basically possible, since the radiographs are presented as grayscale pictures, where the gray value is proportional to the incident neutron flux.

Nevertheless, exact statements about the material content of a sample are not easily done, since the exponential law of attenuation is valid only in first order. There are some effects disturbing this simple law or superposed to it.

The main reason for these deviations is that the neutrons are not only absorbed or undisturbed passed by the samples atoms, but they can be scattered. Many relevant materials (e.g. water) have even a much higher probability for scattering than for absorption. The scattered neutrons can hit the detector, where they provide a too high measured value. This pretended high transmission is misunderstood as a too small thickness or density of the measured sample.

A further reason for the deviation from the exponential law of attenuation is the polyenergetic spectrum of the neutron beam. Since most of the cross sections increase for lower energies in the thermal region, it is not possible to give a general value for them. Also the cross sections of the detector materials are dependent on the energy. These spectral effects affect the effective cross section, used for the evaluation of the quantitative mass thickness from the measured neutron flux.

In order to correct these disturbing effects, it is necessary to know the properties of the experimental arrangement. For the characterization of the neutron beam particularly the energy spectrum is important, but also the beam intensity and its spatial distribution play a role for the expected errors. Also the properties of the detector systems must be known. Depending on the experimental problem, the appropriate detector has to be chosen. The main criteria are the spatial or time resolution respectively, where a compromise must be found. Particularly the energy dependent absorption rate, but also the signal-to-noise ratio are important for the quantification of the radiographs.

The corruption of the pure transmission values by the scattering is corrected by calculating the scattering contribution and subtracting it from the radiograph. For this it is necessary to distinguish between background and sample scattering, according to the origin. The background scattering contains those neutrons, that pass the sample or transmit it undisturbed and are scattered to the detector by the surroundings of the sample (e.g. camera box) or the shielding. The sample scattering consists of the neutrons, that are scattered in the sample itself and hit the detector.

Large parts of the background scattering can be avoided by an appropriate experimental setup. In order to estimate the remaining part, the sample is replaced in an additional measurement by a body, that is opaque for neutrons. The measured neutron flux behind that black body is interpreted as background scattering. It is scaled to the intensity of the sample radiograph and subtracted from it.

For the correction of the sample scattering, Point Scattered Functions (PScF) are calculated by Monte-Carlo simulations. They describe the scattering distribution caused by a neutron beam from a point source penetrating a material layer. They depend on the neutron energy spectrum, the sample material, the thickness of the layer, the detector type and the sample-detector distance. The PScF are chosen according to the mass thicknesses obtained by the evaluation of the uncorrected radiograph, superposed to the total sample scattering behind all pixels of the radiograph, and subtracted from the original radiograph. The sample scattering is calculated several times in an iterative process from a more and more accurately corrected radiograph and subtracted from it.

The results of the simulations mentioned above can be used also for the correction of the spectral effects. They provide as a result also the expected transmission values for the layer thicknesses. The transmitted sample thickness is evaluated with these thickness-transmission pairs as reference values, after subtracting the

scattering contributions from the radiograph.

The correction algorithm has been tested by measurements of well known samples and yields results, that are accurate within about $\pm 5\,\%$. It has been used for relevant scientific and industrial experiments, and provided reliable quantitative material contents. The correction method has been tested successfully also at the facilities in Munich, Pretoria and Berlin. If the facility properties are known and the accurate cross section data are available for the calculation of the PScF and the transmission values, the radiographes recorded there are quantified as exactly as at NEUTRA, where the algorithm has been developed.

The effort needed for the application of the algorithm is reasonable, since the once calculated PScF are reusable for later measurements. The computing time of about 5 to 30 s for the correction of a radiograph is about the same as its recording time. With that, a tool is available, that allows the quantitative evaluation of neutron radiographs and tomograms for materials, and satisfies a large need of the users.

Contents

Chapter 1

Introduction

In many fields of research a non-destructive inspection of objects is required to answer crucial questions about structure and composition. In the field of soil sciences it may be desirable to determine the water distribution and flow process in soil columns at high resolutions, in archeology to obtain information about the material and manufacturing process of a sculpture or in electro-chemistry to detect the origin and transport of water in electric fuel cells. A neutron beam is able to penetrate such samples and is attenuated depending on the sample material, density and thickness. In neutron radiography, the information about these properties are projected by the parallel neutron beam onto a two dimensional transmission image, while the tomograms resolve them in three dimensions (figure 1.1).

These methods are well known from X-ray radiography and tomography. Since X-rays react with the electrons of the atoms, the investigated materials become opaque when containing elements with large atomic numbers. Unlike X-rays, neutrons react with the atomic nuclei and there is no simple rule for their cross sections (section 2.1.2). For thermalized neutrons e.g. the cross section of hydrogen is large compared to silicon, oxygen, calcium, potassium, sodium, iron and aluminum. These elements are the main components of soil minerals and therefore neutrons are ideal in order to determine the distribution of water in the pore space of the soil with a high spatial resolution and sensitivity. Carbon itself has a small neutron cross section, but because the organic material usually is associated with considerable amounts of hydrogen, it attenuates the neutrons efficiently. Since the exposure time for a radiograph is short compared to the water flow, also transient processes can be observed. This thesis has been carried out as a joint effort between the Neutron Imaging and Activation Group (NIAG) at the PSI and the group of soil
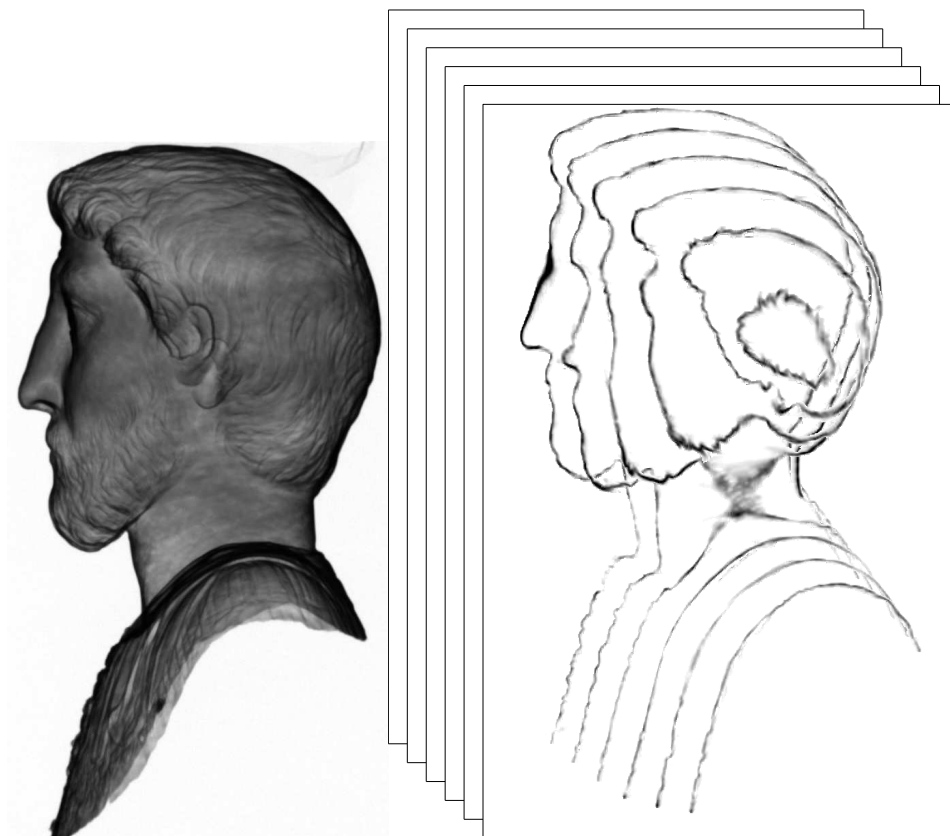
Figure 1.1: Transmission image (left) and tomographic slices (right) of the golden Marc Aurel sculpture of Avenches as a neutron radiography example. The transmission image shows the two dimensional projection through the sculpture. The tomogram resolves the third dimension and makes the 0.5 mm thin, strongly absorbing gold sheet visible (dark).

physics at the ETH Zurich, and therefore most of the applications mentioned here relate to soil physics. Other applications could have been chosen equally well to demonstrate the suitability of the correction methods proposed in this dissertation. Examples of other applications, where neutrons provide valuable information and where quantitative information is required, are building material physics, development of electric fuel cells, conservation technologies, archeology, nuclear technology and mechanically engineered parts, which are opaque in a X-ray beam.

Often it is already a valuable information to see the spatial distribution of a material inside a sample, e.g. preservative components in wood. But most scientists are further interested in quantitative statements, e.g. the exact amount of water in given structures. Although this information is contained in the recordings and numerically available due to the digital detector systems, it is corrupted by several effects, mainly by neutron scattering within the sample or by the materials of the experimental installation. The topic of this thesis is to identify and account for these effects and to implement a correction algorithm, which eliminates this confounding information.

This work is based on the earlier Ph.D. theses of H. Pleinert [1] and N. Kardjilov [2] about neutron radiography and tomography. Pleinert introduced the concept of the scattering correction by *Point Spread Functions (PSF)*. Kardjilov calculated the PSF by Monte-Carlo simulations and showed that after subtraction of the scattering component from the neutron radiograph of well defined samples, the remaining uncollided transmission signal corresponds better to the theoretically expected values. In this thesis the full experimental setup is included in the consideration. The *background scattering* is considered as a prime source of errors as well as the secondary effects by *detector properties* and *beam hardening*. The correction of these distortions on the projections reveals the correct attenuation coefficients in the reconstructed tomographic volume data. A software package is developed for an easy and effective correction of radiographs and tomograms. The algorithm is tested and successfully verified using exactly defined samples and the data obtained in the course of experiments conducted by guest scientists. The error of the quantification is reduced from up to 50 % or more prior to the correction to about 5 % after correction.

Chapter 2

The Neutron Tomography Method

Computed tomography is a method that provides three dimensional information of a sample by recording a set of two dimensional radiographs imaged at different angles and subsequent reconstruction of the volume data. Therefore it is important to understand the radiography method, which provides the raw data for tomography. Every physical effect disturbing the tomograms is already contained in the radiographs and can be corrected at this level, if its cause is understood (cf. chapter 5).

2.1 Neutron Radiography

A neutron radiography system consists basically of a nearly parallel neutron beam and a detector system (figure 2.1) [3]. The investigated sample is placed in the beam and the detector measures the transmitted neutrons. This section describes the components of a radiography system. The properties of specific facilities are presented in chapter 3.

2.1.1 Neutron Source

For neutron radiography usually thermal and cold neutrons are used, because most materials provide a higher attenuation for low energy neutrons. However, not only the attenuation but also the detection sensitivity of slow neutrons are higher. This
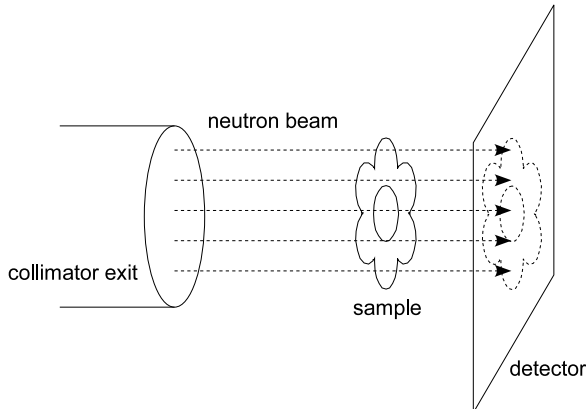
Figure 2.1: Schematic view of a neutron radiography system.

allows to use thin detectors, which results in a high resolution. Therefore only thermal and cold neutron sources are considered here.

After the extraction of the neutrons by a spallation or fission process, they have very high energies (~ 1 to $500\,\mathrm{MeV}$). Therefore, they must be slowed down by scattering processes in a moderator until reaching a thermal equilibrium with the moderator material. Usually, heavy water is used as moderator. The deuterium atoms have a large scattering cross section and a small absorption cross section. In addition they are light, so that the neutrons reach the thermal equilibrium already after a few scattering reactions, according to the conservation of energy and momentum. For a thermal spectrum the moderator is at room temperature, which yields neutron energies around $25\,\mathrm{meV}$ or velocities around $2200\,\mathrm{m/s}$. For a cold spectrum, usually liquid deuterium is used as a moderator and the temperature is about ten times lower (around $25\,\mathrm{K}$), yielding neutron energies around $2.2\,\mathrm{meV}$ ($650\,\mathrm{m/s}$).

When the neutrons are in a thermal equilibrium with the moderator, the collimator selects the neutrons flying in the same direction towards the sample and detector. The inevitable small divergence is described by the L/D-ratio, where L is the length of the collimator and D the diameter of the aperture (figure 2.2). Typical values for L/D are 100 to 800, which corresponds approximately to maximum divergence angles of 1.2 to 0.15 degrees.

The energy distribution of moderated neutrons corresponds in the thermal region ($E < E_{\mathrm{th}}$) roughly to a Maxwell spectrum (figure 2.3)

$$\Phi^0(E) \cdot \mathrm{d}E \propto \frac{E}{kT} \cdot \exp\left(-\frac{E}{kT}\right) \cdot \mathrm{d}E, \quad E < E_{\mathrm{th}}, \tag{2.1}$$
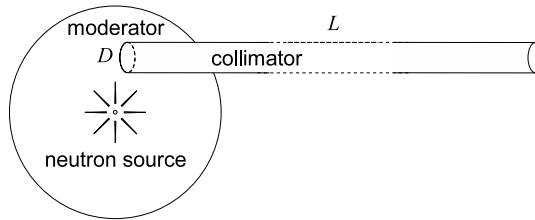
Figure 2.2: Schematic view of the neutron source, moderator and collimator. The ratio of the collimator length L and aperture D defines the divergence of the neutrons, and therefore the quality of the radiographs.

where Φ^0 is the neutron flux of the source, E the neutron energy, T the effective temperature and k the Boltzmann constant. Not only moderated neutrons contribute to the neutron beam, but also neutrons that are still in the moderation process. These neutrons form the epithermal region ($E_{\mathrm{th}} < E < E_{\mathrm{epi}}$) of the spectrum

$$\Phi^0(E) \cdot \mathrm{d}E \propto \frac{\mathrm{d}E}{E}, \quad E_{\mathrm{th}} < E < E_{\mathrm{epi}}. \tag{2.2}$$

After the moderation process, the directions of the neutron velocities are approximately isotropically distributed. By collimation only neutrons within a small solid angle in the direction of the sample are selected, so that the neutron beam reaching the sample can be considered as being parallel for the topic of this thesis.

If the z-axis is aligned with the neutron beam (assumed to be parallel), its flux $\Phi^0(E, x, y, t)$ is a neutron density in units $1/(\mathrm{eV} \cdot \mathrm{cm}^2 \cdot \mathrm{s})$. The total number of neutrons crossing an area in a time interval is then given by integration

$$\Phi^0_{\mathrm{tot}} = \iiiint \Phi^0(E, x, y, t) \, \mathrm{d}E \, \mathrm{d}x \, \mathrm{d}y \, \mathrm{d}t \quad . \tag{2.3}$$

The flux $\Phi^0(E, x, y, t)$ is composed of the *energy spectrum* $\Phi^0(E)$, *spatial distribution* $\Phi^0(x, y)$ and *temporal fluctuations* $\Phi^0(t)$

$$\Phi^0(E) = \iiint \Phi^0(E, x, y, t) \, \mathrm{d}x \, \mathrm{d}y \, \mathrm{d}t \tag{2.4}$$

$$\Phi^0(x, y) = \iint \Phi^0(E, x, y, t) \, \mathrm{d}E \, \mathrm{d}t \tag{2.5}$$

$$\Phi^0(t) = \iiint \Phi^0(E, x, y, t) \, \mathrm{d}E \, \mathrm{d}x \, \mathrm{d}y \quad . \tag{2.6}$$

These three functions are in first order independent from each other, i.e. the energy spectrum is the same at each source point (x, y) and time t and also the temporal fluctuations are the same for all source points and neutron energies. In
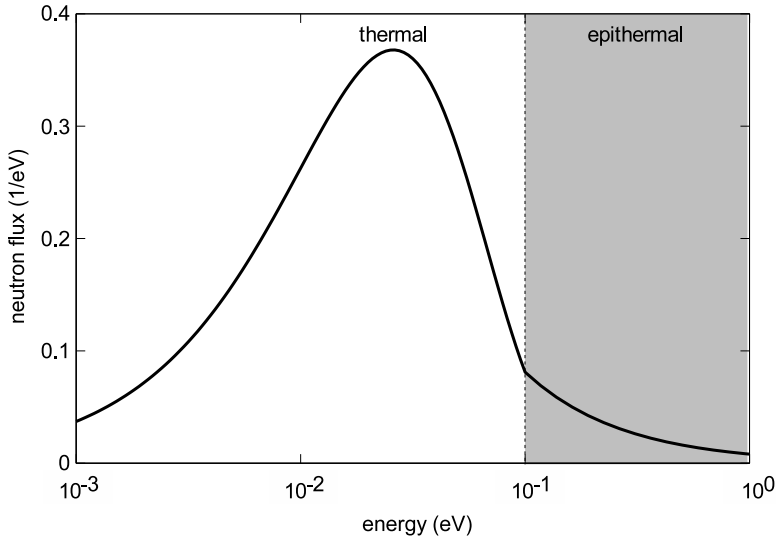
Figure 2.3: Maxwell spectrum of neutrons for the moderator temperature $300\,\mathrm{K}$ with an epithermal region above $100\,\mathrm{meV}$.

second order, mainly the energy spectrum $\Phi^0(E)$ depends also on the source points (x, y). Therefore the neutron flux can be decomposed into the product

$$\Phi^0(E, x, y, t) = \Phi^0_{\mathrm{tot}} \cdot \widetilde{\Phi}^0(E) \cdot \widetilde{\Phi}^0(x, y) \cdot \widetilde{\Phi}^0(t) \quad . \tag{2.7}$$

The tilde denotes the normalization to the total neutron count 1.

$$\widetilde{\Phi}^0(E) = \frac{\Phi^0(E)}{\Phi^0_{\mathrm{tot}}}, \quad \widetilde{\Phi}^0(x, y) = \frac{\Phi^0(x, y)}{\Phi^0_{\mathrm{tot}}}, \quad \widetilde{\Phi}^0(t) = \frac{\Phi^0(t)}{\Phi^0_{\mathrm{tot}}} \tag{2.8}$$

The temporal fluctuations depend on the type of the neutron source. While reactors provide a rather constant beam, spallation sources exhibit fluctuations or occasional interrupts.

2.1.2   Neutron Sample Interaction

Neutrons passing the sample can react with the atomic nuclei. Possible reactions are absorption or scattering events. The probability for a reaction (r) depends on the neutron energy and is described by the *microscopic cross section* $\sigma_{\mathrm{r}}(E)$ as the number of reactions A_{r} per atom in a thin layer of a material and per incident monoenergetic neutron flux Φ^0 with energy E (figure 2.4)

$$\sigma_{\mathrm{r}}(E) = \frac{A_{\mathrm{r}}}{N\Phi^0} \quad , \tag{2.9}$$
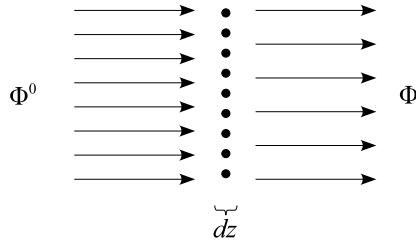
Figure 2.4: Definition of the microscopic cross section as the number of reactions per atom and incident flux in a thin layer.

where N is the number of atoms in the layer. The attenuation of the neutron flux $\mathrm{d}\Phi$ is given by the number of reactions per surface area S

$$\mathrm{d}\Phi = \frac{-\mathrm{d}A_{\mathrm{r}}}{S} = -\Phi^0 \sigma_{\mathrm{r}}(E)\frac{\mathrm{d}N}{S} = -\Phi^0 \sigma_{\mathrm{r}}(E)n\,\mathrm{d}z \quad , \tag{2.10}$$

with the atomic density n and the thickness $\mathrm{d}z$ of the thin layer of atoms. The neutron flux $\Phi(x)$ after the transmission of the thickness z is then given by the *exponential law of attenuation*

$$\Phi(z) = \Phi^0 \exp\left(-n\sigma_{\mathrm{r}}(E)z\right) = \Phi^0 \exp\left(-\Sigma_{\mathrm{r}}(E)z\right) \tag{2.11}$$

with the *macroscopic cross section* $\Sigma_{\mathrm{r}}(E)$ for the reaction r defined as

$$\Sigma_{\mathrm{r}}(E) = n \cdot \sigma_{\mathrm{r}}(E) \quad . \tag{2.12}$$

It is also called the *attenuation coefficient* or probability density for a reaction r, because with Eq. 2.10 it can be written as the reacting flux per incident flux and transmitted thickness

$$\Sigma_{\mathrm{r}}(E) = \frac{-\mathrm{d}\Phi}{\Phi^0\,\mathrm{d}z} \quad . \tag{2.13}$$

The definition of the cross section for a reaction r (Eq. 2.9) can be extended to the total cross section for all possible neutron reactions

$$\sigma_{\mathrm{tot}}(E) = \frac{1}{N\Phi^0}\sum_{\mathrm{r}} A_{\mathrm{r}} = \sum_{\mathrm{r}} \sigma_{\mathrm{r}}(E) \tag{2.14}$$

or the total attenuation coefficient, respectively

$$\Sigma_{\mathrm{tot}}(E) = \sum_{\mathrm{r}} \Sigma_{\mathrm{r}}(E) \quad . \tag{2.15}$$

For compound materials (e.g. molecular materials as H_2O or compositions of multiple isotopes), the microscopic cross section is defined as the mean value

$$\sigma_r(E) = \frac{\sum_i n_i \cdot \sigma_{i,r}(E)}{\sum_i n_i} = \frac{\sum_i n_i \cdot \sigma_{i,r}(E)}{n} \quad . \tag{2.16}$$

where n_i is the atomic density of the isotope i, $\sigma_{i,r}(E)$ its microscopic cross section for the reaction r and n the total number of atoms per volume. The macroscopic cross section of a compound material is then

$$\Sigma_r(E) = \sum_i n_i \cdot \sigma_{i,r}(E) = n \cdot \sigma_r(E) \quad . \tag{2.17}$$

The *mean free path length* $\lambda(E)$ of a neutron is calculated as the weighted average

$$\lambda(E) \quad = \quad \frac{-\int z \, d\Phi}{\Phi^0} = \frac{\int z \Sigma_{tot}(E) \Phi(z) \, dz}{\Phi^0} = \int z \Sigma_{tot}(E) \exp\left(-\Sigma_{tot}(E) z\right) \, dz =$$
$$\frac{1}{\Sigma_{tot}(E)} \int t \exp\left(-t\right) \, dt \quad , \tag{2.18}$$

with Eq. 2.13, 2.11 and the replacement $t = z \Sigma_{tot}(E)$. The remaining integral is known from the Euler Gamma function $\Gamma(x) = \int_0^\infty t^{x-1} \exp(-t) \, dt$ and $\Gamma(2) = 1$. Hence, the mean free path length is directly given by the inverse attenuation coefficient

$$\lambda(E) = \frac{1}{\Sigma_{tot}(E)} \quad . \tag{2.19}$$

The possible neutron reactions are divided into three physically different main types:

Absorption: The neutron is captured by the atomic nucleus, emitting a γ-quantum, an α-particle or a proton. The probability for these (n,γ), (n,α) or (n,p) reactions is described by the energy dependent absorption cross section $\sigma_a(E)$.

Coherent scattering: This reaction is particularly important for crystalline sample materials. The neutron is scattered elastically or inelastically at the crystal lattice of the sample with preferred angles, i.e. the cross section $\sigma_{coh}(E \to E', \theta, \varphi)$ depends not only on the initial and final energy E and E', but also strongly on the deflection angle θ and on the azimutal angle φ defined by the orientation of the reciprocal lattice of the crystal. The coherent scattering becomes particularly important for cold and thermal neutrons, where the de Broglie wavelengths are of the same order of magnitude as the

atomic distances (e.g. for $1\,\mathrm{meV}$ the neutron has the wavelength $9.0\,\text{Å}$, and for $10\,\mathrm{meV}$ it is $2.9\,\text{Å}$).

Incoherent scattering: The neutron is scattered at the atom by the scattering angle θ. The energy E' after the scattering reaction can vary from the initial energy E, i.e. the incoherent scattering cross section $\sigma_{\mathrm{inc}}(E \rightarrow E', \theta, \varphi)$ depends on the initial energy E and on the final energy E'. The dependence on the azimutal angle φ is in most cases negligible. Compared to the coherent scattering, the angular distribution of the scattered neutrons is almost isotropic.

For the purpose of neutron radiography, the different reactions are not distinguished. All neutrons reacting with the sample, either being absorbed or scattered, are considered as *collided* and hence out of the beam. It is (wrongly) assumed that the detector measures only the remaining directly transmitted, *uncollided* beam. In reality, also many scattered neutrons hit the detector. Under this assumption the angular dependence of the scattering cross sections is not relevant, so that the total cross section only depends on the neutron energy:

$$\begin{aligned}
\sigma_{\mathrm{tot}}(E) &= \sigma_{\mathrm{a}}(E) + \sigma_{\mathrm{coh}}(E) + \sigma_{\mathrm{inc}}(E) \\
&= \sigma_{\mathrm{a}}(E) + \iint \sigma_{\mathrm{coh}}(E \rightarrow E', \theta, \varphi)\,\mathrm{d}E'\,\mathrm{d}\Omega + \\
&\quad \iint \sigma_{\mathrm{inc}}(E \rightarrow E', \theta, \varphi)\,\mathrm{d}E'\,\mathrm{d}\Omega
\end{aligned} \tag{2.20}$$

In general, the sample is inhomogeneous, i.e. the atomic density n as well as the cross section σ and therefore also the attenuation coefficient Σ vary with the spatial coordinates (x, y, z)

$$\Sigma_{\mathrm{tot}}(E, x, y, z) = n(x, y, z) \cdot \sigma_{\mathrm{tot}}(E, x, y, z) \quad . \tag{2.21}$$

With the parallel neutron beam along the z-axis (as in section 2.1.1) the attenuated, uncollided beam behind the sample is then given by the flux

$$\Phi(E, x, y, t) = \Phi^0(E, x, y, t) \cdot \exp\left(-\int \Sigma_{\mathrm{tot}}(E, x, y, z)\,\mathrm{d}z\right) \quad . \tag{2.22}$$

2.1.3 Detector System

The detector system records the neutron flux $\Phi(E, x, y, t)$ behind the sample and makes it visible in an image that represents the measured intensity during the

recording time. For quantitative neutron radiography and tomography only digital systems are considered, that provide an image $I(x_i, y_j)$ as a discrete array of numbers, which are proportional to the physically registered neutron intensity.

All types of detectors for thermal and cold neutron radiography have a thin, neutron absorbing layer and count indirectly the produced secondary particle. This layer is homogenous and has an energy dependent macroscopic absorption cross section $\Sigma_{\mathrm{a}}^{\mathrm{det}}(E)$. The energy dependent absorption of the detection layer with the thickness s^{det} is then

$$A^{\mathrm{det}}(E) = 1 - \exp\left(-\Sigma_{\mathrm{a}}^{\mathrm{det}}(E) \cdot s^{\mathrm{det}}\right) \quad . \tag{2.23}$$

Using Eq. 2.22 the detected neutron flux behind the sample is

$$\begin{aligned}
\Phi^{\mathrm{det}}(x, y) &= \iint \Phi(E, x, y, t) \cdot A^{\mathrm{det}}(E)\, \mathrm{d}E\, \mathrm{d}t \\
&= \iint \Phi^0(E, x, y, t) \cdot \exp\left(-\int \Sigma_{\mathrm{tot}}(E, x, y, z)\, \mathrm{d}z\right) \cdot \\
&\quad \left(1 - \exp\left(-\Sigma_{\mathrm{a}}^{\mathrm{det}}(E) \cdot s^{\mathrm{det}}\right)\right) \mathrm{d}E\, \mathrm{d}t \quad .
\end{aligned} \tag{2.24}$$

In this thesis it is assumed that the subsequent counting of the secondary particle is independent of the incident neutron energy and also further loss of resolution due to the specific detector properties is negligible. Therefore, the value of a pixel with the finite area $\Delta x \cdot \Delta y$ in the image $I(x_i, y_j)$ is proportional to the total number of detected neutrons in the pixel area

$$I(x_i, y_j) \propto \int_{x_i - \Delta x/2}^{x_i + \Delta x/2} \int_{y_j - \Delta y/2}^{y_j + \Delta y/2} \Phi^{\mathrm{det}}(x, y)\, \mathrm{d}x\, \mathrm{d}y \quad . \tag{2.25}$$

2.2   Image Referencing

The transmission image is determined experimentally by recording the neutron beam behind the sample (Eq. 2.24) and the open beam flux without sample

$$\Phi^{\mathrm{ob}}(x, y) = \iint \Phi^0(E, x, y, t) \cdot \left(1 - \exp\left(-\Sigma_{\mathrm{a}}^{\mathrm{det}}(E) \cdot s^{\mathrm{det}}\right)\right) \mathrm{d}E\, \mathrm{d}t \quad . \tag{2.26}$$

The transmission through the sample is calculated by a subsequent division and scaling of the two measured fluxes

$$T(x, y) = f^{\mathrm{ob}} \cdot \frac{\Phi^{\mathrm{det}}(x, y)}{\Phi^{\mathrm{ob}}(x, y)} \quad . \tag{2.27}$$

The scaling factor f^{ob} is chosen so that the mean transmission $T(x, y)$ is 1 in a region without sample. It is necessary, because the two images cannot be recorded

at the same time and the neutron source intensity can fluctuate. This referencing is also known as *flat field correction*, because it eliminates the beam and detector inhomogenities from the radiograph.

The measured neutron fluxes Φ^{det} and Φ^{ob} (Eq. 2.24, 2.26) contain not only the sample properties $\Sigma(x, y, z)$ but also the beam and detector properties $\Phi^0(E, x, y, t)$, $\Sigma_{\text{a}}^{\text{det}}(E)$ and s^{det}, which are not objects of the investigation. All these properties can be combined in an effective attenuation coefficient Σ_{eff} that obeys for a homogeneous sample with thickness s the simple exponential law of attenuation for the measured transmission

$$T(x, y) = \exp\left(-\Sigma_{\text{eff}} \cdot s(x, y)\right) \tag{2.28}$$

$$\Sigma_{\text{eff}}(s) = \frac{-1}{s} \log T = \frac{-1}{s} \log\left(f^{\text{ob}} \cdot \frac{\Phi^{\text{det}}}{\Phi^{\text{ob}}}\right) \quad . \tag{2.29}$$

For a polyenergetic neutron beam, the effective attenuation coefficient depends on the sample thickness s. Therefore it is not possible, to obtain quantitative information about the sample thickness by the exponential law of attenuation. However, the expected transmission values for several given thicknesses can be precomputed numerically, yielding a reference curve that allows to transform measured transmission values to thickness values of a material, taking spectral effects as beam hardening and detector sensitivities into account (cf. chapter 4 and section 6.3).

Also the tomographic reconstruction is affected by the non-existence of a simple value for the effective cross section Σ_{eff}. The resulting attenuation coefficients are clearly underestimated at the center of the sample. Therefore the measured effective cross section $\Sigma_{\text{eff}}(s)$ is replaced by the constant value

$$\Sigma_{\text{eff}} = \lim_{s \to 0} \Sigma_{\text{eff}}(s) \tag{2.30}$$

in each pixel of the transmission images before the reconstruction.

2.3 Three Dimensional Reconstruction

In the radiographs the sample is projected to a two dimensional image. But the three dimensional distribution of the attenuation coefficients of the sample can be reconstructed by the methods of computed tomography from a set of transmission images $T_\theta(x, y)$ of the sample rotated by different angles θ. The coordinate system (x', y, z') is attached to the sample rotating around the y-axis by the angle θ, while the coordinate system (x, y, z) is defined by the neutron beam in z-direction (figure 2.5) and the rows and columns of the detector pixels (x_i, y_j). Therefore
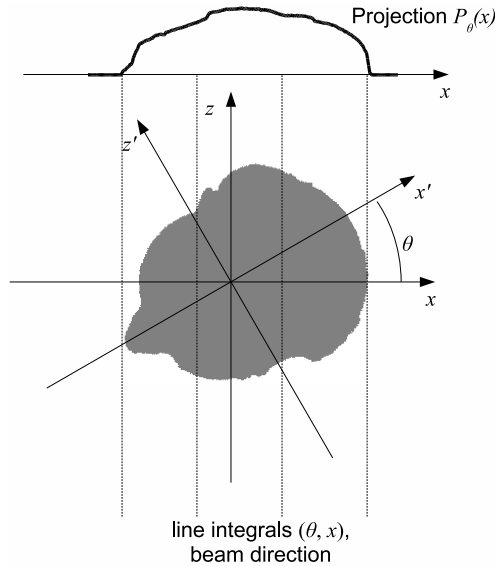
Figure 2.5: The sample is rotated by the angle θ and the line integrals at (θ, x) are measured as projections $P_\theta(x)$.

the attenuation coefficients are described as a function $\Sigma(x', y, z')$ in the rotating coordinate system. Since all the correction methods elaborated in this thesis are performed as preprocessing steps, i.e. before the three dimensional reconstruction, the reconstruction algorithm is not part of this thesis and outlined for the readers information only. For details see e.g. [4].

The reconstruction algorithm for the parallel beam geometry works in two dimensions (slices perpendicular to the rotation axis). It finds the two dimensional function $f(x', z')$ from the parallel projections (i.e. line integrals) along the z-axis of the sample rotated by the angle θ. The projections are given by

$$P_\theta(x) = \int f(x'_\theta, z'_\theta) \, \mathrm{d}z \tag{2.31}$$

with the rotated coordinates $x'_\theta = x'_\theta(x, z)$ and $z'_\theta = z'_\theta(x, z)$ attached to the sample.

The mathematical basis is given by the *Fourier Slice Theorem*, which states that the Fourier transform of the projection $P_\theta(x)$

$$\widehat{P}_\theta(w) = \int P_\theta(x) \cdot \exp\left(-2\pi i \cdot wx\right) \, \mathrm{d}x \tag{2.32}$$

gives the two dimensional Fourier transform of $f(x', z')$

$$\hat{f}(u, v) = \iint f(x', z') \cdot \exp\left(-2\pi i \left(ux' + vz'\right)\right) \, \mathrm{d}x' \, \mathrm{d}z' \tag{2.33}$$
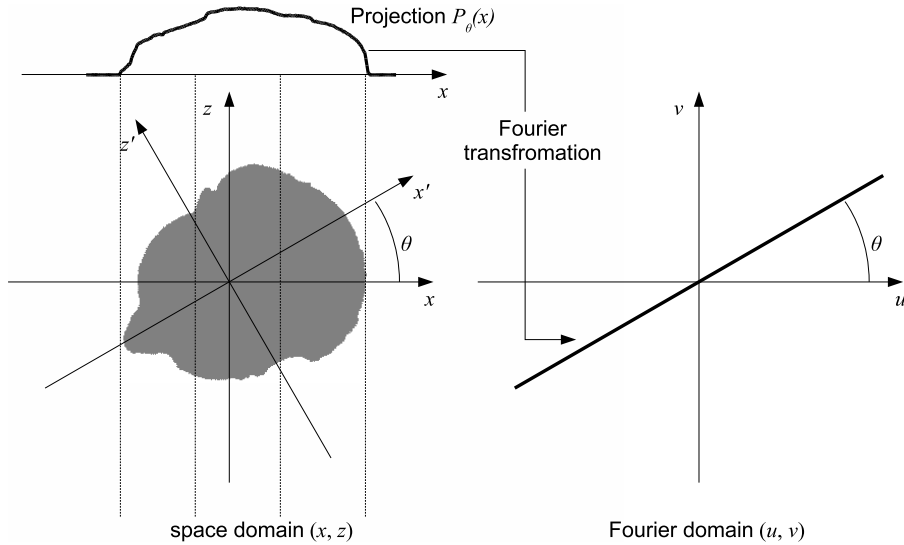
Figure 2.6: According to the Fourier slice theorem, the Fourier transformation of the projection $P_\theta(x)$ gives a line of the two dimensional Fourier transform of the function $f(x', y')$.

along a line in the Fourier domain (u, v), subtending the angle θ with the u-axis. Therefore $\hat{f}(u, v)$ and $\widehat{P}_\theta(w)$ are the same functions in the Fourier domain, either in rectangular coordinates (u, v) or in polar coordinates (θ, w). Hence the original function $f(x', z')$ is reconstructed by the inverse Fourier transformation (figure 2.6).

For numerical reasons, this algorithm is implemented by filtered backprojections instead of the mentioned Fourier transformations. The backprojections are obtained by reforming the fundamental mathematical expressions, details are also described in [4].

Applying the algorithm for every (x', z')-plane, yields the three dimensional function $f(x', y, z')$ or the physical attenuation coefficients $\Sigma(x', y, z')$, respectively from the transmission images $T_\theta(x, y)$.

Chapter 3

Experimental Facilities

The developed correction algorithm is designed to be transferable to every thermal or cold neutron radiography facility. They differ mainly by the neutron source and the available detector systems. Because their properties are important parameters for the correction algorithm, this chapter describes how they are characterized. The facilities, where the algorithm has been tested, are presented.

3.1   Neutron Sources

During this Ph.D. thesis the facility *Imaging with Cold Neutrons* (ICON) [5] has been designed and built at the Paul Scherrer Institut (PSI). It has been characterized together with E. Meier in a practical work in terms of the energy spectrum, intensity, spatial flux distribution and collimation. Since the collimation is simplified to be perfectly parallel for the correction algorithm, its measurement is not mentioned here.

The main experiments for this thesis have been performed at the thermal neutron radiography and tomography facility NEUTRA, PSI [6, 7]. The correction algorithm has been tested also for radiographs and tomograms recorded at the cold neutron radiography facilities ANTARES (FRM II, Technische Universität München) [8], CONRAD (Hahn-Meitner-Institut Berlin) [9] and the thermal facility SANRAD (Necsa Pretoria) [10]. The properties of these facilities are presented in the following sections.
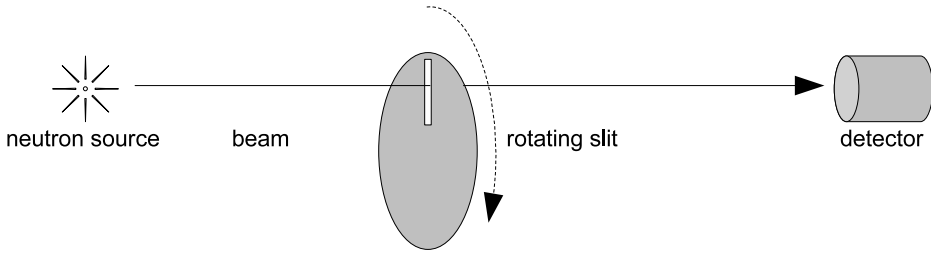
Figure 3.1: Experimental setup for time of flight measurements. The detector counts the neutrons in time intervals after passing the thin rotating slit.

3.1.1   Energy Spectrum

The neutron energy spectrum $\Phi(E)$ of thermal and cold neutrons can be measured by *time of flight* experiments (figure 3.1). The detector counts the number of neutrons C_i in N time intervals $[t_{i-1}, t_i]$, $(i = 1 \ldots N)$ after passing the thin rotating slit

$$C_i = \int_{E_{i-1}}^{E_i} \Phi(E) \, \mathrm{d}E \quad , \tag{3.1}$$

where E_i and E_{i-1} are the energy limits for a neutron to reach the detector in the time interval $[t_{i-1}, t_i]$. The experimental results form a step function

$$\Phi^{\mathrm{exp}}(E) = \frac{1}{E_i - E_{i-1}} \int_{E_{i-1}}^{E_i} \Phi(E') \, \mathrm{d}E' \quad \text{with} \quad E_{i-1} < E < E_i \quad . \tag{3.2}$$

The experimental result of the time of flight measurement at the ICON facility is plotted in figure 3.2. The comparison with the fitted Maxwell spectrum makes clear that the theoretical approximation is unusable. Because the neutrons are not completely moderated by the cold source, it matches only up 15 meV. In the range of 15 to 100 meV there is a remaining bulge with thermal neutrons and beyond 100 meV are the epithermal neutrons.

In the low energy region (~ 1 meV) the statistical error of the measurement becomes dominant because the number of neutrons is very small (note the double logarithmic scale). At about 100 meV there is a break, where the epithermal region starts. Although the epithermal flux is small compared to the thermal flux, it is spread over a large energy range. According to the measurement shown in figure 3.2, covering a range up to 5.14 eV, 25 % of the neutrons are epithermal. Because of their small flux values, the experimental error in this region is mainly determined by the neutron background signal and the detector efficiency, that must be taken into account in the evaluation of the experiment. Even small changes have
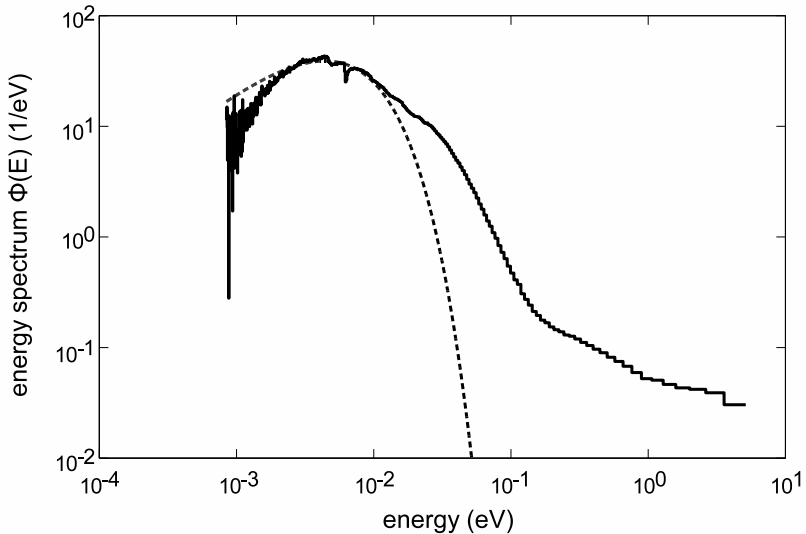
Figure 3.2: The measured ICON spectrum (solid) compared to the Maxwell spectrum for the temperature 51 K (dashed). The temperature of the liquid deuterium moderator is 25 K.

a large effect. This uncertainty and the lack of experimental data above 5.14 eV is a major source of error for the correction algorithm, because the cross section of some sample materials (e.g. water or aluminum) decrease by less than a factor of 10 over the whole energy range (figure 3.3). The detector material gadolinium has a lot of strong resonances in the epithermal region, hence it is not possible to calculate the correct effective attenuation coefficient Σ_{eff} (Eq. 2.29). Fortunately, the most often used detector material [6]lithium has a smooth and continuously decreasing cross section, so that epithermal neutrons are hardly detected.

The measured spectra of the NEUTRA, ICON and ANTARES facilities are shown in figure 3.4 together with the simulated CONRAD spectrum. Since all spectra are normalized to the total integrated flux 1, the integrals of the graphs are comparable. Although such a comparison is difficult to see because of the double logarithmic scales, it is evident that the ICON spectrum has the largest amount of epithermal neutrons, even more than the thermal NEUTRA spectrum. The ANTARES and ICON spectrum are rather similar, but at ANTARES there are less epithermal neutrons, but more thermal and cold neutrons and the maximum of the spectrum is shifted to colder energies. This indicates that the ANTARES spectrum is more effectively moderated.
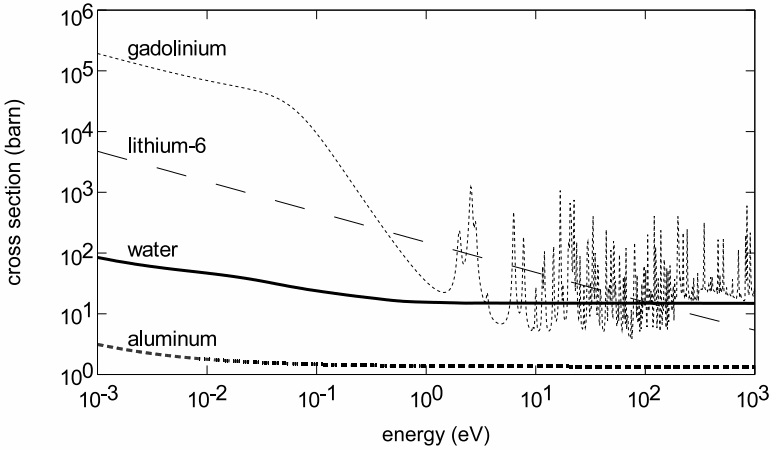
Figure 3.3: Cross sections of the typical sample materials water and aluminum and the detector materials gadolinium and [6]lithium in the cold, thermal and epithermal energy range.

At low energies the simulated CONRAD spectrum is similar to that of ICON, but it shows no epithermal neutrons. They are filtered due to the neutron guide instead of the collimator. Unfortunately, there are neither time of flight measurements nor simulations of the SANRAD spectrum available. Since it is thermal, the NEUTRA spectrum has been used to evaluate the radiographs recorded at Necsa. Therefore, calculations with the spectra of CONRAD and SANRAD must be considered with caution because of the large uncertainties.

3.1.2   Neutron Flux Intensity

The mean neutron flux intensity is an important value for neutron imaging, because it affects the minimum required exposure time or the actual signal-to-noise (S/N) ratio, respectively. For quantifying the radiographs the flux intensity is important, because the detection limits and statistical error are determined by the S/N-ratio.

The mean neutron flux $\overline{\Phi}$ is defined as the spatial and temporal mean of the flux $\Phi(E, x, y, t)$ (cf. Eq. 2.3–2.6)

$$\overline{\Phi} = \frac{1}{S \cdot t} \iiiint \Phi(E, x, y, t')\, \mathrm{d}E\, \mathrm{d}x\, \mathrm{d}y\, \mathrm{d}t' \quad , \tag{3.3}$$

i.e. the number of neutrons per unit surface $S = \iint \mathrm{d}x\,\mathrm{d}y$ and time $t = \int \mathrm{d}t'$. It is measured with gold foils that are exposed to the neutron beam at the beam exit of the shielding. The gold foil is activated and from the measurement of the
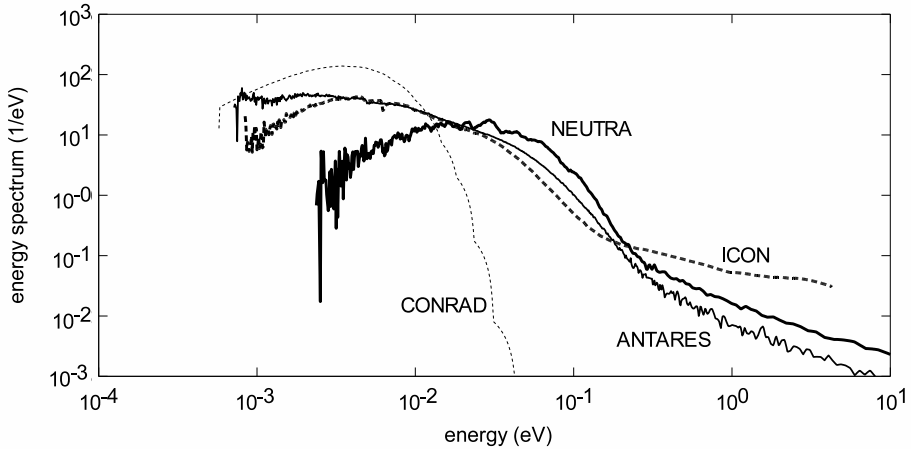
Figure 3.4: Neutron energy spectra of the NEUTRA, ICON, ANTARES (measured) and CONRAD (simulated) facilities with the total integrated flux normed to 1.

activity, the neutron flux can be calculated. The activity $A(t)$ of the gold foil during irradiation as a function of time is

$$A(t) = \overline{\Phi}S \cdot \left(1 - e^{-N\sigma_{\text{eff}}d/V}\right)\left(1 - e^{-\lambda t}\right) \quad , \tag{3.4}$$

where σ_{eff} is the effective microscopic cross section of gold, N the number of gold atoms in the foil, V, S and d the volume, surface and thickness of the foil and λ the decay constant of gold.

The saturation activity A_{sat} is reached when the same amount of gold atoms become activated by the neutron beam as decay. It is given by

$$\begin{aligned} A_{\text{sat}} &= \lim_{t \to \infty} A(t) = \overline{\Phi}S \cdot \left(1 - e^{-N\sigma_{\text{eff}}d/V}\right) \\ &\approx \overline{\Phi}S \cdot \frac{N\sigma_{\text{eff}}d}{V} = \overline{\Phi}N\sigma_{\text{eff}} \quad . \end{aligned} \tag{3.5}$$

The approximation is valid for foils, which are thin compared to the mean free path length of the neutrons, that is in the order of $1\,\text{mm}$. The foils used in the experiments are around $0.05\,\text{mm}$ thick. With this simplification and for short exposure times compared to the decay time $1/\lambda = 93\,\text{h}$, the activity $A(t)$ (Eq. 3.4) is

$$A(t) = A_{\text{sat}} \cdot \left(1 - e^{-\lambda t}\right) \approx A_{\text{sat}}\lambda t \quad . \tag{3.6}$$

Using Eq. 3.5 and 3.6 the neutron flux is then calculated as

$$\overline{\Phi} \approx \frac{A_{\text{sat}}}{N\sigma_{\text{eff}}} \approx \frac{A(t)}{N\sigma_{\text{eff}}\lambda t} \quad . \tag{3.7}$$
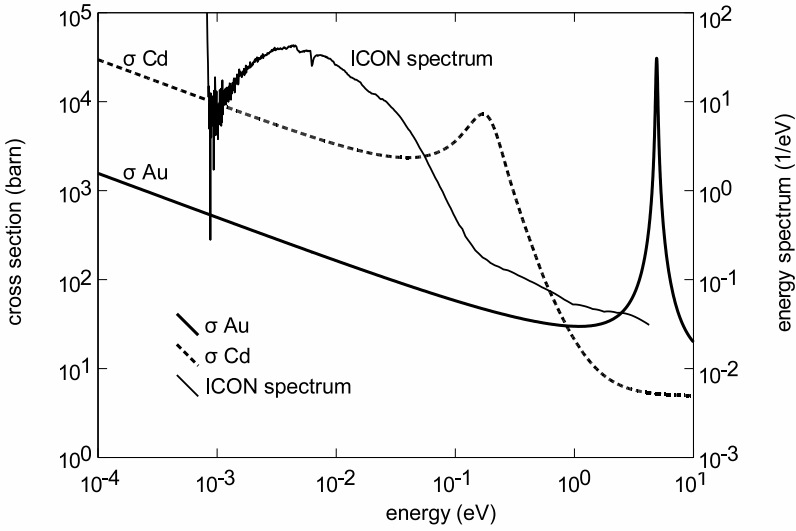
Figure 3.5: Cross sections of gold and cadmium in the measured energy range of the ICON spectrum.

The activity $A(t)$ and exposure time t are measured in the experiment and the number of atoms N ($3.056 \cdot 10^{24}$ atoms/kg) and the decay constant $\lambda = 2.978 \cdot 10^{-6}$ 1/s are known as well as the energy dependent cross section $\sigma(E)$. The effective cross section of gold is calculated as (cf. Eq. 2.29 and 2.12)

$$\sigma_{\text{eff}} = \frac{-V}{Nd} \log \left(\frac{\int \Phi(E) \exp\left(-N\sigma(E)d/V\right) \, \mathrm{d}E}{\int \Phi(E) \, \mathrm{d}E} \right) \quad , \tag{3.8}$$

where the spectrum $\Phi(E)$ is known from the time of flight measurements (section 3.1.1). The numerical integration is difficult because the cross section of gold has a resonance at 5 eV, where the measured spectrum ends and is not precisely known (figure 3.5).

Therefore, the gold foils have been exposed to the neutron beam once behind a 1 mm thick cadmium shielding and once without the shielding. Since the cross section of cadmium decreases sharply at 955 meV, one can assume that it blocks all neutrons below this energy and is completely transparent at higher energies. This threshold value is found by Monte-Carlo simulations of the two experiments. It is chosen such that the difference of the gold foil activation without and with the cadmium shielding equals the activation due to the neutrons with energies lower than the threshold value.

The thermal flux in the range 0 to 955 meV is then determined using the accu-

rately computable cross section for thermal neutrons

$$\sigma_{\text{eff}}^{\text{th}} = \frac{-V}{Nd} \log \left(\frac{\int_0^{955\,\text{meV}} \Phi(E) \exp\left(-N\sigma(E)d/V\right) \, \text{d}E}{\int_0^{955\,\text{meV}} \Phi(E) \, \text{d}E} \right) = 141 \, \text{barn} \qquad (3.9)$$

and the difference of the activities without $(A_0(t_1))$ and with the cadmium shielding $(A_{\text{Cd}}(t_2))$ as defined in Eq. 3.7

$$\overline{\Phi}_{\text{th}} \approx \frac{1}{N\sigma_{\text{eff}}^{\text{th}}\lambda} \left(\frac{A_0(t_1)}{t_1} - \frac{A_{\text{Cd}}(t_2)}{t_2} \right) = 4.3 \cdot 10^8 \, \frac{1}{\text{cm}^2 \cdot \text{s}} \qquad . \qquad (3.10)$$

The value of this thermal flux is reliable, while the value for the epithermal flux is rather an estimation

$$\overline{\Phi}_{\text{epi}} \approx \frac{A_{\text{Cd}}(t)}{N\sigma_{\text{eff}}^{\text{epi}}\lambda t} = 1.9 \cdot 10^7 \, \frac{1}{\text{cm}^2 \cdot \text{s}} \qquad , \qquad (3.11)$$

because it is not possible to compute the epithermal effective cross section accurately.

$$\sigma_{\text{eff}}^{\text{epi}} = \frac{-V}{Nd} \log \left(\frac{\int_{955\,\text{meV}}^{5.14\,\text{eV}} \Phi(E) \exp\left(-N\sigma(E)d/V\right) \, \text{d}E}{\int_{955\,\text{meV}}^{5.14\,\text{eV}} \Phi(E) \, \text{d}E} \right) \approx 248 \, \text{barn} \qquad (3.12)$$

The total measured mean flux is then the sum of the thermal and epithermal flux (Eq. 3.10, 3.11)

$$\overline{\Phi} = \overline{\Phi}_{\text{th}} + \overline{\Phi}_{\text{epi}} = 4.5 \cdot 10^8 \, \frac{1}{\text{cm}^2 \cdot \text{s}} \qquad . \qquad (3.13)$$

This is the maximum flux at the ICON facility with the aperture completely opened and at the exit of the target block. Neutron imaging is done with a smaller aperture and at larger distances to the neutron source in order to have a higher L/D-ratio. At the positions designed for radiography the flux is 1.5 to $2.8 \cdot 10^6 \, 1/(\text{cm}^2\text{s})$. Table 3.1 shows the typical fluxes of the facilities where the correction algorithm has been tested. The fluxes depend on the collimation ratio and field of view. Generally, the fluxes from reactor sources are higher than from the spallation sources NEUTRA and ICON. The very high maximum flux of CON-RAD is obtained due to neutron guides instead of a collimator, at the cost of a low L/D-ratio.

3.1.3 Spatial Flux Distribution

The spatial flux distribution has been experimentally determined at the ICON facility by imaging plate recordings for the three measurement positions and different

Table 3.1: Neutron flux, field of view and collimation ratio of the facilities where the correction algorithm has been tested.

facility	neutron flux $[1/(cm^2 s)]$	field of view [cm]	L/D [1]
NEUTRA	$2.9 \cdot 10^7$	$\varnothing 15$	200
	$7.9 \cdot 10^6$	$\varnothing 29$	350
	$4.2 \cdot 10^6$	$\varnothing 40$	550
ICON	$1.5 \cdot 10^6$	8×13	710
	$2.8 \cdot 10^6$	15×23	605
ANTARES	$9.4 \cdot 10^7$	32×32	402
	$2.5 \cdot 10^7$	36×36	795
CONRAD	$3.0 \cdot 10^9$	3×5	70
	$1.0 \cdot 10^7$	15×15	500
SANRAD	$1.6 \cdot 10^6$	$\varnothing 36$	150
	$3.0 \cdot 10^6$	$\varnothing 36$	300
	$9.8 \cdot 10^5$	$\varnothing 36$	500

collimator apertures. Some results for the end position (greatest collimation length and field of view) are shown in figure 3.6.

The smallest aperture (0.05 cm) works like a pinhole camera and therefore the sharp boundaries of the cold neutron source (left) and collimator are projected onto the detector plane. The advantages of this aperture are the high collimation ratio (L/D) and the broad plateau of a relatively high flux. The absolute flux is of course very small because of the small aperture. The bright peaks in the horizontal profile originate from neutrons reflected at the collimator walls and form a sharply defined region in the field of view. Since the reflection is possible only for cold neutrons, the energy spectrum in this region will be different from the mean spectrum measured by the time of flight experiment. Because the spectrum is an important, spatially constant input parameter for the correction algorithm, this aperture would be a bad choice for quantitative neutron radiography.

With the largest aperture (8 cm), the boundaries are smeared out and the neutron spectrum is everywhere the same. But since they are smeared, the high flux plateau has vanished. Radiography with this setting would have a good S/N-ratio in the center of the beam, but it would be poor in the surrounding area. This deteriorates the quantification limits.

A good compromise of high flux, broad plateau, homogeneous neutron distri-

bution and a favourable collimation ratio is found with the aperture $2\,cm$. This is chosen as the standard setting for transmission radiography at the ICON facility. In table 3.1 the spatial flux distributions are compared for the facilities where the correction algorithm has been tested.

3.2 Detectors

For every experiment, a suitable detector system must be chosen. While an imaging plate reveals details of a sample with a high resolution, a scintillator screen in combination with a CCD camera is the most efficient constellation for tomography. These are the two major digital detector systems used in neutron radiography and tomography. In the following sections they are being described and compared.

3.2.1 Imaging Plate

The neutron imaging plates have a thin film of gadolinium (Gd) as absorption material. Natural gadolinium consists of $14.8\,\%$ ^{155}Gd and $15.7\,\%$ ^{157}Gd, which have huge absorption cross sections for thermal neutrons ($61,100\,barn$ and $259,000\,barn$ for the neutron energy $25.3\,meV$). Both isotopes capture the neutron by a (n,γ) reaction. The γ-irradiation excites the electrons, which will be trapped in the conduction band, so that the information of the neutron absorption is stored in the imaging plate. After the exposure it is read out by a scanner, that excites the trapped electrons by a laser and lets them recombine with the crystal ions. The photo-stimulable luminescence (PSL) is emitted by the recombination and recorded by the scanner. Finally, the intensity of the PSL is proportional to the number of absorbed neutrons and digitally available as a 16-bit integer [11, 12].

The imaging plate is removed and scanned after each exposure and repositioned for the next exposure. Since the repositioning is not very accurate, it is unsuitable for image referencing (cf. section 2.2). Therefore, it is not the primary choice for quantitative neutron radiography. However, it produces very sharp images with a pixel size down to $12.5\,\mu m$.

3.2.2 Scintillator

Scintillators for neutron imaging perform a twofold conversion: first, the neutrons are absorbed in a (n,α) or (n,γ) reaction. Then, in a second reaction the α or γ produces the visible light, which is recorded by a CCD camera or an amorphous

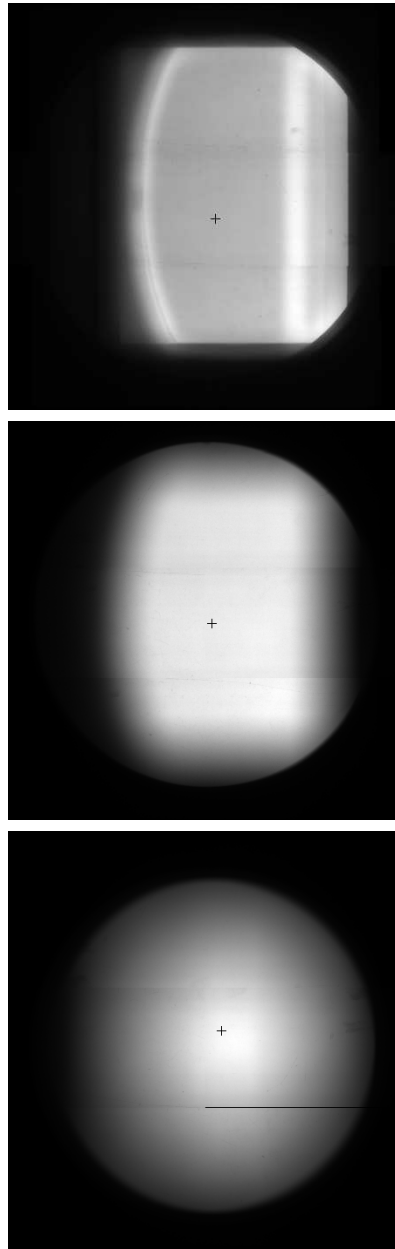Figure 3.6: Left: Spatial flux distributions at the end position of the ICON facility for collimating apertures 0.05 cm (top), 2 cm (middle) and 8 cm (bottom). Center, right: Horizontal and vertical profiles through the center of the beam (cross). The flux values are scaled such that the center value equals 1. The two dips in each vertical profile are artefacts due to the imaging plate reader.
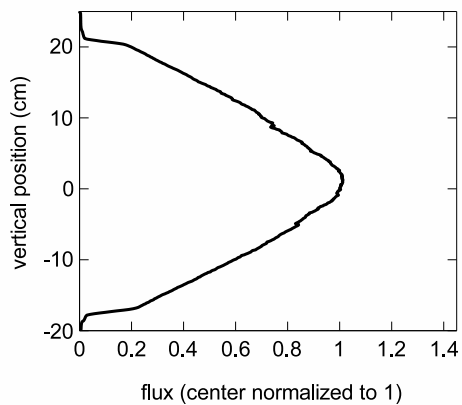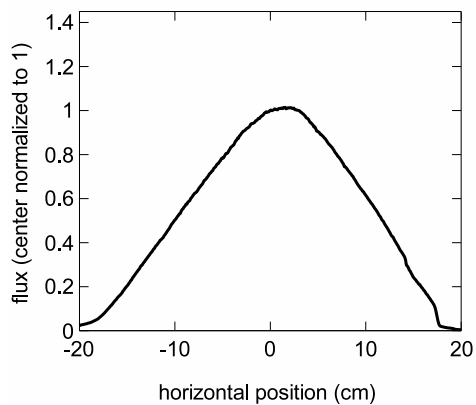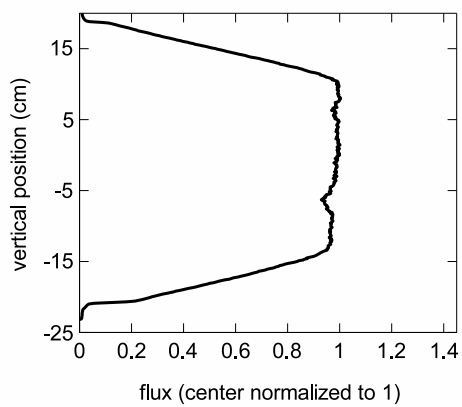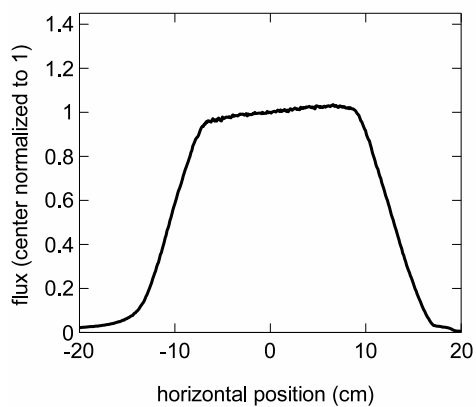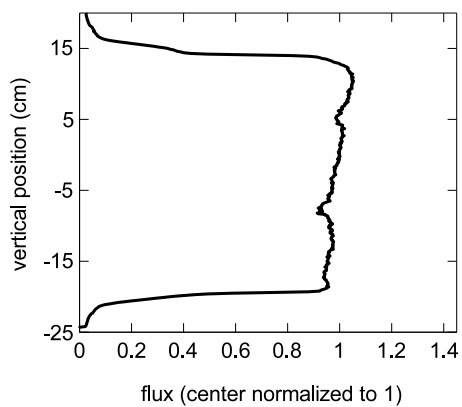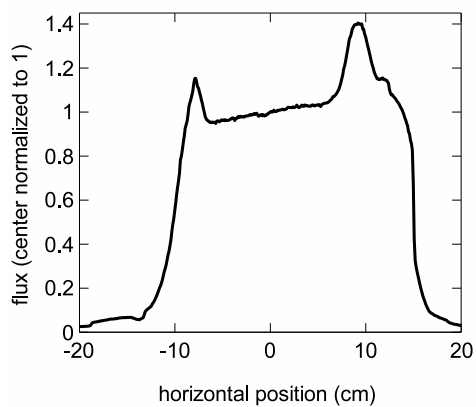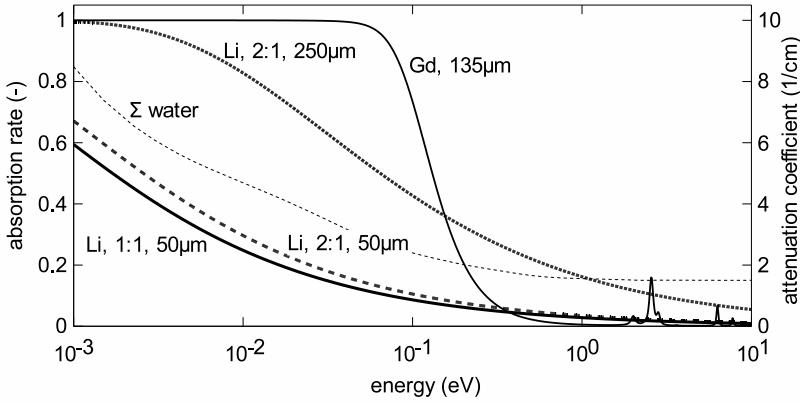
Figure 3.7: Absorption rates (Eq. 2.23) of the Li and Gd scintillators (various mixture and thickness combinations). Since they affect the effective attenuation coefficient of a sample material, the energy dependent macroscopic cross section of water is overlayed as an example (right scale).

silicon flat panel [13]. Since the light is not produced directly by the neutron, but by secondary particles, which are spread around the location of the neutron reaction, the size of the light spot produced by a neutron reaction and therefore the blurring increases with the scintillator thickness. On the other hand, a thin scintillator causes a poor signal-to-noise ratio because of the small neutron reaction rate. Therefore, it is ideal to have several scintillator types to be used depending on the experimental conditions and needs.

As a neutron absorbing material either ^{6}Li or ^{nat}Gd is used. Figure 3.7 shows the neutron absorption rates (Eq. 2.23) for four different scintillator materials: ^{6}LiF/ZnS (mixture 1:1 by weight, thickness 50 µm), ^{6}LiF/ZnS (2:1, 50 µm), ^{6}LiF/ZnS (2:1, 250 µm) and ^{nat}Gd$_2$SO$_2$ (thickness 135 µm). They differ significantly, which affects not only the signal-to-noise ratio, but also the effective neutron cross section of a sample (Eq. 2.30). Table 3.2 shows that it varies for Li-scintillators and the NEUTRA spectrum within 3 % and for the colder ICON spectrum even within 10 % (cf. section 5.3). Hence, it is important to know the detector properties and to take them into account for quantitative neutron radiography or tomography.

In order to compare the Li- and Gd-scintillators, two stones have been recorded with the two scintillators. The horizontal profiles are shown in figure 3.8. It is clearly visible that the Gd-scintillator measures less attenuation of the stones than the Li-scintillator, which is in agreement with table 3.2. Moreover, it becomes also

Table 3.2: Effective attenuation coefficients of water for the scintillators shown in figure 3.7 and the NEUTRA and ICON spectrum.

detector (mixture, thickness)	$\Sigma_{\mathrm{eff}}^{\mathrm{H_2O}}$ (NEUTRA) [1/cm]	$\Sigma_{\mathrm{eff}}^{\mathrm{H_2O}}$ (ICON) [1/cm]
^{6}LiF/ZnS (1:1, 50 µm)	3.52	4.65
^{6}LiF/ZnS (2:1, 50 µm)	3.51	4.62
^{6}LiF/ZnS (2:1, 250 µm)	3.40	4.20
Gd_2SO_2 (135 µm)	3.29	4.11

visible that the edges measured by the Gd-scintillator are smoother (cf. center of the profiles at 15 cm). The reason for this is that the γ produced by the neutron absorption produce the visible light in a wide region. The image sharpness and quantification accuracy suffer from this. Therefore only Li-scintillators have been used for the quantification described in this thesis. Potentially, the problems with the Gd-scintillator could be avoided by a deconvolution with the point spread function of that detector system.

The signal-to-noise (S/N) ratio of a Li-scintillator photographed by a cooled CCD-camera is shown in figure 3.9. It is evident that it is proportional to the square root of the exposure time, i.e. the number of recorded neutrons. This means that the S/N ratio depends only on the collected neutron statistics and only secondarily on other effects such as the camera readout. For the typical recording times 10 to 20 s of a radiograph with that scintillator at the ICON facility, a S/N ratio of about 200 to 300 can be expected in an open beam region.
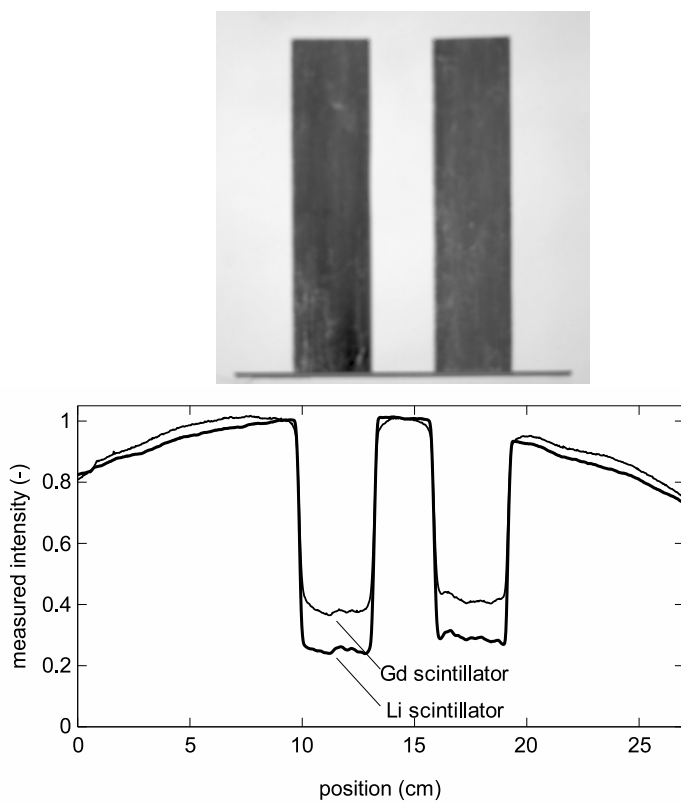
Figure 3.8: Horizontal profiles (left) of the radiographs of two stones (right) recorded by a Li- and Gd-scintillator (the measured intensity values are scaled to fit each other).
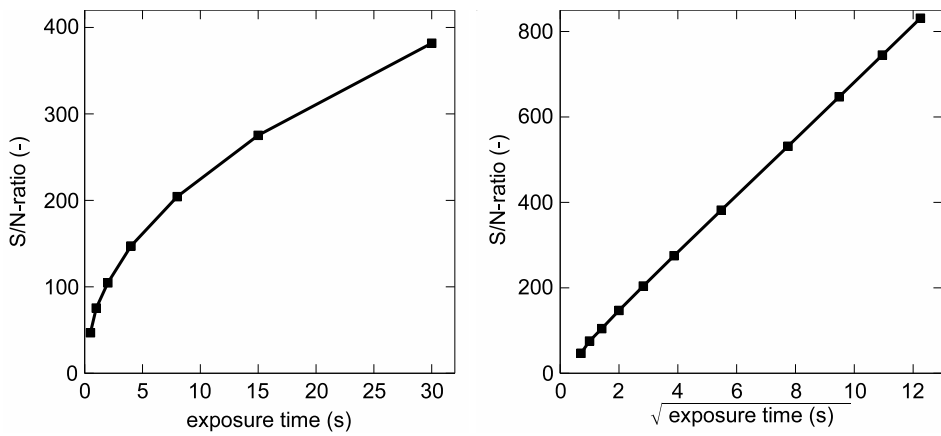
Figure 3.9: Measured S/N ratios of a ^{6}LiF/ZnS scintillator (mixture 2:1, thickness $300 \, \mu$m) for several exposure times determined at the ICON faciltiy. Left: evaluation of single recordings in a linear scale; right: the last four measurements are obtained by an accumulation of 2 to 5 recordings (each 30 s) plotted against the square root of the exposure time.

Chapter 4

Monte-Carlo Simulations

In order to understand the physical effects in neutron radiography and to determine their consequences quantitatively, Monte-Carlo simulations of the experiments are an effective tool. The particle transport is simulated with pseudo-random decisions about the origin of the neutron (e.g. place, energy, direction) and its interactions with the matter. The decisions are always made within the constraints of the simulated experimental setup and according to the physical probabilities, i.e. cross sections. After the transport of many particles, the simulation yields the expected neutron distribution as a result.

It allows to separate the various effects of a radiograph. For example to study the effect of beam hardening in neutron radiography, the detector sensitivity is set constant for all energies, the scattered neutrons are discarded and the beam divergence is set to zero. In a similar way it is possible to investigate the influence of the neutron spectrum (epithermal neutrons), neutron scattering, beam divergence, energy dependence of the detector sensitivity, shielding of the experimental facility, etc. by assuming ideal conditions for the rest of the experimental setup.

In contrast to solving the differential equations for the neutron transport numerically, Monte-Carlo simulations are the suitable tool for calculating the neutron radiographs. It is possible to model the relatively complex experimental setup and it is easily changed for variations of the experiment. Because in the simulation the neutrons can be started at the collimator exit, they are directed to the sample and detector, which increases the efficiency of the calculation.

The computing time for a Monte-Carlo simulation depends on many factors, but it is basically given by the intended accuracy of the results. Since it is a statistical method, the accuracy is proportional to the square root of the number

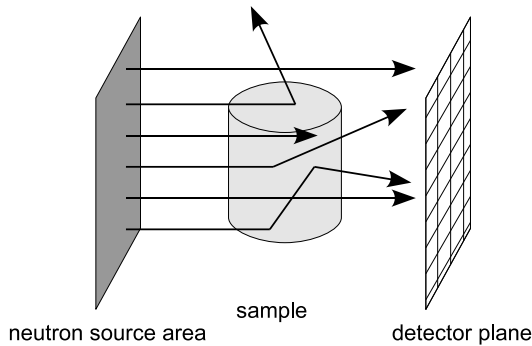neutron source area   sample   detector plane

Figure 4.1: The three main components for the Monte-Carlo simulation of a neutron radiograph: the source area of the neutrons, the sample description and the setup of the pixel detector. The neutrons are transported through the sample and absorbed, scattered or transmitted through the sample, according to the cross sections. Also multiple events can occur in a history.

of the started neutrons and hence with the square root of the computing time. Fortunately, the history of a neutron in the simulation of a radiograph is simple: it is started with a certain energy and direction, transmitted, scattered or absorbed in the sample and finally counted by the detector (figure 4.1). Therefore, it is feasible to simulate hundreds of millions of neutrons. On the other hand, the highly resolving detector needs a lot of neutrons, so that the neutron statistics in each pixel is reasonable. These calculations have been done on up to 16 processors in a linux cluster. Since all neutron histories are independent from each other, the computing time is reduced almost linearly with the number of processors.

During this thesis, the Monte-Carlo software MCNPX [14] has been used. It has the advantages that the libraries for the cross sections are available for almost all isotopes, it is very flexible in constructing geometries and it provides a variety of analysis possibilities, including statistical evaluations.

4.1   Neutron Source

The collimator exit of a real experiment is considered as the neutron source for the simulations. For the investigation of the neutron scattering, beam hardening and detector sensitivity, it is not necessary to simulate the beam divergence. Therefore all neutrons are started exactly parallel to the z-axis. But in order to investigate the resolution possibilities of neutron imaging, the beam divergence would be a

decisive parameter.

Another very important parameter is the neutron spectrum because the cross sections of the sample materials as well as the detector material can vary considerably with the neutron energy. If the spectrum is measured by a time of flight experiment (cf. section 3.1.1), the resulting flux $\Phi^{\mathrm{exp}}(E)$ (Eq. 3.2) is directly used as an input parameter. If the spectrum is unknown, it can be estimated as a Maxwell spectrum (Eq. 2.1) at a given temperature. The uncertainty or even the complete absence of the epithermal spectrum (Eq. 2.2) can lead to an error because the absolute number of epithermal neutrons can be large. Although the flux (in units 1/eV) is small, the energy range covers several orders of magnitude. The error caused by the uncertainty at the low energy limit of the time of flight measurement is small because only a few neutrons are affected.

An example of the MCNPX code for a neutron source modelling is given in appendix A.1.

4.2 Detector

Since it is known from real experiments that the measured effective attenuation coefficient Σ_{eff} (Eq. 2.29, 2.30) depends on the detector system, the modelling of the detector in the simulations is a major issue. It is also known from experiments that the measured neutron intensity linearly depends on the exposure time and hence also linearly on the real intensity. Therefore it is sufficient to consider the neutron absorption rate, while the following physical processes such as light conversion, light output, optics and CCD camera can be omitted in the simulation.

Although MCNPX offers a specific radiography tally (i.e. neutron counter), this is not used for the simulations, because it has not the flexibility and combination possibilities as the other tallies. Instead of that, usually a surface tally (F1) has been used, which is easily divided by macrobodies into a rectangular grid that corresponds to the detector pixels. The code for a two dimensional pixel detector is given in the appendix A.2. It can even be extended to a three dimensional detector, so that several sample-detector distances are simulated in a single run. Often it is not necessary to simulate a detector with a large number of pixels, which slows down the execution of the simulation. Rather, it is preferable to decrease either the resolution or to concentrate on a detail at a high resolution. If the problem is symmetric, the detector can be adjusted accordingly, e.g. to a one dimensional or circular detector can be chosen. This dramatically reduces the number of neutron

histories needed for good statistics.

In MCNPX it is possible to add an energy dependent multiplier to a tally. Setting this multiplier to the neutron absorption rate $A^{\mathrm{det}}(E)$ (Eq. 2.23, figure 3.7), yields an accurate model of the detector properties. It has the additional advantage that it is easily calculated or predicted. An example for a ^{6}Li-scintillator is given in appendix A.2.

4.3   Sample

The sample is modelled by combinations of simple geometric shapes (e.g. planes, spheres, boxes). Physical properties as material composition density are then assigned to each of the volumetric cells.

The description of the material composition consists of an enumeration of the occuring isotopes with their fractions. MCNPX contains the cross section data for all usual isotopes and combines them for a composed material. For this combination, the *free gas* approximation is used, i.e. the atoms are not combined to molecules, which changes the scattering cross sections. Only for a few materials (e.g. water, heavy water, polyethylene, graphite) the correct double differential cross section data $\mathcal{S}(\alpha, \beta)$ are implemented. There is a clear difference between the free gas approximation and the correct double differential cross sections in the thermal energy range (figure 4.2). Therefore, only the simulations of materials with the double differential cross sections are reliable. This is particularly true for the cold neutron spectra (cf. section 8.3.2).

Unfortunately, there are inaccuracies in the interpolation of the $\mathcal{S}(\alpha, \beta)$ scattering data [15]. This leads to the peaks in the angular distribution of the scattered neutrons, which exceed the statistical error of the Monte-Carlo simulation (figure 4.3). Particularly in the forward direction is a deep dip in the distribution of the scattered neutrons, which is not physical but it affects the simulation results of neutron radiographs. This simulation inaccuracy has to be taken into account for the scattering correction (cf. section 6.1).

4.4   Simulation Results

In this section two typical simulation results are described to show the capabilities of the MCNPX code. Many other simulations have been calculated, e.g. to verify that the influence of the air is negligible.
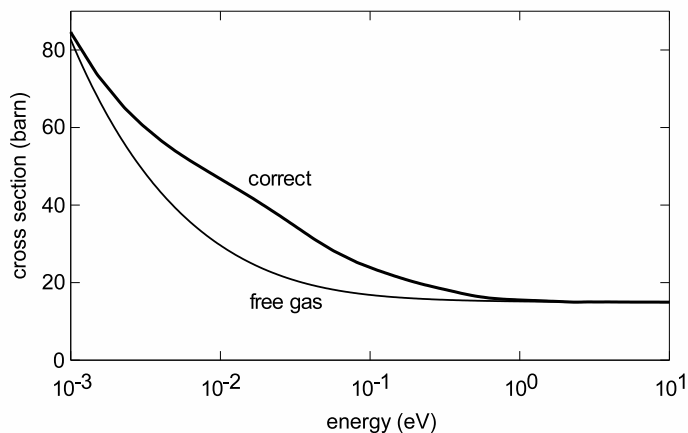
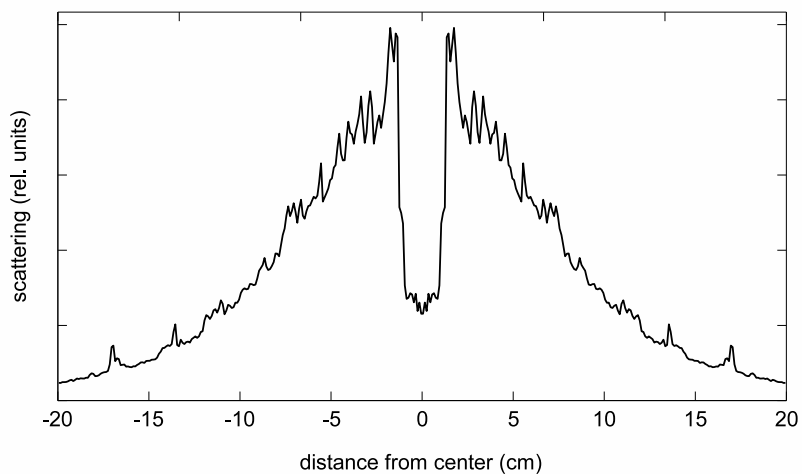Figure 4.2: Total microscopic cross section of water compared with the free gas approximation.

Figure 4.3: Simulated neutron scattering from a thin water layer to a plane detector in $10\,cm$ distance. The dip at the center and the peaks are physically not correct. Their height is several times larger than the standard deviation of the simulation results of about $1.5\,\%$.

Table 4.1: Experimentally measured and simulated water thicknesses and detector distances.

water thickness [mm]	detector distance [cm]					
0.97			5	10	15	20
1.91	2	3	5	10	15	20
3.00			5	10	15	20
4.99	2	3	5	10	15	20
6.94	2	3	5	10	15	20
9.97			5	10	15	20

4.4.1   Scattering of Water Layers

In order to get confidence into the simulation results, a set of radiographs of water layers is compared to the corresponding simulations. The thickness of the water layers varies between 1 and 10 mm and the detector distances between 2 and 20 cm (cf. table 4.1). The area of the water layer is around $4.4 \times 4.0 \, \text{cm}^2$. An example of an experimental result is shown in figure 4.4.

Some profiles of the flat field corrected experimental radiographs and simulation results are shown in figure 4.5. It is evident that the scattering contribution in the radiographs decreases with larger sample-detector distances, which is expected due to the divergence of the scattered neutrons. The skyshine and the build-up are hardly visible at the detector distance 5 cm, but the comparison to the 20 cm distance shows that there is still a significant amount of scattered neutrons in the radiographs. Only at 20 cm the profiles converge. This means that the contribution of the scattered neutrons can be neglected only for sample-detector distances, that are about five times larger than the extension of the sample perpendicular to the beam. Although the simulations reveal that for thick samples the scattering contribution is around 5 to 10 % of the measured transmission even in 20 cm distance. Therefore the scattering correction is necessary in order to obtain accurate quantitative results.

The experimental and simulated profiles in figure 4.5 run parallel. This shows that the scattering contribution is correctly simulated. But the measured absolute transmission is still higher than the simulated transmissions. Therefore, another contribution must exist in the experimental radiographs, which is not taken into account by the simulations. This unaccounted contribution is, however, quantita-
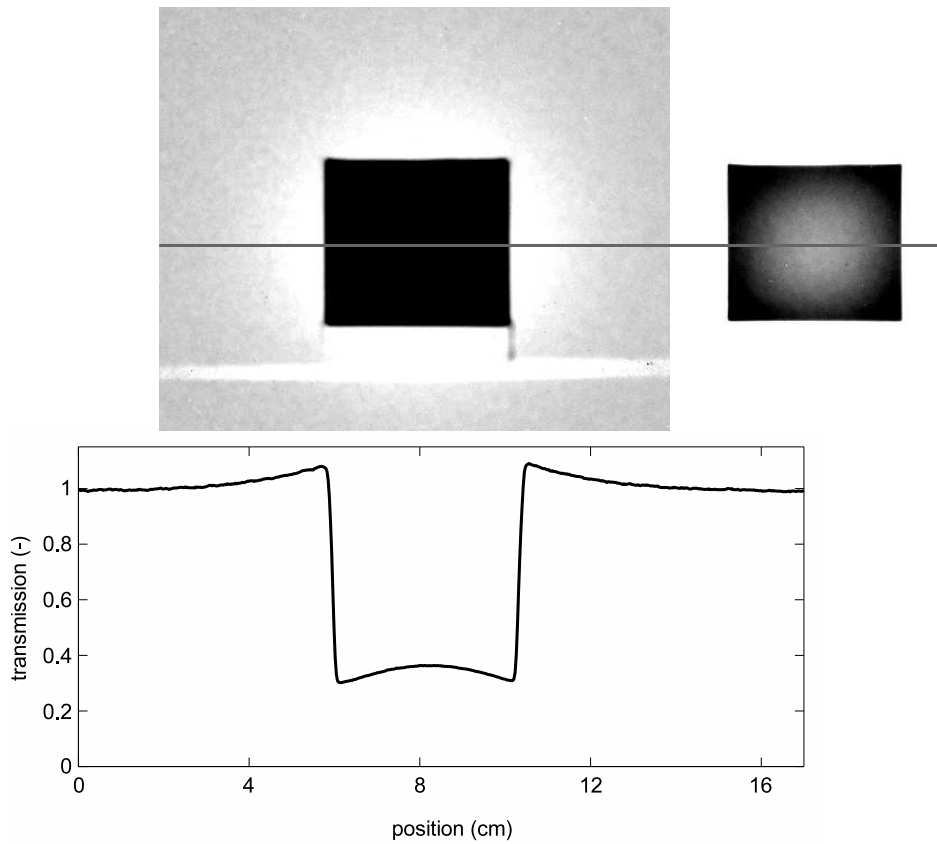
Figure 4.4: Radiograph of a water layer (thickness 7 mm, detector distance 2 cm) after the flat field correction with strong contrast settings to show the skyshine around the sample (left) and the build-up in the sample (right) due to the scattered neutrons. The graph (bottom) shows the horizontal profile of the experimentally measured transmission along the gray line.
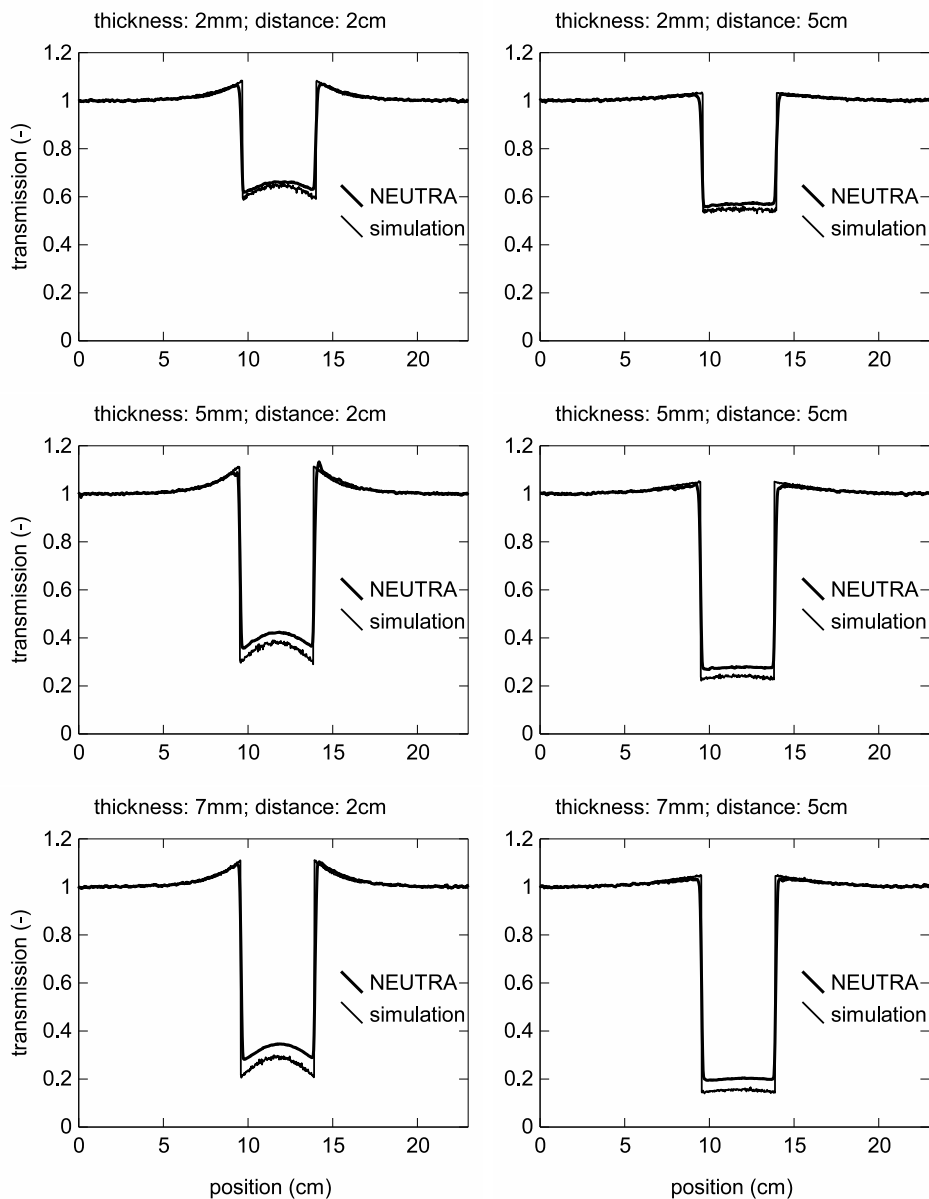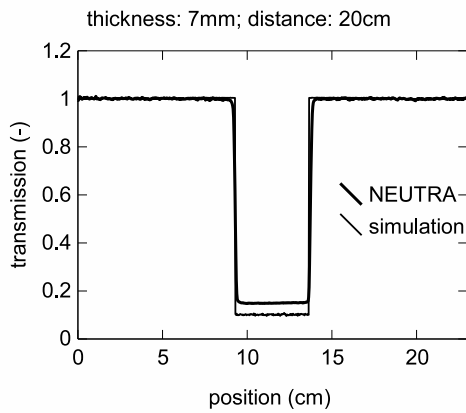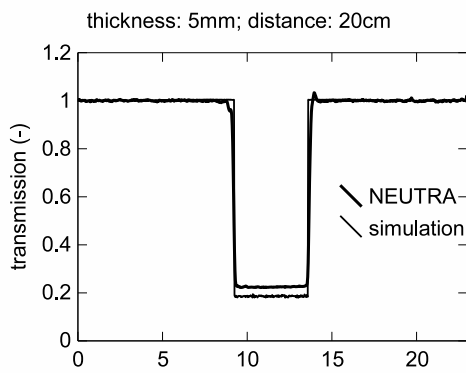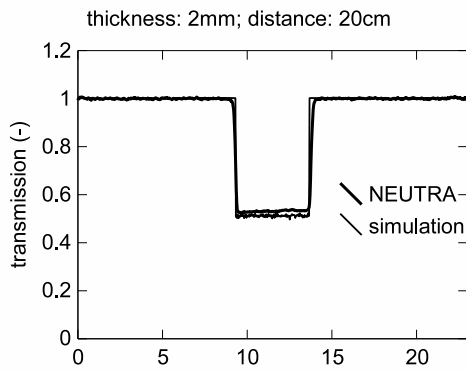
Figure 4.5: Comparison of the experimental radiographs and simulation results for the water thicknesses 2, 5, 7 mm and the sample-detector distances 2, 5, 20 cm (the simulated profiles are always the lower curves).

thickness: 2mm; distance: 20cm

NEUTRA
simulation

thickness: 5mm; distance: 20cm

NEUTRA
simulation

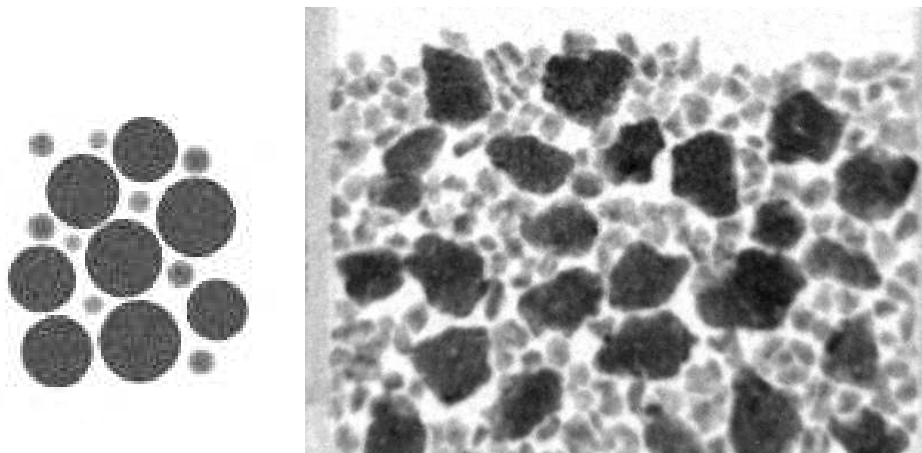thickness: 7mm; distance: 20cm

NEUTRA
simulation

Figure 4.6: Simulation of a radiograph of soil aggregates (left) compared to the real experiment (right). The contrast settings and the scales are identical for both images. The large aggregates in the simulation are cylindrical with a diameter of 6 to 8 mm and thickness 3 mm, the small aggregates are spheres with diameters 2 to 3 mm.

tively significant (cf. section 5.2).

4.4.2   Contrast of Soil Aggregates

To investigate the water flow between soil aggregates, an experiment has been carried out, where large aggregates with a high water content are in contact with small aggregates with a lower water content. It has not been clear in advance what water contents will be distinguishable because of the neutron scattering, the noise, and the limited image resolution in the real experiment. Therefore an experimental setup of soil aggregates with water contents between 20 and 42 % (by volume) has been simulated. The finding is that differences of 1 % in water content are distinguishable. Figure 4.6, left shows a simulation where the big aggregates contain 42 % water and the small aggregates 40 %.

The experimental radiograph corresponds with the expected neutron attenuation. It shows how the water is exchanged between the aggregates. The quantitative results of this measurement are used to model the water content of the aggregates as a function of time and distance from the aggregate surface, until the equilibrium has been reached [16].

Chapter 5

Distortions of the Quantitative Information

The "ideal" neutron radiograph to be used for quantification would be a transmission image, which exactly obeys the exponential law of attenuation (Eq. 2.11) with a monoenergetic neutron beam. There are various reasons, why this assumption does not hold.

The main deviations from ideality originate from the neutron scattering. Neutrons passing the sample can be scattered and hit the detector. This *sample scattering component* appears as an extra intensity in the radiographs, that is being interpreted as reduced attenuation or as lower mass density of the material, respectively. But also the neutrons missing the sample can be scattered at the surrounding of the sample (e.g. the camera box) or at the neutron shielding. Also this *background scattering component* causes an extra intensity on the detector.

Further deviations from the exponential law of attenuation are due to the fact that a neutron beam for radiography is usually polyenergetic. Although it is possible to delimit the energy range, it is often not applicable because of the increased exposure time. Since the cross sections usually decrease with increasing neutron energies, *beam hardening* effects have to be expected, i.e. the effective attenuation coefficient decreases with the sample thickness because of the increasing weight of the high energy neutrons in the effective cross section (cf. Eq. 2.29). But also the *energy dependent detector efficiency* has to be taken into account, because the neutron spectrum behind and in front of the sample are not the same.

The four effects mentioned above are taken into account by the correction algo-

rithm presented in this thesis. In this chapter they are described in detail. There are of course additional effects disturbing the quantification, which are of minor importance and are not discussed here, as e.g. the beam divergence or the limited detector resolution.

5.1 Neutron Scattering in the Sample

The neutron scattering in the sample depends on the material composition, density, the sample dimensions and the neutron energy. The cross section σ of some elements, as e.g. hydrogen, consists mainly of scattering contributions ($\sigma_{\mathrm{s}} = \sigma_{\mathrm{coh}} + \sigma_{\mathrm{inc}}$, cf. section 2.1.2), while for other elements such as gold, the absorption cross section σ_{a} is dominant.

Figure 5.1 shows the total amount of scattered neutrons directly behind a planar layer of a given material. The curves are obtained by simulations. There is a clear material dependence, which correlates to the contribution of the scattering cross section to the total cross section ($\sigma_{\mathrm{s}}/\sigma_{\mathrm{tot}}$). Of course, for thin layers the amount of scattered neutrons on the detector increases with the sample thickness, because more scattering events occur. But there is a maximum at about one to two mean free path lengths. Beyond this the scattering component measured by the detector decreases again. This is called the *self shielding*. In thick samples the probability for multiple scattering becomes large and therefore the number of neutrons passing through the whole sample decreases. It becomes more probable that a neutron is absorbed on its path through the sample or scattered backwards out of the sample.

The neutrons scattered by the sample are spatially smoothly distributed on the detector. The amount of scattered neutrons in each detector pixel depends not only on the sample thickness as mentioned above, but also on the distance between sample and detector. The width of the scattering distribution is mainly a function of the detector distance.

The comparison to the expected exponential attenuation shows that the scattering component of a radiograph exceeds the component of the uncollided beam for thicknesses beyond one to two mean free path lengths and small sample-detector distances (cf. figure 5.1). But even for smaller thicknesses the sample scattering is a significant contribution in the radiographs and should not be neglected in order to obtain quantitative results.
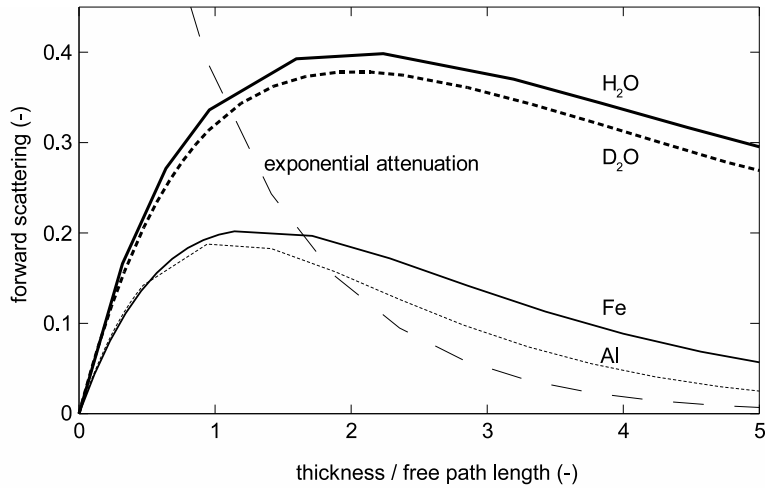
Figure 5.1: Amount of scattered neutrons directly behind a planar material layer (simulated). The thickness axis is in units of mean free path lengths, in order to obtain comparable scales. The scattering axis is in fractions of the incident neutron beam. The dashed line shows the expected exponential attenuation for comparison.

5.2 Neutron Scattering by the Experimental Setup

It is known from many experiments, that are supposed to yield quantitative results that the sample scattering is not the only disturbing neutron contribution in the radiographs (cf. section 4.4.1). A *background scattering* contribution has been demonstrated by systematically placing and removing shielding material around the scintillator. This background scattering is divided into two components.

The first component consists of neutrons, that cannot reach the detector directly, but are scattered e.g. at the shielding or at the borders of the camera box and hit the detector. These neutrons can be blocked by limiting the beam size to the size of the detector. At the NEUTRA facility the optimal method for this is an aperture in the collimator and an additional cadmium window at the end of the collimator.

The second component are neutrons, that pass through the scintillator and are backscattered from the mirror to the scintillator. As the absorption rates in figure 3.7 show, most neutrons are not absorbed but can penetrate a Li-scintillator and hence can be backscattered. The backscattering from the camera box has been investigated in further experiments. In figure 5.2 the line profiles of a partially shielded open beam recording are presented. The measured gray values behind the
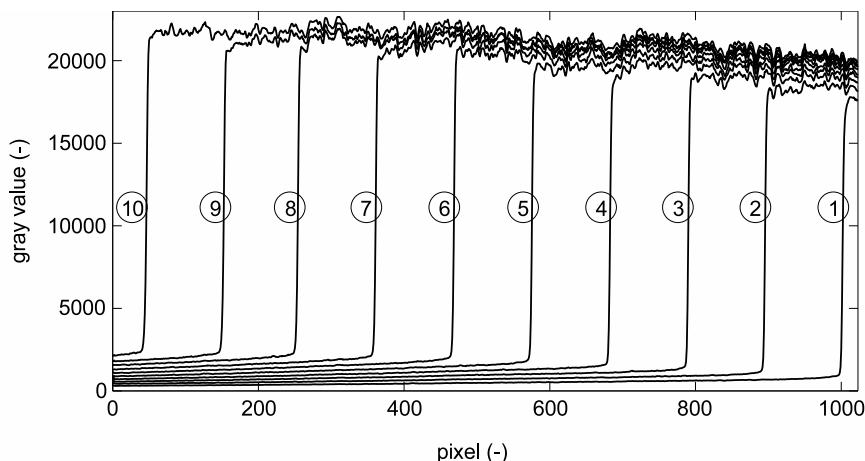
Figure 5.2: Line profiles of an open beam recording, that is partially covered with a 5 cm thick boron plastic shielding block (left). The backscattered neutrons cause an intensity behind the shielding and also in the open beam area. The shielding has been stepwise moved from right to left, opening the detector plane (the curve labels indicate the step number).

shielding represent the backscattering component. Apparently, the background scattering increases with the opening of the beam. Of course, the background scattering is not only behind the shielded area, but also in the open beam area. Therefore also these values increase with the opening of the beam. In this experimental setup, the backscattering component is up to 10 % of the open beam gray values. Hence also this is a significant contribution disturbing the quantification and is of the correct order of magnitude to explain the differences found in the water layer radiographs compared to the simulations (figure 4.5).

To be sure that this is a neutronic effect instead of light scattering, an additional experiment has been performed. Figures 5.3(a) and (b) show the setup, where the scintillator is shielded on the left hand side with boron carbide. On the right hand side it is open to the neutrons, but the produced light is blocked once by a aluminum plate (a) and once by a gadolinium plate (b). Both a Li- and a Gd-scintillator have been used for this experiment.

The profiles in figure 5.3 show the results with the Al- (left) and the Gd-plate (right) as light shielding. For the Li-scintillator with the Al-plate (c), a similar profile as in the previous experiment is recorded. With the Gd-plate still the same amount of light is produced, but the neutrons are prevented from being

backscattered from the camera box to the scintillator (e). This is observed in the experiment, since the profile approximates to the background value where the scintillator is completely shielded. Hence, the recorded backscattering component is a neutronic effect. The peak in the profile with the Gd-cover is due to the (n,γ) reaction in the gadolinium. The LiF/ZnS-scintillator is not only sensitive on neutrons, but also on the produced γ-radiation.

The profiles measured with the Gd-scintillator are almost identical for the Al- and the Gd-cover (figures 5.4(d) and (f)). The reason for this is that the Gd- scintillator itself absorbs almost all the neutrons, so that for both covers the mea- sured backscattering is nearly the same as for the completely shielded scintillator. This finding might suggest that the Gd-scintillator is a better choice for quanti- tative neutron radiography than the Li-scintillator. But as the wide peak at the border to the Gd-cover shows, the γ-particles produced by the detector reaction affect a large neighborhood of the effective event. Therefore edges are blurred and a quantification is not possible. This is in agreement with the profiles shown in figure 3.8, where the edges are round and the transmission values are dominated by the γ-background.

## 5.3   Beam Hardening and Detector Efficiency

Figure 5.4 shows how the energy spectrum of the uncollided neutron beam changes through $1\,\mathrm{cm}$ water. Since the cross section of water increases for the low energy neutrons, the mean neutron energy is shifted to higher energies. This effect is called *beam hardening.* Therefore the effective attenuation coefficient for a thick sample is less than for a thin sample. As a consequence, the attenuation coefficient in the exponential law of attenuation depends on the sample thickness s (cf. Eq. 2.29):

$$
\begin{aligned}
\Sigma_{\mathrm{eff}}(s) &= \frac{-1}{s} \log\left(\frac{\Phi}{\Phi^{\mathrm{ob}}}\right) \\
&= \frac{-1}{s} \log\left(\frac{\int \Phi^0(E) \exp\left(-\Sigma(E) \cdot s\right) \mathrm{d}E}{\int \Phi^0(E) \, \mathrm{d}E}\right) \quad,
\end{aligned}
\tag{5.1}
$$

where the detector absorption rate is set to $A^{\mathrm{det}}(E) = 1$, in order to separate the effects of the sample and the detector. This thickness dependent effective attenuation coefficient is compared to the constant value $\Sigma_{\mathrm{eff}} = \lim_{s\to 0} \Sigma_{\mathrm{eff}}(s)$, to specify the impact of the beam hardening for the quantification.
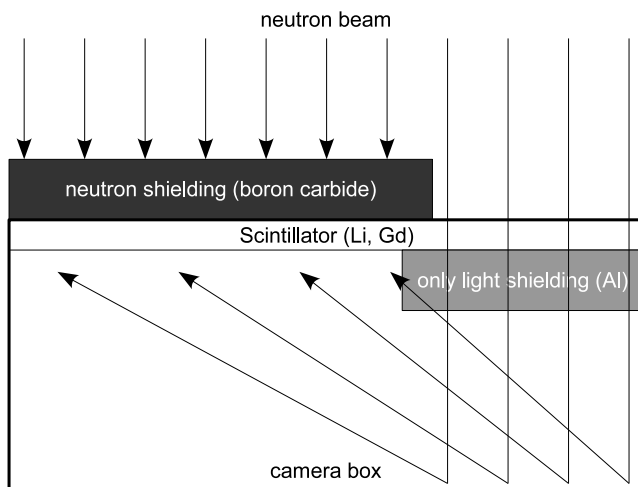
(a) Experimental setup with the Al cover
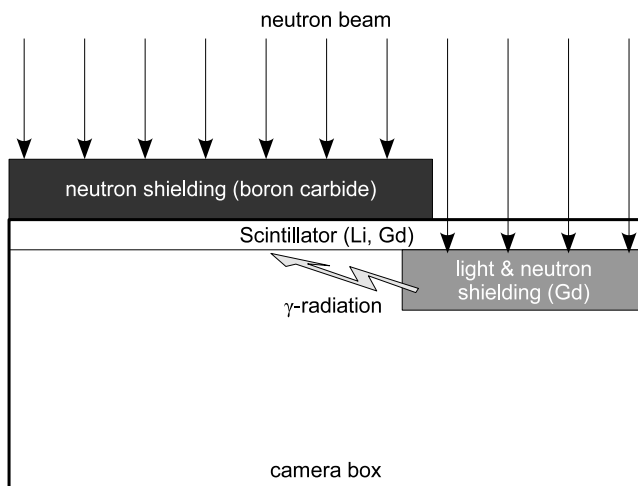
(b) Experimental setup with the Gd cover

Figure 5.3: Experimental setup for the verification of the backscattering component from the camera box and the resulting backscattering profiles. On the right hand side the scintillator can detect the neutrons, but the light is blocked. Top: An aluminum cover blocks the light but is transparent for neutrons. They can pass and be backscattered to the left hand side of the scintillator. Since the direct beam is blocked there, only the backscattered neutrons are detected. Bottom: A gadolinium cover blocks the light and also the neutrons. The diagrams contain the profiles as well as the open beam intensity and the background intensity behind a scintillator, that is completely shielded against neutrons.
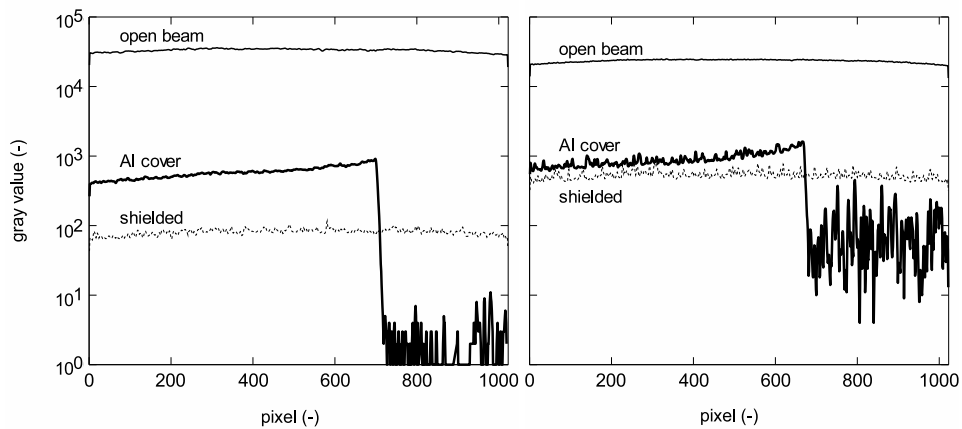
(c) Li-scintillator, Al cover

(d) Gd-scintillator, Al cover
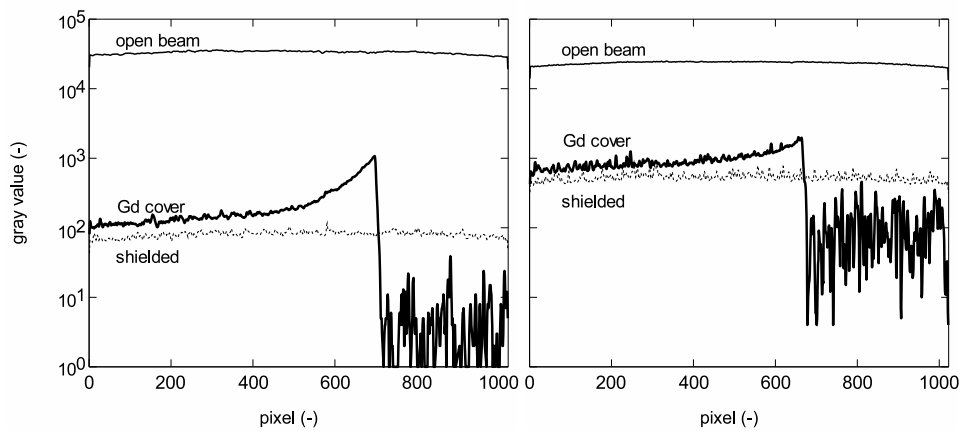
(e) Li-scintillator, Gd cover

(f) Gd-scintillator, Gd cover
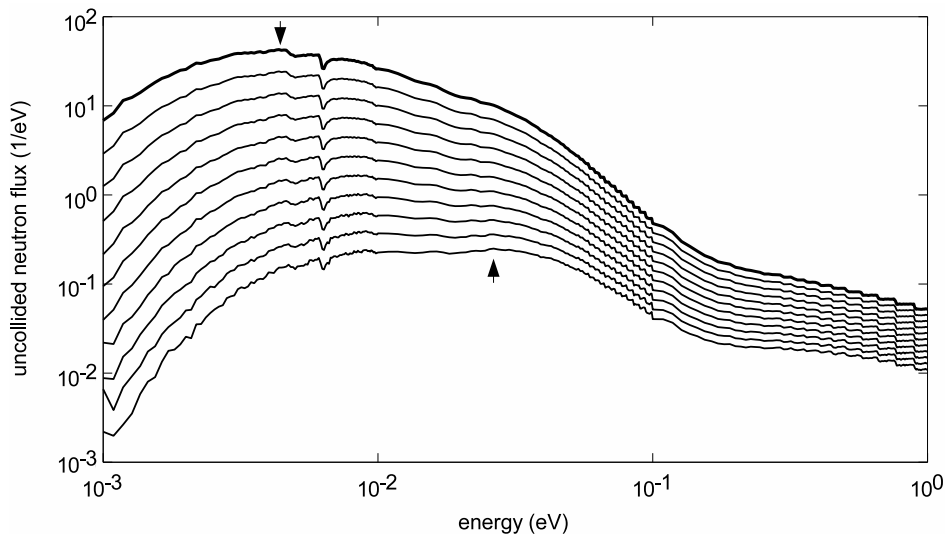
Figure 5.4: Energy spectrum of the ICON facility (thick line) compared to the simulated spectrum of the uncollided neutrons behind 1, 2, 3, ..., 10 mm water (thin lines, from top to bottom). The thickness 10 mm water corresponds to 3.8 mean free path lengths. The arrows mark the shift of the maximum flux to higher energies.

$$\Sigma_{\text{eff}} = \lim_{s \to 0} \Sigma_{\text{eff}}(s) = \frac{\int \Phi^0(E)\Sigma(E)\,\mathrm{d}E}{\int \Phi^0(E)\,\mathrm{d}E} \tag{5.2}$$

In a similar way the constant value for the mean free path length is defined as

$$\lambda = \frac{1}{\Sigma_{\text{eff}}} \quad . \tag{5.3}$$

Figure 5.5 shows the decreasing effective attenuation coefficients for iron, water and cadmium. While iron causes almost no beam hardening (1 %), the attenuation coefficient for water and cadmium decreases by about 11 resp. 28 % within three mean free path lengths in the NEUTRA spectrum. In the ICON spectrum it is even 4 % for iron, 22 % for water and 50 % for cadmium. These values are calculated by the numerical solution of Eq. 5.1 and confirmed also by the statistical method of the Monte-Carlo simulations.

The results make clear that it is absolutely necessary to take the beam hardening into account for an accurate quantification of neutron radiographs or tomograms.

Since the energy spectrum of the transmitted neutron beam is changed by the sample and the detector sensitivity is energy dependent, it is not enough to consider
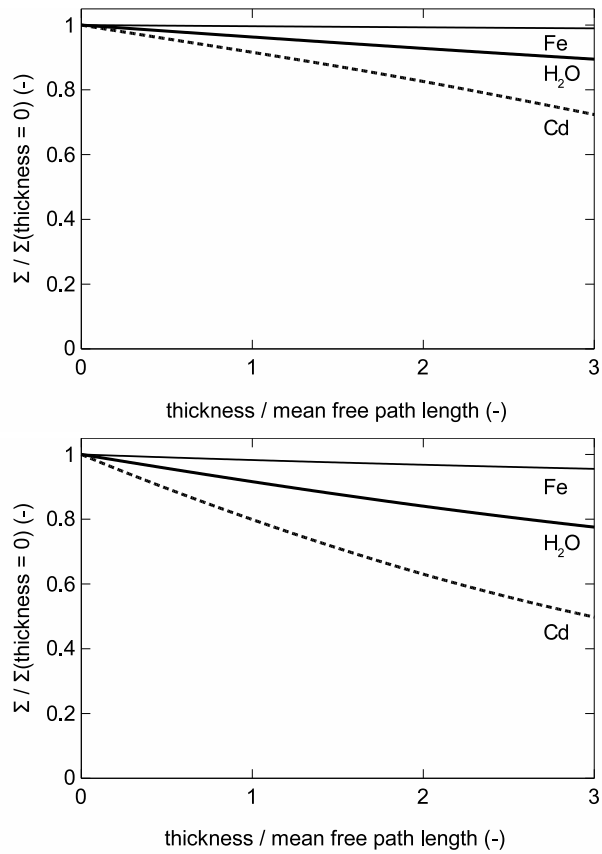
Figure 5.5: Impact of the beam hardening to the effective attenuation coefficient for the NEUTRA (left) and ICON spectrum (right), calculated according to Eq. 5.1. The axes are in relative units, so that the materials are comparable, although their absolute attenuation coefficients and thicknesses differ.

only the beam and sample properties for the calculation of the effective attenuation coefficient Σ_{eff} as in Eq. 5.1. Also the absorption rate $A^{\text{det}}(E)$ (cf. section 2.1.3) must be taken into account, yielding Σ_{eff} as described in Eq. 2.29 (in the ideal case, the intensity of the open beam image and sample image is the same, i.e. $f^{\text{ob}} = 1$).

$$\Sigma_{\text{eff}}(s) = \frac{-1}{s} \log \left(\frac{\int \Phi^0(E) \cdot \exp\left(-\Sigma(E) \cdot s\right) \cdot A^{\text{det}}(E) \, dE}{\int \Phi^0(E) \cdot A^{\text{det}}(E) \, dE} \right) \tag{5.4}$$

The effect of the different absorption rates is shown in table 3.2 for water as an example. It is in the range of 5 to 10 % and therefore also significant for an accurate quantification.

Chapter 6

Correction Algorithm

In chapter 5 the main effects disturbing the quantitative information are identified. The best correction is always to avoid the disturbances by a suitable experimental setup. Although this is mostly possible for all the mentioned effects, it is not always feasible. The neutron scattering at the surroundings of the sample can be reduced almost completely by a well adjusted limitation of the beam size. But even then the remaining scattering contribution should be subtracted from the radiographs. The neutrons scattered in the sample can be filtered by a grid of small collimators between sample and detector. Such a collimator has been tested just before finishing the experiments for this thesis, but the results are not satisfying because the scattering of the collimator itself is as large as that of the sample. Therefore the completely computational correction method with the point scattered functions is proposed here. Nevertheless, it is worth to follow this approach and potentially develop it to an experimental component of the scattering corrections. The beam hardening can be avoided experimentally by filtering a single energy from the neutron beam with an energy selector. But this increases the exposure times and is not feasible for time critical measurements or tomograms with hundreds of projections.

The described disturbing effects are all induced by the neutrons themselves and become apparent in every radiograph. Therefore also for tomograms the correction algorithm is performed on the radiographic level. If all projections of a tomogram are corrected, the reconstruction algorithm will yield a tomogram with the correct attenuation coefficients.

The correction of neutron radiographs in order to allow quantitative evaluations is not only an academic problem, but it should be applied in the daily use at all

neutron radiography facilities. This means that it is not feasible to simulate every experiment in order to distinguish the different physical effects in a radiograph. Rather the whole experiment should be described by a few parameters as an input for the correction algorithm, which provides then the corrected radiograph. This practical approach is a basic precondition for the method described here.

6.1   Neutron Scattering in the Sample

As described in section 5.1, the neutron scattering in the sample is a major source of error for the quantification. Moreover, it is a neighbourhood effect, i.e. the neutrons scattered at one point of the sample affect the whole radiograph. Furthermore, it depends on the potentially complex geometry and composition of the sample and the angularly dependent cross sections. For these reasons an effective and feasible correction of the sample scattering must be based on simplifications.

The method described here is based on *Point Scattered Functions* (PScF). The PScF is the probability density for a neutron from a point-like, directed source to be scattered at a homogeneous material layer and to be registered by the detector (figure 6.1) [17, 18]. For the correction of the sample scattering the following steps are performed:

1. The sample is described, i.e. the corresponding material and sample-detector distance are assigned to every pixel of the radiographic image.

2. With this information a first estimation of the material thickness is computed from the uncorrected radiograph.

3. The algorithm calculates then the appropriate PScF, which is in general different for every pixel. The PScF are scaled by the open beam value and multiplied by the pixel area, yielding the scattering contribution of every pixel.

4. All these scattering contributions are subtracted from the original radiograph resulting in an image that is corrected for the sample scattering.

5. The steps 3 and 4 are repeated iteratively until the total scattering cloud remains unchanged within given limits.
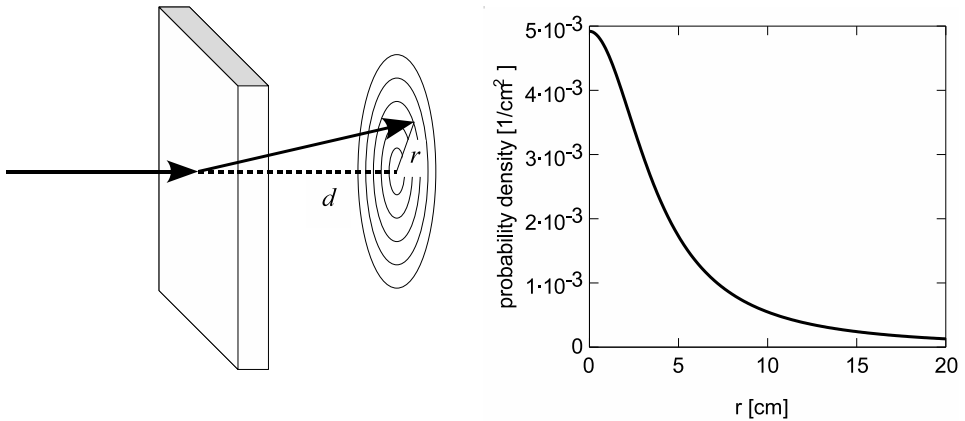
Figure 6.1: Arrangement for the simulation of the PScF and the resulting approximated distribution of the scattered neutrons, measured by a ^{6}Li-detector $5\,\mathrm{cm}$ behind a $5\,\mathrm{mm}$ thick water layer.

6.1.1 Simulation of the PScF

The PScF depend on the material composition, thickness and density, the sample-detector distance and the detector material, thickness and density. The lateral extension of the material layer is chosen to be very large compared to the detector distances and mean free path lengths, so that no edge effects occur in the simulated PScF. Although they exist in reality, they differ for every experiment. Therefore, they are neglected to avoid potential artefacts induced by the correction algorithm.

A PScF is a probability density, that is composed of the two probabilities, i.e. the scattering event (p_{scat}) and the detection event (p_{det}). Both probabilities are functions of the detector distance d and the radial distance r. The scattering probability is of course related to the angularly dependent cross sections σ_{s} (cf. section 2.1.2), but it depends mainly on the geometric effect that the increment of the scattering angle $r\,\mathrm{d}\theta$ is less than the increment of the radial distances $\mathrm{d}r$ (cf. figure 6.2 left)

$$r\,\mathrm{d}\theta = \cos\theta \cdot \mathrm{d}r = \frac{d}{\sqrt{d^2 + r^2}} \cdot \mathrm{d}r \quad . \tag{6.1}$$

Also the detection probability depends on the scattering angle, because the scattered neutrons do not hit the detector perpendicularly. Therefore the path length through the detector is larger than the detector thickness s^{det} and the absorption rate A^{det} higher (cf. figure 6.2 right, Eq. 2.23)
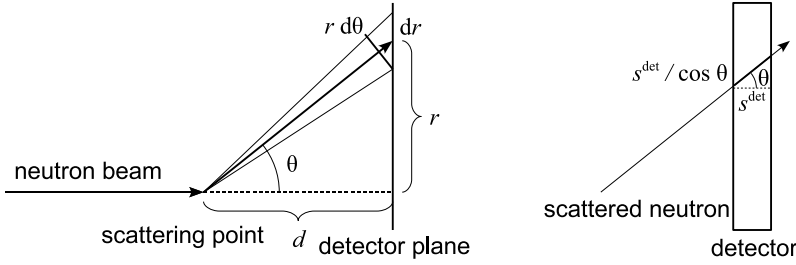
Figure 6.2: Left: relation between dθ and dr. Although the neutrons are scattered approximately isotropic in dθ, the measured neutron flux through the detector plane decreases with the distance r from the center. Right: The path length of a scattered neutron is longer than the detector thickness. Therefore the absorption rate increases for scattered neutrons.

$$A^{\mathrm{det}}(E,\theta) \;=\; 1 - \exp\left(-\Sigma_{\mathrm{a}}^{\mathrm{det}}(E)\cdot s^{\mathrm{det}}/\cos\theta\right) \tag{6.2}$$

$$\;=\; 1 - \exp\left(-\Sigma_{\mathrm{a}}^{\mathrm{det}}(E)\cdot s^{\mathrm{det}}\cdot \frac{\sqrt{d^2+r^2}}{d}\right) \quad. \tag{6.3}$$

Unfortunately, MCNPX provides only independent energy and angle multipliers for the neutron tallies. Therefore it is not possible to simulate the angularly dependent absorption rate exactly. The problem is circumvented by simulating the PScF without the angular dependence of the detector sensitivity (i.e. $\theta = 0$ resp. $r = 0$ in Eq. 6.3), but with the energy dependence. The angular dependence is taken into account after the simulation for the mean of the whole neutron spectrum. Since the thermalized neutron spectrum will remain approximately constant by the scattering processes, the error by this simplification is only small (cf. section 6.1.4).

The PScF are computed with a simulated setup as shown in figure 6.1. The neutron source is modelled as a unidirectional point source, with the energy spectrum taken directly from the time-of-flight measurement if available. Otherwise it is taken from simulation results or approximations to a Maxwell spectrum.

The sample composition is described as accurately as possible by the occurring isotopes and their fractions. In general MCNPX provides cross section data for all naturally existing isotopes, but as free gas models. Because the molecular composition and atomic structures are neglected in this model, the cross sections are mostly approximations and always independent of the azimutal scattering angle φ due to coherent scattering (cf. section 2.1.2). For some common materials as
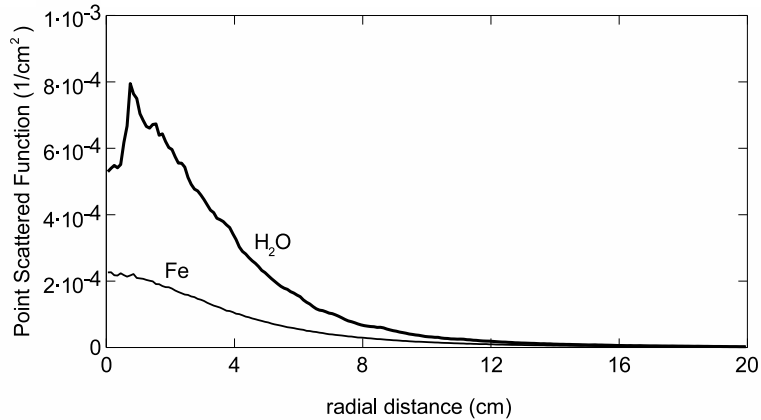
Figure 6.3: Simulation results for the PScF of water and iron in the NEUTRA spectrum, with the thickness 5 mm and a ^{6}Li-detector 5 cm behind the material layer.

e.g. water the double differential cross sections $\mathcal{S}(\alpha, \beta)$ are available, which provide exact results.

Because the simulated scattering is always independent of the azimutal scattering angle, the geometry of the detector is modelled as concentric rings around the uncollided beam with the radii $r = 0.1, 0.2, ..., 20$ cm (cf. figure 6.1). Since the energy dependence (Eq. 6.3) is just a multiplier for the tally, the neutrons cross the detector plane undisturbed. This allows to simulate multiple detector planes in the distances $d = 1, 2, \ldots, 20$ cm behind the sample at once.

With that arrangement, only one input file and simulation run is required per combination of material composition, sample thickness, energy spectrum and detector type. In order to know the detector response of the open beam, it is necessary to simulate also an undisturbed beam with the same spectrum and detector type. The MCNPX input file is described in detail in appendix A.3.

Two typical results of the simulated PScF are shown in figure 6.3. The PScF of water looks very irregular and has a deep dip at the center ($r = 0$). These variations are beyond the statistical error of the simulation, which is less than 1%. They are caused by inaccuracies in the MCNPX interpolation algorithm of the $\mathcal{S}(\alpha, \beta)$ scattering data [15]. The free gas model of iron provides a very flat curve, but it neglects the Bragg edges due to the atomic structure.

6.1.2   Approximation of the PScF

Of course, the PScF can only be simulated for a discrete set of material thicknesses
and detector distances, and also the detector resolution is given. Therefore these
data cannot be used directly for the correction of a real radiograph, where the
sample thickness, detector distance and image resolution have arbitrary values. In
order to obtain the PScF values for such arbitrary values, the simulated PScF are
approximated by analytical functions, that are based on isotropic scattering in one
point. The approximated PScF is described by the equation (cf. figure 6.2)

$$
\begin{aligned}
\mathrm{PScF}_{\mathrm{A}}(r) &= S_{\mathrm{A}} \cdot \frac{1}{4\pi\,(d_{\mathrm{A}}^2 + r^2)} \cdot \cos\theta \\
&= S_{\mathrm{A}} \cdot \frac{d_{\mathrm{A}}}{4\pi\,(d_{\mathrm{A}}^2 + r^2)^{3/2}} \quad ,
\end{aligned}
\tag{6.4}
$$

where S_{A} is the scattering intensity, d_{A} the distance between the scattering
point and the detector and r the radial distance from the center of the detector
(figure 6.2). The approximated detector distance d_{A} does not have to be equal
to the geometric distance between sample and detector, because in reality the
scattering is not isotropic and multiple scattering occurs for thicker samples. If
e.g. forward scattering is preferred, d_{A} will be smaller than the geometric distance.

Another approximation concerns the material density: it assumes that the pa-
rameters S_{A} and d_{A} depend only on the *mass thickness* (i.e. the product of the
sample density times the sample thickness) instead of its components separately.
With that the PScF have to be simulated for only one typical density.

Figure 6.4 shows the good correspondence of the simulated and approximated
PScF for water and iron. For the presented PScF of iron, the standard deviation
between the simulated and approximated values is $1.94 \cdot 10^{-6}$. This is about $1\,\%$
of the PScF values and about the same as the statistical error of the simulation.
Therefore the differences of the iron curves are hardly visible.

In order to get rid of the unphysical dip at $r \gtrsim 0$ in the water PScF, these values
are just neglected for the approximation. This yields a relative standard deviation
of about $5\,\%$ between the simulated and approximated PScF.

For every simulated PScF, the approximation is computed. This results in a
pair of approximation parameters S_{A} and d_{A} for each combination of neutron spec-
trum, detector type, material composition, sample thickness and detector distance.
Within one radiograph, of course the neutron spectrum and detector type is given.
Also the material composition at each pixel is given as a user input for the correction
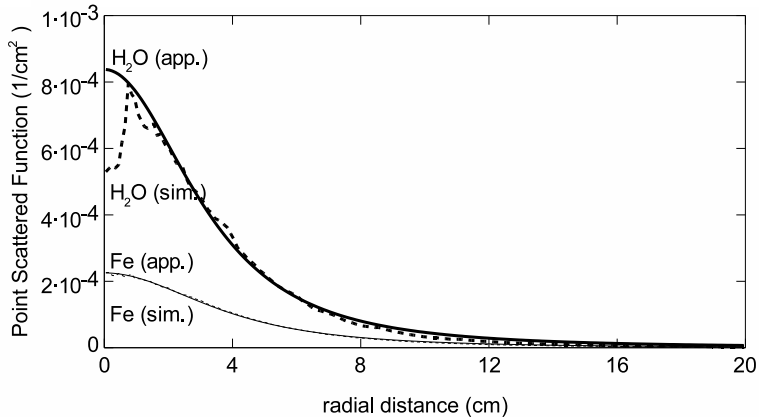
Figure 6.4: Dashed lines: Simulation results for the PScF of water and iron as in figure 6.3. Solid lines: The corresponding approximations of the simulated PScF, based on isotropic scattering (Eq. 6.4).

algorithm (for details see also section 6.1.6). Hence, the approximation parameters S_A and d_A are functions of the continuous experimental parameters sample thickness s and detector distance d. The correction algorithm interpolates $S_A(s, d)$ and $d_A(s, d)$, that are known for the simulated set of discrete thicknesses and distances, to the given experimental thickness and distance. Thus, the approximated PScF can be computed for an experimental setup.

Since the approximation parameter $S_A(s, d)$ is almost (but not completely) independent of the detector distance d and vice versa $d_A(s, d)$ is almost independent of the sample thickness s, the numerical approximation by the used gradient-expansion algorithm is not very stable. For this numerical reason, the approximated PScF (Eq. 6.4) is rewritten in terms of the height h and width w (half width at half maximum) of the graph

$$PScF_A(r) = h \cdot \frac{w^3}{\left(w^2 + \left(2^{2/3} - 1\right) \cdot r^2\right)^{3/2}} \quad , \tag{6.5}$$

where the physical parameters S_A and d_A are substituted by

$$S_A = 4\pi h \cdot \frac{w^2}{2^{2/3} - 1} \tag{6.6}$$

$$d_A = \frac{w}{\sqrt{2^{2/3} - 1}} \quad . \tag{6.7}$$

In the implemented correction algorithm, the mathematical parameters h and w

are approximated and linearly interpolated in order to obtain the approximated PScF.

6.1.3   Parameterization of the PScF

Although the correction with the approximated PScF is efficient and accurate, it would be even more elegant to have only one algebraic function of the PScF for all sample thicknesses s and sample-detector distances d, i.e. only one function per combination of neutron spectrum, material and detector type. Then it would not be necessary to have tables for the PScF approximation parameters and to interpolate them. Rather the PScF could be calculated by a single function, which would also increase the calculation performance. This parameterization method is presented in the following for the example of water in the NEUTRA spectrum, measured with a Li-scintillator. The same method applies also for other materials, spectra or scintillator types.

In figure 6.5 (top) the approximated distance d_A is plotted versus the simulated sample-detector distance d for several thicknesses s of a water layer. It is obvious that they are linearly correlated and can be described by

$$d_P(s, d) = m(s) \cdot d + a(s) \quad , \tag{6.8}$$

where the slope $m(s)$ and the axis intersect $a(s)$ are functions of the water thickness s. In the PScF equation 6.4 the interpolated values for d_A are then replaced by the parameterized distance $d_P(s, d)$.

The slope $m(s)$ and axis intersect $a(s)$ of the straight lines $d_P(s, d)$ are plotted as functions of the water thickness s in figure 6.5 (bottom). The slope $m(s)$ is approximated by a third order polynomial, while the axis intersect $a(s)$ is again approximated by a liner function.

Figure 6.6 (left) shows the approximated scattering intensities S_A as functions of the water thickness for the detector distances 1, 2, ..., 20 cm. It seems justified, to consider these twenty graphs as coinciding and hence independent of the simulated detector distance d. Therefore the parameterized scattering intensity $S_P(s)$ is just a function of the material thickness. A good approximation is given by the function

$$S_P(s) = S_{P,max} \cdot \frac{s}{s_{P,max}} \cdot \exp\left(\frac{1}{c} \left(1 - \left(\frac{s}{s_{P,max}} \right)^c \right) \right) \quad . \tag{6.9}$$

It is based on the term $As \cdot \exp(-Bs)$, but reformed, so that the parameters $S_{P,max}$ is the maximum of the parameterized scattering intensity at the position $s_{P,max}$.
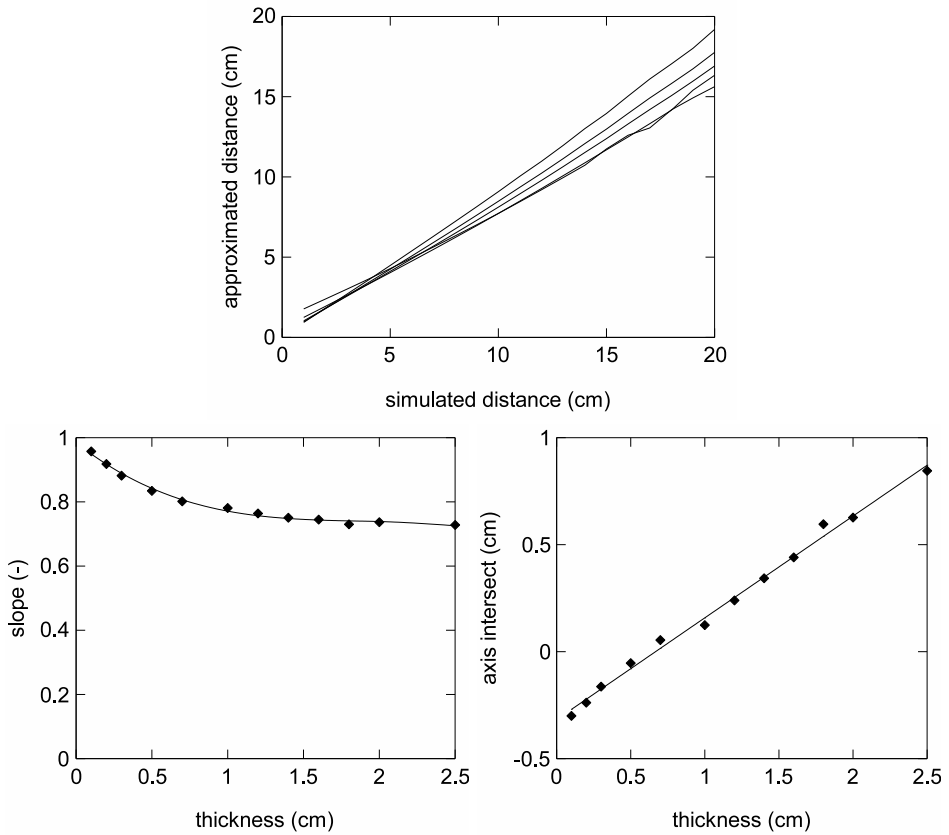
Figure 6.5: Top: the approximated distance d_A as a function of the simulated detector distance d for the PScF of water in the NEUTRA spectrum with a Li-scinitllator. The different curves are for the water layer thicknesses $s = 1, 3, 5, 10, 20$ mm (top to bottom).

Bottom: the slope (left, dots) and axis intersect (right, dots) of the parameterized distances d_A in the top graph. The slope is approximated by a third order polynomial and the axis intersect by a linear function (lines).

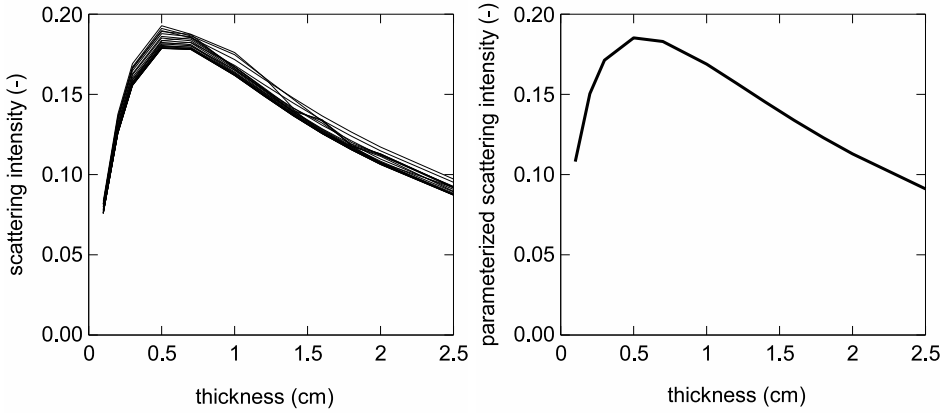Figure 6.6: Left: the approximated scattering intensities S_A as a function of the material thickness s for the simulated detector distances $1, 2, \ldots, 20\,\text{cm}$ for the PScF of water in the NEUTRA spectrum with a Li-scintillator. Right: the parameterized scattering intensity $S_P(s)$ for the same PScF.

The third parameter c affects mainly the slope of the curve beyond the maximum. These three parameters for the scattering intensity S_P are easily identified. The shape of the scattering intensity curve is clearly correlated to the total amount of scattered neutrons behind a material layer, as described in section 5.1. For thin thicknesses, the amount of scattering increases with the thickness up to a maximum. Beyond that, the self shielding becomes dominant and the amount of neutrons scattered in the sample and hitting the detector decreases again.

All together, the parameterized PScF is given by the equation

$$\text{PScF}_P(r) = S_P(s) \cdot \frac{d_P(s,d)}{4\pi \left(d_P(s,d)^2 + r^2\right)^{3/2}} \tag{6.10}$$

with the parameterized scattering intensity $S_P(s)$ given by Eq. 6.9 and the distance

$$
\begin{aligned}
d_P(s,d) &= m(s) \cdot d + a(s) \\
&= \left(m_3 s^3 + m_2 s^2 + m_1 s + m_0\right) \cdot d + (a_1 s + a_0) \quad . \tag{6.11}
\end{aligned}
$$

The parameterized PScF of water and iron are compared to the simulated PScF in figure 6.7.

With this parameterization, the whole scattering for a material in a certain neutron spectrum and detected by a certain detector is determined by the nine parameters $S_{P,\max}$, $s_{P,\max}$, c, $m_0, \ldots, m_3$, a_0 and a_1. Furthermore the linear
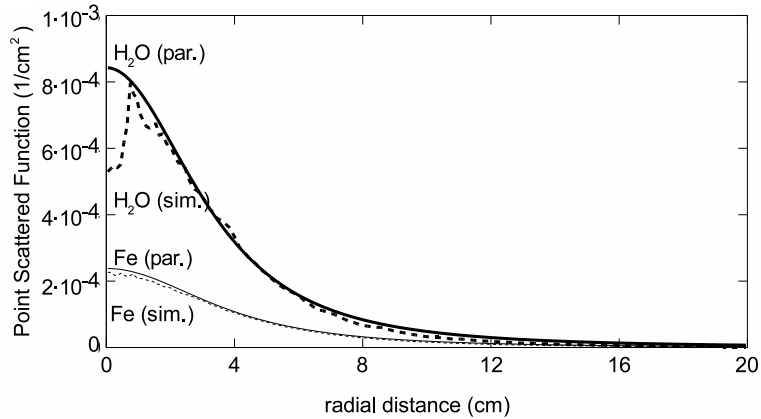
Figure 6.7: Comparison of the simulation and parameterized results for the PScF of water and iron (same conditions as in figure 6.3).

correlation of the parameterized and simulated detector distance as well as the independence of the scattering intensity from the detector distance validate the PScF approximation on the basis of isotropic scattering.

For the example of water, that is presented here, the parameters are summarized in table 6.1.

6.1.4 Angular Dependence of the Detector Sensitivity

A neutron that is scattered in the sample by the angle θ towards the detector, encounters the pixel size reduced by $\cos\theta$ (cf. figure 6.2). Therefore the expected measured intensity of the scattering component is $I \cdot \cos\theta$. In order to check this experimentally, the scintillator has been exposed to the open beam and rotated by ± 90 degrees. However, the measurement (figure 6.8, diamonds) shows a different behaviour than the expected cosine curve (dashed line). The reason for this is that the scattered neutrons pass the scintillator along a larger path length than the scintillator thickness, as explained in section 6.1.1. Because it is not possible to model this effect in the input file of the MCNPX simulation, it is taken into account by the implementation of the correction algorithm. The correct energy and angle dependent absorption rate is given by Eq. 6.3, but the simulation consideres only the energy dependent term for the unscattered beam

$$A^{\text{det}}(E, \theta = 0) = 1 - \exp\left(-\Sigma_{\text{a}}^{\text{det}}(E) \cdot s^{\text{det}}\right) \quad . \tag{6.12}$$

Analogous to the effective sample attenuation coefficient (Eq. 5.1), the effective

Table 6.1: Examples of PScF parameterization parameters for a ^{6}Li-detector.

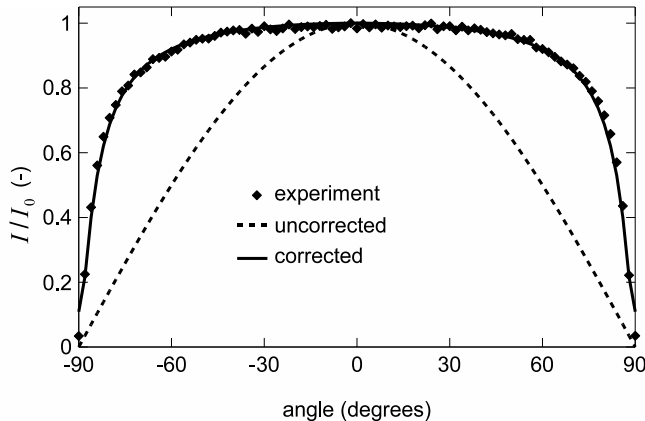| material | facility | PScF parameterization parameters | | | | |
		$S_{\mathrm{P,max}}$	$s_{\mathrm{P,max}}$	c	m_3, m_2, m_1, m_0	a_1, a_0
water	NEUTRA	1.09	0.55	0.48	$-0.008\,09$	0.488
					$0.075\,4$	-0.333
					-0.234	
					0.953	
water	ICON	0.81	0.42	0.80	$-0.025\,0$	0.479
					0.148	-0.336
					-0.300	
					0.956	
water	ANTARES	0.75	0.35	0.40	$-0.007\,56$	0.493
					$0.071\,0$	-0.350
					-0.219	
					0.942	
iron	NEUTRA	0.53	1.15	1.00	$0.000\,319$	0.374
					$0.000\,207$	$0.002\,19$
					$-0.060\,3$	
					0.953	
iron	ANTARES	0.37	0.95	1.00	$-0.000\,306$	0.268
					$0.010\,9$	0.117
					$-0.083\,6$	
					0.933	

Figure 6.8: Measurement of the open beam intensities with the detector plane rotated around ± 90 degrees against the neutron beam (diamonds). The lines show the expected values with a constant angular sensitivity (dashed) and with the correction for the angular dependence of the detector (solid).

attenuation coefficient for the neutron absorption in the detector is defined as

$$\Sigma_{\mathrm{a,eff}}^{\mathrm{det}} = \frac{-1}{s^{\mathrm{det}}} \log \left(\frac{\int \Phi^0(E) \exp\left(-\Sigma_{\mathrm{a}}^{\mathrm{det}}(E) \cdot s^{\mathrm{det}}\right) \mathrm{d}E}{\int \Phi^0(E)\, \mathrm{d}E} \right) \qquad . \tag{6.13}$$

With that the energy independent absorption rate for the unscattered beam becomes

$$A_0^{\mathrm{det}} = 1 - \exp\left(-\Sigma_{\mathrm{a,eff}}^{\mathrm{det}} \cdot s^{\mathrm{det}}\right) \qquad , \tag{6.14}$$

and the energy independent absorption rate for the scattered beam is

$$
\begin{aligned}
A^{\mathrm{det}}(r) &= 1 - \exp\left(-\Sigma_{\mathrm{a,eff}}^{\mathrm{det}} \cdot s^{\mathrm{det}} \cdot \frac{\sqrt{d^2 + r^2}}{d}\right) \\
&= 1 - \left(1 - A_0^{\mathrm{det}}\right)^{\sqrt{d^2+r^2}/d} \qquad .
\end{aligned}
\tag{6.15}
$$

Therefore, in the implementation of the correction algorithm the PScF values (simulated, approximated, or parameterized) are multiplied with the factor for the correction of the scattering angle

$$\frac{A^{\mathrm{det}}(r)}{A_0^{\mathrm{det}}} = \frac{1 - \left(1 - A_0^{\mathrm{det}}\right)^{\sqrt{d^2+r^2}/d}}{A_0^{\mathrm{det}}} \qquad . \tag{6.16}$$

The solid line in figure 6.8 shows the good agreement of this correction with the measured intensities.

The correction of the detector sensitivity for the neutron incidence angle is particularly important for thin detectors with a low absorption rate, where only a small percentage of the neutrons are counted. If anyway almost all neutrons are counted (e.g. by a Gd-detector), the correction factor approximates 1.

6.1.5   Binning

Computing the sample scattering with PScF is an extensive operation. Unlike a usual convolution of point spread functions, the scattering kernal varies for each pixel, since the material definitions and particularly the sample thicknesses and detector distances differ. Therefore it is necessary to calculate the two dimensional PScF array for each pixel of the two dimensional radiograph, i.e. the computing time is proportional to the dimension to the power of 4. This means that for the correction of a radiograph with the resolution of $1024{\times}1024$ pixels, around 10^{12} loops are needed, which is far too much for a today's $3\,$GHz processor.

Fortunately, it is not necessary, to compute the scattering with such a precision. Since the PScF and also the total scattering clouds are always smooth functions, it is possible to reduce the size of the radiographs, calculate the total scattering component and expand it again. Of course, the binning width should not be too rough, so that the features of the radiographed sample are still preserved. Usually, a $8{\times}8$ binning yields good results, since also the overall resolution of a radiograph is not better than two to three pixels. This lets the computing time decrease by the factor $8^4 = 4096$, i.e. only $128^4 = 2.7 \cdot 10^8$ loops are needed. For smaller samples or resolutions often a $4{\times}4$ binning is feasible, so that the computing time for one iteration of the sample scattering correction is in the order of 5 to 20 seconds.

6.1.6   Material Mixtures

It is in the nature of non-destructive testing that the exact material composition of the sample is not known. But often at least the main components are known and particularly in experiments, where a material content should be quantified, the involved materials are usually known. Therefore it is not possible to compute the PScF of the correct material, but the PScF of the main scatterer in a sample is used instead, in order to correct a radiograph for the sample scattering. For example in a sand column with water, the water is the main scatterer. Therefore the radiograph of the wet column is corrected with the PScF of water as well as the radiograph of the dry column. Of course, the scattering contribution by the
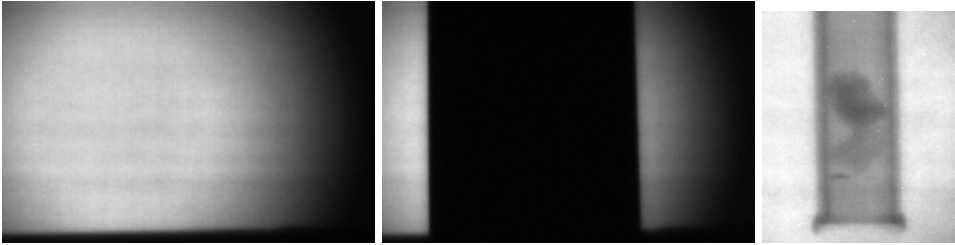
Figure 6.9: Left: Beam limitation with an aperture at the collimator exit (circle) and a Li-plate (bottom). Center: The black body at the place of the sample. Right: Sample radiograph of three soil aggregates in a cylinder, height ~ 1.5 cm.

sand is overestimated by this, but it is overestimated by about the same amount in the correction of the wet as in the dry radiograph. Therefore one can expect that the two errors are compensated by the image referencing, that is required to obtain water distribution without the sand and the quantified water content.

The same procedure as described above for material mixtures, is valid also for multiple layers of different materials. In the previous example of sand and water, the sand is filled in an aluminum container. The front and back side of the container contribute to the total sample scattering, but they are not separable from the sand and water.

6.2 Neutron Scattering by the Experimental Setup

The best correction of the neutron scattering at the surroundings of the sample is to avoid it. This is easily achieved by an additional aperture at the collimator exit. The smaller the aperture is, the less neutrons contribute to the background scattering. If possible, the neutrons should be prevented from hitting the borders of the camera box, because there is a lot of material in beam direction. In the open beam image shown in the left figure 6.9 the beam limitation is clearly visible and hence the neutron beam can not reach the borders of the camera box. Of course, it is not possible to avoid the background scattering completely. But particularly for small samples, it can be reduced from several percents to only a few gray values.

The correction of the remaining background scattering is done in a rather practical way. Its contribution is measured by an additional image recording. For this, the inspected sample is replaced by a *black body*, i.e. a sample that is assumed to be opaque for neutrons. This is a 5 or 10 cm thick block of polyethylene with

$5\,\%$ boron for the experiments at NEUTRA (figure 6.9, center). The simulated
transmission for these blocks is only about $3 \cdot 10^{-5}$ resp. $6 \cdot 10^{-6}$, including the
scattered neutrons. This value is in the order of the detection limit of a 16-bit
detector ($2^{-16} = 1.5 \cdot 10^{-5}$). Ideally, the black body has the same size and shape
as the sample. For practical reasons, it can be larger than the sample, but not
too large, so that some neutrons are able to pass it and to be backscattered to the
detector.

Since the black body blocks more neutrons than the sample in the radiograph,
the measured background scattering behind the black body is scaled by the factor
$f_{\mathrm{bg\ scat}}$

$$f_{\mathrm{bg\ scat}} = \frac{\sum_{x,y} \Phi(x,y)}{\sum_{x,y} \Phi^{\mathrm{bb}}(x,y)} \quad , \tag{6.17}$$

where $\Phi(x,y)$ is the measured flux of the sample radiograph at the pixel (x,y)
and $\Phi_{\mathrm{bb}}(x,y)$ is the measured flux of the black body radiograph. This scaling
factor contains also the correction for temporal beam fluctuations between the
measurement of the sample and the black body. But it is only correct, if the
beam limitations are visible in the radiographs. Otherwise the amount of neutrons,
contributing to the background scattering, is underestimated and the scaling factor
$f_{\mathrm{bg\ scat}}$ becomes too large.

The correction for the background scattering is then obtained by subtracting
the scaled background scattering from the originally measured flux.

$$\Phi^{\mathrm{bg\ scat\ cor}}(x,y) = \Phi(x,y) - f_{\mathrm{bg\ scat}} \cdot \Phi^{\mathrm{bb}}(x,y) \tag{6.18}$$

After this correction only the region, that is actually behind the black body,
contains meaningful values. Anyway, the surrounding image should contain only
the open beam and the beam limitations. Therefore it makes sense, to consider
after the correction only the subimage behind the black body.

Of course, this correction method for the background scattering is only an
approximation. A more accurate method would be to find (measure) a *Point
Backscattered Function* for the background scattering, that depends on the position
and a subsequent deconvolution. But since it is a big effort to measure these Point
Backscattered Functions and they differ for every experiment, this approach is not
feasible in the everyday measurements, although it would be more accurate. But
it turns out that the suggested approximation yields rather accurate results (cf.
section 7.2).

The first example in figure 6.9 shows that an effective beam limitation for small
samples can suppress the background scattering almost completely (i.e. $\lesssim 0.5\,\%$ of
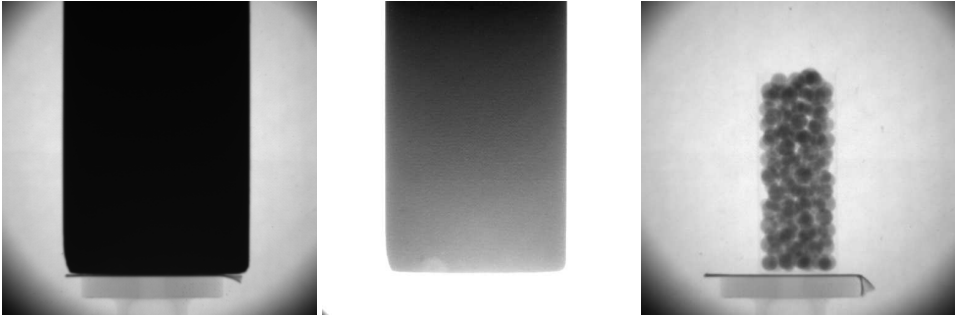
Figure 6.10: Left: Radiograph of the black body for a tomography sample. Center: The same image but with higher contrast settings. It shows the spatial distribution of the background scattering. Right: The sample is a cylinder filled with aluminum oxide balls, height 6 cm.

the open beam value). This is not possible for larger samples (figure 6.10). There is a significant background scattering behind the black body visible. It is stronger at the bottom, where the mirror of the camera box is close to the scintillator. Therefore it is not enough, just to subtract a constant background value.

6.3 Spectral Effects

The Monte-Carlo simulations of the PScF yield not only the scattering distribution, but also the expected intensity of the uncollided beam behind the sample measured with a given detector type. The simulation for several sample thicknesses yields then the flux of the uncollided beam $\Phi(s)$ as a function of the sample thickness s. The effective attenuation coefficient is derived from this by Eq. 2.29

$$\Sigma_{\text{eff}}(s) = \frac{-1}{s} \log \frac{\Phi^{\text{det}}(s)}{\Phi^{\text{ob}}} \quad . \tag{6.19}$$

In the simulations the correction factor f^{ob} for beam fluctuations is not necessary and therefore set equal to 1. The substitution of the transmission

$$T(s) = \frac{\Phi^{\text{det}}(s)}{\Phi^{\text{ob}}} \tag{6.20}$$

yields a reference curve for the relation between the measured transmission T and the effective attenuation coefficient Σ_{eff}.

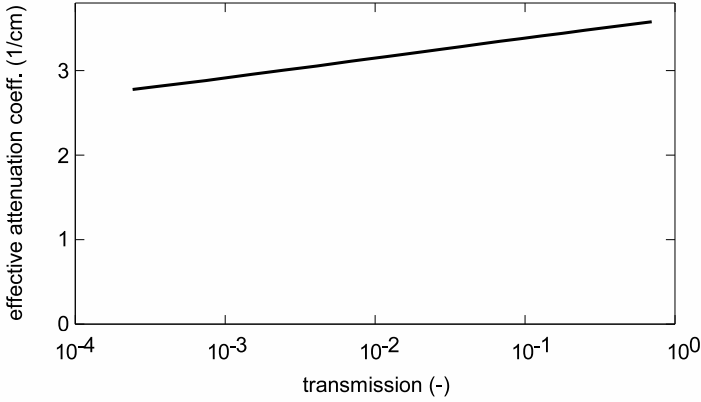$$\Sigma_{\text{eff}}(T) = \frac{-1}{s} \log T \tag{6.21}$$

Figure 6.11: Reference curve for the correction of the spectral effects for water in the NEUTRA spectrum with a Li-scintillator.

Since the simulation contains the neutron source spectrum $\Phi^0(E)$ as well as the energy dependent attenuation coefficients $\Sigma(E)$, the sample thickness s and the energy dependent absorption rate of the detector $A^{\text{det}}(E)$, the reference curve takes into account both the beam hardening and the detector sensitivity (cf. Eq. 5.4).

Figure 6.11 shows a reference curve for water in the NEUTRA spectrum with a Li-scintillator as detector. If the transmission is plotted on a logarithmic scale, the reference curve is in a good approximation a straight line. Therefore it is easy to find the constant value for the effective attenuation coefficient (Eq. 2.30) from the simulation results by a linear regression.

$$\Sigma_{\text{eff}} = \lim_{s \to 0} \Sigma_{\text{eff}}(s) = \lim_{T \to 1} \Sigma_{\text{eff}}(T) \tag{6.22}$$

The correction algorithm finds the transmitted sample thickness from the measured transmission value by exponentially interpolating the simulated thickness-transmission pairs $(s, T(s))$. The corrected transmission value $T^{\text{spect cor}}$ is then computed with the constant effective attenuation coefficient Σ_{eff} as

$$T^{\text{spect cor}} = \exp\left(-\Sigma_{\text{eff}} \cdot s\right) \quad . \tag{6.23}$$

Hence the resulting image obeys the exponential law of attenuation after the correction for the spectral effects.

6.4 Combination of the Correction Algorithms

The previous sections describe the algorithms for the correction of the sample scattering, background scattering and spectral effects. Beside these corrections elaborated in this thesis, there are further well known corrections necessary:

The median filter with a threshold removes white and dark spots due to γ-radiation or pixel failures from the radiographs.

The intensity correction scales the measured radiograph, so that the same neutron source flux is assumed for all radiographs of a series.

The flat-field correction divides the measured flux of a radiograph by the measured open beam flux, yielding the transmission through the sample. Inhomogeneities of the beam and detector are thereby eliminated.

Detector specific corrections may be necessary for the various detector types (e.g. the dark current is a property of CCD cameras and has to be subtracted from the radiographs).

These are in total seven corrections, that have to be applied in order to obtain accurate quantitative results from a measured radiograph. It is decisive to do them in the correct order. The principle is to correct them in the reverse order as they emerge. This gives then the following sequence:

1. The *detector specific effects* emerge only, when the radiographic image is completed. Therefore they are corrected first, in order to obtain the image as it is available at the imaging device (e.g. the CCD chip).

2. The *median filtering* removes the white spots due to the γ-radiation, that are overlaid to the neutron image. The result after this correction corresponds to the image, that the neutrons produce on the scintillator.

3. The background and sample scattering are superposed to the pure transmission image. The *background scattering* is subtracted first, since it can originate also from neutrons, that are scattered in the sample. Therefore it is necessary to have the sample scattering still in the source image of the algorithm for the background scattering correction.

4. The *sample scattering* is subtracted afterwards. The result of the two scattering corrections is a pure transmission image with the attenuation coefficients $\Sigma_{\text{eff}}(s)$, that depend on the sample thicknesses.

5. The *correction of the spectral effects* lets the transmission values obey the exponential law of attenuation with a constant attenuation coefficient ($\Sigma_{\text{eff}}(s) \rightarrow \Sigma_{\text{eff}}$). The resulting values are proportional to the exponentially attenuated, uncollided neutron beam behind the sample.

6. The *intensity correction* affects only properties of the neutron source and norms the incident neutron flux of the open beam. It is a precondition for the quantitative comparison of radiographs within a measurement.

7. The *flat-field correction* finally eliminates the source beam and detector inhomogeneities. The result are transmission values instead of a neutron flux.

Most of the corrections are very fast computations. But particularly the correction of the sample scattering is time consuming (cf. section 6.1.5) and also the median filtering may take some seconds. All together, a radiograph is corrected within 20 to 60 seconds, which is of the order of the usual recording times.

Chapter 7

Error Estimation

The error in the neutron radiographs are twofold: On the one hand there is the *statistical error*, that becomes visible as noise in the transmission images. On the other hand all effects mentioned in chapter 5 contribute to a *systematic error*. Both types of error must be separately considered.

Usually, the aim of the quantitative neutron investigations is not the transmission values, but the material densities or thicknesses of a sample or of a component of the sample. Both, the density ρ and thickness s, are combined in the *mass thickness* τ, that is defined as their product.

$$\tau = \rho \cdot s \tag{7.1}$$

Therefore it is necessary, to consider not only the error of the transmission values, but also the error propagation to the mass thickness. The mass thickness is derived from the measured and corrected transmission values T as

$$\tau = m_\mathrm{a} n \cdot s = \frac{m_\mathrm{a} \Sigma_\mathrm{tot} s}{\sigma_\mathrm{tot}} = -\frac{m_\mathrm{a}}{\sigma_\mathrm{tot}} \log T \quad , \tag{7.2}$$

where m_a is the atomic mass, n the atomic density, σ_tot the total microscopic cross section of the sample material and Σ_tot the corresponding total attenuation coefficient (cf. section 2.1.2). It has the unit of a mass per area, indicating the meaning of the sample mass behind a pixel area of the radiograph.

7.1 Statistical Error

As found in the signal-to-noise (S/N) experiments (section 3.2.2), the statistical error is dominated by the measured neutron statistics. The contribution by a

modern detector system (e.g. a cooled CCD camera) to the noise is negligible. The relative statistical error in an open beam area is then given by the reciprocal signal-to-noise value

$$\frac{\Delta T_{\text{stat}}^{\text{ob}}}{T^{\text{ob}}} = \frac{1}{S/N} \quad . \tag{7.3}$$

Since the expected transmission value for the open beam is $T^{\text{ob}} = 1$, the absolute error equals the relative error in the open beam area.

According to figure 3.9, the S/N ratio is proportional to the square root of the detected neutrons. Therefore the relative error of the attenuated beam behind the sample depends on the transmission value T and is given by

$$\frac{\Delta T_{\text{stat}}}{T} = \frac{1}{\sqrt{T} \cdot S/N} \quad . \tag{7.4}$$

The error propagation to the mass thickness yields then the absolute statistical error

$$\Delta \tau_{\text{stat}} \quad \approx \quad \left| \frac{\mathrm{d}\tau}{\mathrm{d}T} \cdot \Delta T_{\text{stat}} \right| = \frac{m_{\text{a}}}{\sigma_{\text{tot}} T} \cdot \Delta T_{\text{stat}} \tag{7.5}$$

$$= \quad \frac{m_{\text{a}}}{\sigma_{\text{tot}} (S/N)} \cdot \exp\left(\frac{\sigma_{\text{tot}}}{2 m_{\text{a}}} \cdot \tau \right) \quad , \tag{7.6}$$

or the relative statistical error

$$\frac{\Delta \tau_{\text{stat}}}{\tau} = \frac{m_{\text{a}}}{\sigma_{\text{tot}} (S/N)} \cdot \frac{1}{\tau} \cdot \exp\left(\frac{\sigma_{\text{tot}}}{2 m_{\text{a}}} \cdot \tau \right) \quad . \tag{7.7}$$

Therefore the relative error of the evaluated mass thickness becomes large for small and for large values. For small mass thicknesses, the absolute error is limited and is therefore large compared to the actual value ($1/\tau \to \infty$). For large values, the contribution of the noise to the transmission is dominant compared to the expected transmission value ($\exp(\ldots \tau) \to \infty$).

This calculation shows the meaning of a good signal-to-noise ratio, because the statistical error is directly proportional to its reciprocal value. The neutron spectrum and detector sensitivity play a role, because they affect the effective total cross section σ_{tot}. Figure 7.1 shows a comparison of the expected statistical error for a measurement of water in the NEUTRA and ICON spectrum. While the colder ICON spectrum is more sensitive for thin water layers, the NEUTRA spectrum is able to transmit thicker layers.

The corrections for the sample and background scattering subtract a smooth scattering cloud from the transmission images. By this operation the transmission T decreases, while the absolute statistical error ΔT_{stat} is conserved. Therefore the
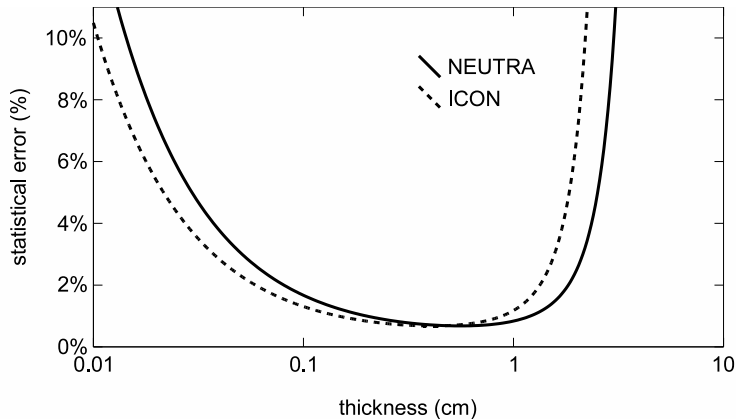
Figure 7.1: Comparison of the expected relative statistical error for a radiograph of a water layer as a function of the sample thickness s (Eq. 7.7). A ^{6}Li-scintillator with the signal-to-noise ratio 200 is assumed as detector for both graphs.

relative statistical error of the transmission $\Delta T_{\text{stat}}/T$ and also the sample thickness $\Delta \tau_{\text{stat}}/\tau$ is increased by the correction algorithm.

Several correction algorithms need additional radiographs to the sample radiograph. For the correction of the background scattering, a radiograph of a black body is needed and an open beam radiograph for the flat field correction. In order to avoid the increase of noise by these corrections, it is recommended to record several of these additional radiographs, to adjust their intensities and to use the pixelwise mean value for the further evaluations. The same is valid also for the CCD dark current.

7.2 Background Scattering

As described in section 6.2 the background scattering is measured by one radiograph of a black body Φ^{bb}. This measured flux of the background is used for the correction of the measured flux behind the sample Φ^{sample} and the measured open beam flux Φ^{ob}. The deviations of the scaled measured background scattering fluxes from the correct background scattering contributions are denoted as $\Delta\Phi^{\text{sample}}$ and $\Delta\Phi^{\text{ob}}$, respectively.

$$\Delta\Phi^{\text{sample}} = \left| f^{\text{sample}}_{\text{bg scat}} \cdot \Phi^{\text{bb}} - \Phi^{\text{sample}}_{\text{bg scat}} \right| \tag{7.8}$$

$$\Delta\Phi^{\text{ob}} = \left| f^{\text{ob}}_{\text{bg scat}} \cdot \Phi^{\text{bb}} - \Phi^{\text{ob}}_{\text{bg scat}} \right| \tag{7.9}$$

The relative error of the transmission, that is computed as $T = \Phi^{\text{sample}}/\Phi^{\text{ob}}$, is then approximately given by the sum of the relative errors of the sample and open beam fluxes

$$\frac{\Delta T_{\text{bg scat}}}{T} \approx \frac{\Delta\Phi^{\text{ob}}}{\Phi^{\text{ob}}} + \frac{\Delta\Phi^{\text{sample}}}{\Phi^{\text{sample}}} = \frac{1}{\Phi^{\text{ob}}} \cdot \left(\Delta\Phi^{\text{ob}} + \frac{\Delta\Phi^{\text{sample}}}{T}\right) \quad . \qquad (7.10)$$

Hence, the relative error of the transmission consists of a constant contribution due to the scattering in the open beam radiograph, and a contribution due to the scattering in the sample radiograph, that increases for smaller transmission values.

The error of the mass thickness is analogous to Eq. 7.5 given by

$$\begin{aligned}
\Delta\tau_{\text{bg scat}} &\approx \left|\frac{d\tau}{dT} \cdot \Delta T_{\text{bg scat}}\right| = \frac{m_a}{\sigma_{\text{tot}}\Phi^{\text{ob}}} \cdot \left(\Delta\Phi^{\text{ob}} + \frac{\Delta\Phi^{\text{sample}}}{T}\right) \\
&= \frac{m_a}{\sigma_{\text{tot}}\Phi^{\text{ob}}} \cdot \left(\Delta\Phi^{\text{ob}} + \Delta\Phi^{\text{sample}}\exp\left(\frac{\sigma_{\text{tot}}}{m_a}\cdot\tau\right)\right) \qquad (7.11)
\end{aligned}$$

or

$$\frac{\Delta\tau_{\text{bg scat}}}{\tau} \approx \frac{m_a}{\sigma_{\text{tot}}\Phi^{\text{ob}}} \cdot \frac{1}{\tau} \cdot \left(\Delta\Phi^{\text{ob}} + \Delta\Phi^{\text{sample}}\exp\left(\frac{\sigma_{\text{tot}}}{m_a}\cdot\tau\right)\right) \quad . \qquad (7.12)$$

For small and large mass thicknesses, the expected error of the quantitative evaluation increases because of inaccuracies in the correction of the background scattering in the open beam radiograph or the sample radiograph, respectively.

Figure 7.2 shows an example of the relative error for water in the NEUTRA and ICON spectrum. Again the ICON spectrum is more suitable for the quantification of small mass thicknesses because of the larger effective cross section σ_{tot}, and the NEUTRA spectrum is better for larger mass thicknesses. But it is remarkable that the assumed errors for the background scatterings $\Delta\Phi^{\text{ob}} = \Delta\Phi^{\text{sample}} = 0.01 \cdot \Phi^{\text{ob}}$ are propagated to about 4 %. Therefore the results of the quantification are very sensitive to the parameters of the background scattering correction.

7.3   Sample Scattering

The effect of inaccuracies in the correction of the sample scattering is computed analogously to the background scattering. But since the open beam radiograph contains no sample and therefore no sample scattering, the terms with $\Delta\Phi^{\text{ob}}$ are omitted. The relative errors of the transmission and mass thickness are then according to Eq. 7.10 and 7.12

$$\frac{\Delta T_{\text{s scat}}}{T} \approx \frac{1}{T} \cdot \frac{\Delta\Phi^{\text{sample}}}{\Phi^{\text{ob}}} \qquad (7.13)$$

$$\frac{\Delta\tau_{\text{s scat}}}{\tau} \approx \frac{m_a}{\sigma_{\text{tot}}\tau} \cdot \frac{\Delta\Phi^{\text{sample}}}{\Phi^{\text{ob}}} \cdot \exp\left(\frac{\sigma_{\text{tot}}}{m_a}\cdot\tau\right) \quad . \qquad (7.14)$$
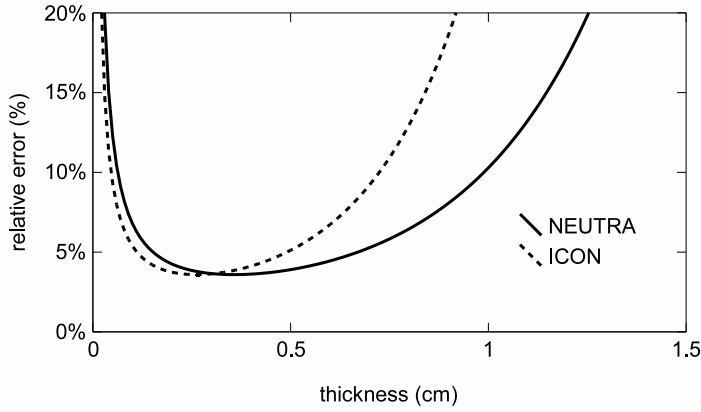
Figure 7.2: Comparison of the expected relative errors due to inaccuracies in the correction of the background scattering. The graphs are calculated for the radiograph of a water layer as a function of the sample thickness s with a ^{6}Li-scintillator (Eq. 7.12). The assumed errors of the measured background scatterings are $\Delta\Phi^{\mathrm{ob}} = \Delta\Phi^{\mathrm{sample}} = 0.01 \cdot \Phi^{\mathrm{ob}}$.

Again the relative error in the mass thickness becomes large for small and large evaluated values. An example of the error propagation to the evaluated thickness is shown in figure 7.3. It is based on the same assumptions as the example for the background scattering.

7.4 Spectral Effects

The effects of the polyenergetic neutron beam and the energy dependent cross sections are combined in the effective attenuation coefficient Σ_{eff} (Eq. 5.2) or the corresponding effective microscopic cross section σ_{eff}, respectively. It is used to derive the mass thickness τ from the transmission values T by Eq. 7.2

$$\tau = -\frac{m_{\mathrm{a}}}{\sigma_{\mathrm{tot}}} \log T \quad . \tag{7.15}$$

Therefore the relative error of the evaluated mass thickness is the same as the uncertainty of the effective cross section.

$$\frac{\Delta\tau}{\tau} \approx \frac{\Delta\sigma_{\mathrm{tot}}}{\sigma_{\mathrm{tot}}} \tag{7.16}$$
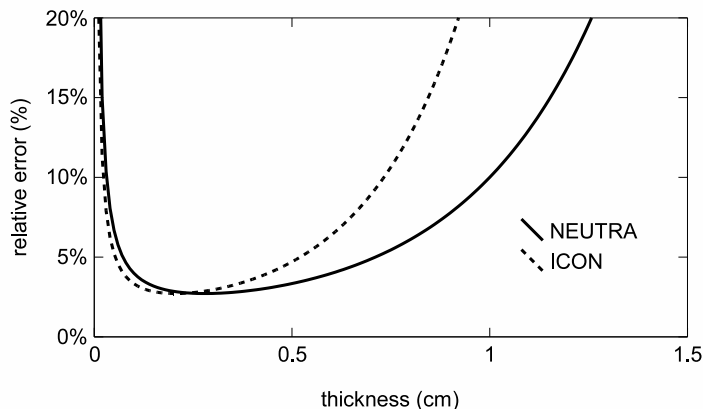
Figure 7.3: Comparison of the expected relative errors due to inaccuracies in the correction of the sample scattering. The graphs are calculated for the radiograph of a water layer as a function of the sample thickness s with a ^{6}Li-scintillator (Eq. 7.14). The assumed error of the calculated sample scattering is $\Delta\Phi^{\text{sample}} = 0.01 \cdot \Phi^{\text{ob}}$.

7.5 Systematic Error

The inaccuracies of the three correction methods for the sample scattering, background scattering and spectral effects contribute to the systematic error. Unlike the statistical error, it is not possible to predict the expected systematic error prior to an experiment. While the statistical error depends mainly on the signal-to-noise ratio, which is a measurable detector property, the systematic errors depend particularly on the experimental setup. For example the background scattering depends strongly on the beam limitation, the sample scattering on the shape of the sample and the beam hardening on the material composition of the sample. Therefore it is not possible to give numbers for the inaccuracies of the calculated background scattering $\Phi^{\text{sample}}_{\text{bg scat}}$, $\Phi^{\text{ob}}_{\text{bg scat}}$, the sample scattering $\Phi^{\text{sample}}_{\text{s scat}}$ or the effective cross sections σ_{eff}, Σ_{eff}.

In summary, the total systematic error can be indicated sometimes after the evaluation of the experiment. One method is the comparison of the total sample mass calculated by the neutron radiography with the mass measured by a balance (cf. section 8.2.1). But for this it is necessary, to know the material composition of the sample exactly. Another possibility is, to measure a well known reference material, that has approximately the same properties as the inspected sample and to compare the results for the reference material (cf. section 8.2.3). Of course,

these comparisons yield only one number instead of an error for every pixel value. But since the scattering clouds are always smoothly distributed over the whole radiograph, these two methods yield rather reliable numbers for a systematic error that is valid for the whole radiograph.

The other way round, finding the systematic error by such a comparison can be used to adjust the calculated scattering components by a factor, in order to obtain even more accurate results. This is of course an impure approach, to adjust the correction algorithm, in order to obtain the known result. But it is justified, since the shapes of the scattering contributions are not dramatically wrong because of small inaccuracies in the assumed experimental setup.

Chapter 8

Results

Many experiments have been performed during the elaboration of this thesis. The intention of some experiments is to develop and test the correction methods. Other experiments are relevant measurements of scientists, who are interested in the quantitative results by neutron radiography and tomography. These experiments are evaluated according to the development status of the correction algorithms at that time. Some of them are presented here as typical results. Because it is planned to use the correction algorithm also at other facilities than NEUTRA, some measurements and corrections of radiographs and tomograms obtained in Munich, Berlin and Pretoria are mentioned here.

8.1 Methodic Experiments

Most often the methodic experiments are done for the development and testing of the correction methods. But it is also necessary to know the properties of the experimental setup (e.g. spectrum, detector) and the sample materials. Some of these measurements are described here.

8.1.1 Detector Characterization

The sections 2.1.3 and 5.3 show the importance of the knowledge of the detector properties. Although a detector can be a complex system, only the energy and angularly dependent absorption rate $A^{\mathrm{det}}(E, \theta)$ of the neutron absorbing material is relevant for the correction algorithm (Eq. 6.2). In order to compute it, the attenuation coefficient $\Sigma_{\mathrm{a}}^{\mathrm{det}}(E)$ and the detector thickness s^{det} are needed, or alternatively

the microscopic absorption cross section $\sigma_{\mathrm{a}}^{\mathrm{det}}(E)$ of the detector material and its mass thickness τ^{det}.

$$\Sigma_{\mathrm{a}}^{\mathrm{det}}(E) \cdot s^{\mathrm{det}} = \frac{\sigma_{\mathrm{a}}^{\mathrm{det}}(E) \cdot \tau^{\mathrm{det}}}{m_{\mathrm{a}}^{\mathrm{det}}} \tag{8.1}$$

The atomic mass $m_{\mathrm{a}}^{\mathrm{det}}$ of the detector material and the microscopic absorption cross sections as a function of the energy are tabulated values. Therefore only the mass thickness of the detector material has to be determined. If there is no information about it from the manufacturer, it is possible to measure it. For thin detectors, it is obtained with a measurement of the transmission of the detector. (For thick detectors, this is not easy, because almost all neutrons are absorbed and the errors become large. But anyway, the absorption rate of a thick detector equals one in a good approximation.)

The experiment has a very simple setup: the detector is put into the neutron beam and the transmission signal measured with a second detector. This second detector is preferably a thick detector, so that its own properties and the neutron spectrum play only a minor role. The measured flux behind the detector is then

$$\Phi^{\mathrm{det}} = \int \Phi^0(E) \cdot \exp\left(-\frac{\sigma(E) \cdot \tau}{m_{\mathrm{a}}}\right) \mathrm{d}E \quad , \tag{8.2}$$

where $\Phi^0(E)$ is the neutron source flux. The open beam flux has to be measured as a reference value

$$\Phi^{\mathrm{ob}} = \int \Phi^0(E) \, \mathrm{d}E \quad . \tag{8.3}$$

Usually, the neutron detection material (e.g. ^{6}Li) is far more absorbing than the other materials in the detector (e.g. F, ZnS, binder). Therefore the total attenuation by the detector is primarily due to the absorption of the neutron detection material. So it is a good approximation to replace the overall cross section $\sigma(E) \approx \sigma_{\mathrm{a}}^{\mathrm{det}}(E)$, the overall atomic mass $m_{\mathrm{a}} \approx m_{\mathrm{a}}^{\mathrm{det}}$ and the overall mass thickness $\tau \approx \tau^{\mathrm{det}}$ in Eq. 8.2.

$$\Phi^{\mathrm{det}} \approx \int \Phi^0(E) \cdot \exp\left(-\frac{\sigma_{\mathrm{a}}^{\mathrm{det}}(E) \cdot \tau^{\mathrm{det}}}{m_{\mathrm{a}}^{\mathrm{det}}}\right) \mathrm{d}E \tag{8.4}$$

In a first step the beam hardening is neglected and the energy dependent cross

Table 8.1: Results of the detector characterization for the ^{6}Li-scintillator NDg 40 from Applied Scintillation Technologies.

measured transmission	$\Phi^{\text{det}}/\Phi^{\text{ob}} = 0.820$
averaged cross section	$\overline{\sigma_{\text{a}}^{\text{det}}} = 785\,\text{barn}$
effective cross section	$\sigma_{\text{a,eff}}^{\text{det}} = 766\,\text{barn}$
mass thickness	$\tau^{\text{det}} = 25.8\,\text{g/m}^2$

section replaced by a cross section, that is averaged over the neutron spectrum

$$\sigma_{\text{a}}^{\text{det}}(E) \to \overline{\sigma_{\text{a}}^{\text{det}}} \quad = \quad \frac{\int \Phi^0(E) \cdot \sigma_{\text{a}}^{\text{det}}(E)\,\text{d}E}{\int \Phi^0(E)\,\text{d}E} \quad , \tag{8.5}$$

$$\Phi^{\text{det}} \quad \approx \quad \int \Phi^0(E) \cdot \exp\left(-\frac{\overline{\sigma_{\text{a}}^{\text{det}}} \cdot \tau^{\text{det}}}{m_{\text{a}}^{\text{det}}}\right)\,\text{d}E \tag{8.6}$$

$$= \quad \int \Phi^0(E)\,\text{d}E \cdot \exp\left(-\frac{\overline{\sigma_{\text{a}}^{\text{det}}} \cdot \tau^{\text{det}}}{m_{\text{a}}^{\text{det}}}\right) \tag{8.7}$$

$$= \quad \Phi^{\text{ob}} \cdot \exp\left(-\frac{\overline{\sigma_{\text{a}}^{\text{det}}} \cdot \tau^{\text{det}}}{m_{\text{a}}^{\text{det}}}\right) \quad . \tag{8.8}$$

With this simplification, the mass thickness is calculated from the detector radiograph and the open beam radiograph as

$$\tau^{\text{det}} \approx \frac{-m_{\text{a}}^{\text{det}}}{\overline{\sigma_{\text{a}}^{\text{det}}}} \cdot \log \frac{\Phi^{\text{det}}}{\Phi^{\text{ob}}} \quad . \tag{8.9}$$

This is a first estimation of the detector mass thickness. It is now possible to replace the averaged cross section $\overline{\sigma_{\text{a}}^{\text{det}}}$ by a first estimation of the effective cross section $\sigma_{\text{a,eff}}^{\text{det}}$, that includes also the beam hardening (Eq. 5.1), and to find a better approximation for the mass thickness (Eq. 8.9). After two or three iterations of this procedure, the value for the mass thickness converges within a reasonable numerical accuracy, i.e. the expected experimental errors will be much larger.

The experiment has been performed at NEUTRA for the LiF/ZnS-scintillator NDg 40 from Applied Scintillation Technologies, that has been used as a standard detector at that time. The scintillator thickness is known ($200\,\mu$m), but unfortunately the manufacturer provided no specification about the ^{6}Li content. Therefore the mass thickness is measured as described above and the values in table 8.1 are found. The final result for the mass thickness (including the beam hardening effect of 2.5 % for the effective cross section) is $\tau^{\text{det}} = 25.8\,\text{g/m}^2$. The corresponding energy dependent absorption rate of the detector is depicted in figure 8.1.
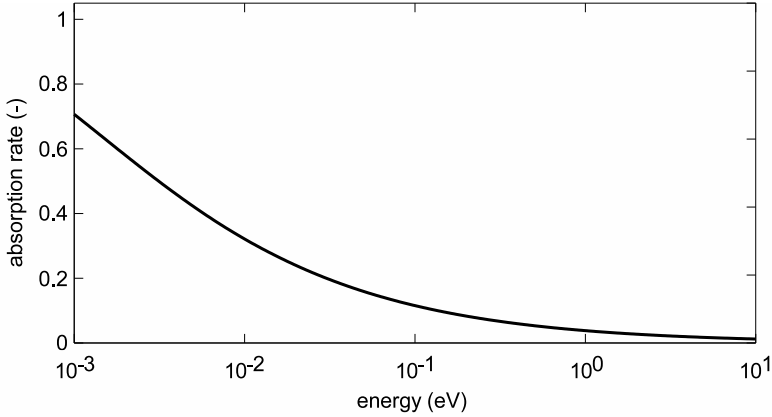
Figure 8.1: Energy dependent absorption rate $A^{\mathrm{det}}(E)$ for the ^{6}Li-scintillator NDg 40.

8.1.2   Test Samples

Many well known test samples have been radiographed during the elaboration of the presented correction algorithm in order to test it. A typical sample is a step wedge, because several different sample thicknesses are measured at once. The step wedge presented in this section is made of iron and has 10 steps, each 1 cm high. The thicknesses of the steps in beam direction are 0.5, 1.0, 1.5, . . . , 5 cm (cf. figure 8.2).

It is radiographed at the NEUTRA facility with a Li-scintillator. The evaluation is done once with all corrections mentioned in chapter 6, and once without the correction for the background scattering, sample scattering and beam hardening. The corresponding transmission images are shown in figure 8.3(a) with identical brightness and contrast settings. Even the visual impression makes clear that the uncorrected image is much brighter due to the scattered neutrons. In the corrected image, the scattered neutrons are subtracted and the boundaries of the ten steps become visible again.

The vertical profiles of the thicknesses calculated from the transmission images are depicted in figure 8.3(b). While the evaluated thicknesses of the uncorrected steps do not show a clear distinction between the thicker steps, the boundaries become distinguishable again after the correction. This is amazing, since the subtracted scattering clouds are only smooth curves. But because the neutron transmission is attenuated exponentially and only 1 % or even less of the neutrons is transmitted through the thicker steps, only small differences do have a large effect.
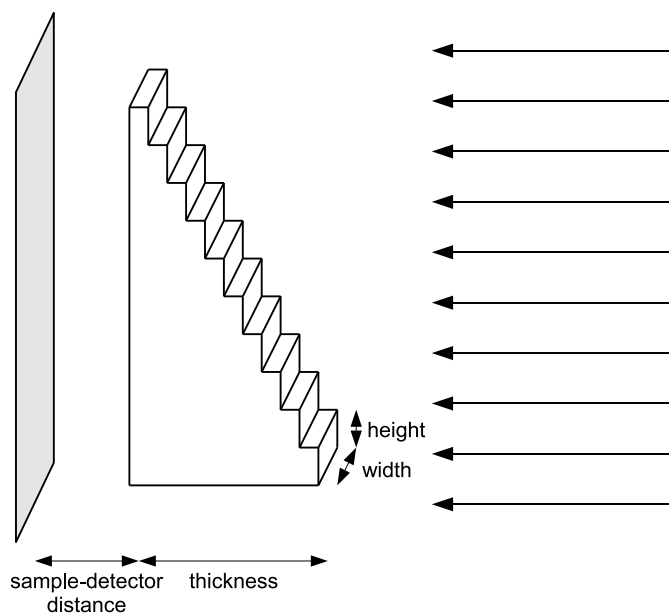
Figure 8.2: Experimental setup for the measurement of the iron step wedge. The sample-detector distance is constant for all steps. The width and height of each step is $2 \times 1 \, \text{cm}^2$ and the thicknesses in beam direction are 0.5, 1.0, ..., 5.0 cm.
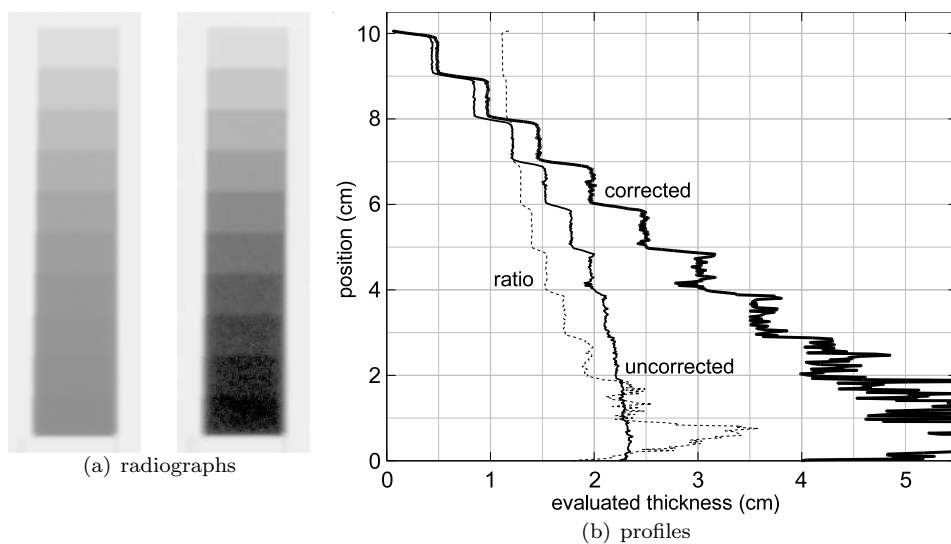
(a) radiographs

(b) profiles

Figure 8.3: (a) Transmission images of an iron step wedge radiographed at NEU-TRA, before (left) and after (right) the corrections for the background and sample scattering and the spectral effects. The step wedge is 10 cm high and the thicknesses are 0.5, 1.0, 1.5, ..., 5.0 cm. (b) Vertical profiles through the evaluated thickness of the iron step wedge. The line of the evaluation after correction (thick) should follow the diagram grid. The dotted line shows the ratio between the corrected and the uncorrected evaluated thickness (no units).

Unfortunately, this is valid also for the statistical error. The corrected transmission values show more noise than the uncorrected, particularly at the very thick steps (3.5 to 5 cm). The limitation of the quantitative evaluation for thick samples as explained in section 7.1 becomes clearly visible at this example.

But for the thinner steps, the quantification works well. The results for the thicknesses 0.5 to 3 cm are correct within $\pm 5\%$. Since the effective attenuation coefficient is calculated as $\Sigma_{\mathrm{eff}} = 1.18\,\mathrm{cm}^{-1}$, this corresponds to 0.59 to 3.55 free path lengths or theoretical transmission values of 55 to 2.9%. In order to stay within the deviation of $\pm 5\%$, the scattering cloud has to be calculated with a maximum error of 0.47%.

The effect of the corrections is depicted with the dashed line. It shows the ratio of the corrected and uncorrected evaluated thicknesses (smoothed). For the thinnest step (0.5 cm), the effect of the correction is only about 10%, but for 3.5 cm it is already around 70%.

For other materials, the results of the correction algorithm are comparable [19]. In this example, the sample-detector distance is chosen 6 cm, which is a realistic value for a radiograph and where the sample scattering is still important. For very small distances (0 to 2 cm) the sample scattering is slightly overestimated. But since it behaves approximately like $1/r^2$, this has a large effect to the evaluated thickness.

Another limitation is given by the neutron energy spectrum. For cold neutrons the Bragg edges become dominant in the scattering cross sections of some materials. But until now they are not taken into account by the MCNPX libraries (cf. section 8.3.2).

8.1.3   Use of Heavy Water vs. Light Water

Many of the soil physical experiments are designed to measure the water content in natural or artificial structures quantitatively and in three dimensions. For these tomograms it is necessary to record a set of projections through the sample along all directions, and all transmission values should be within an appropriate range for the quantification. Therefore the diameter of the tomographic slices is restricted by the neutron attenuation of the sample material (cf. chapter 7). On the other hand a minimum size of the sample is needed in order to obtain representative results. For a thermal neutron beam, the attenuation coefficient of water is about $3.5\,\mathrm{cm}^{-1}$. Together with the soil structure and a typical porosity of 40 to 50%, the maximum sample thickness is about 2 cm, which is often not enough for represen-
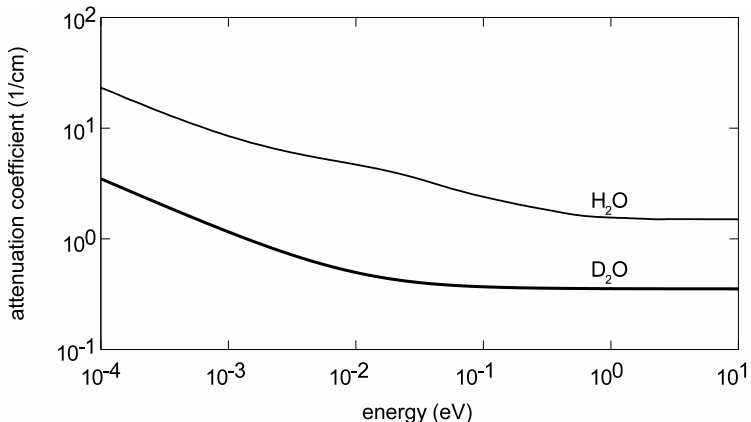
Figure 8.4: Attenuation coefficient of D_2O compared to H_2O in the cold and thermal neutron energy region.

Table 8.2: Properties of D_2O compared to H_2O at normal pressure [20].

property	D_2O	H_2O	
dynamic viscosity at $25\,°C$	1.101	0.893	$mPa \cdot s$
surface tension at $25\,°C$	71.93	71.97	mN/m
melting temperature	3.813	0	$°C$
boiling temperature	101.4	100	$°C$
maximum density at	11.23	3.98	$°C$
density at $25\,°C$	1.106	1	g/cm^3

tative structures. Because the neutron attenuation of heavy water (D_2O) is about seven times less than for light water ($\Sigma_{D_2O} \sim 0.5\,cm^{-1}$, figure 8.4), it is a good alternative to use heavy water as a fluid for the experiments.

Of course, D_2O has not the same physical properties as H_2O. K. Rohde has collocated these properties and has performed measurements for the experimental verification during a practical work. The most important properties of D_2O for soil physical studies are summarized in the tables 8.2 and 8.3. The main differences compared to H_2O are the higher viscosity and the higher density. These values allow to transfer the results obtained with D_2O to H_2O. Attention should be paid to the dependence of the viscosity on the temperature, because this effect can exceed the other differences between light and heavy water.

Table 8.3: Viscosity [21], surface tension [22] and density [21] of H_2O and D_2O at different temperatures.

temperature	dynamic viscosity		surface tension		density	
[°C]	[mPa · s]		[mN/m]		[g/cm^3]	
	D_2O	H_2O	D_2O	H_2O	D_2O	H_2O
5	1.987	1.528	74.8	75.0	1.10543	0.99974
10	1.677	1.311	74.1	74.3	1.10519	0.99971
25	1.098	0.892	71.9	72.0	1.10230	0.99706

8.2 Applications

A very typical application for neutron radiography is the detection of water in porous media. Most of the relevant applications have been provided by the soil physics group at the ETH Zurich, with either real or semi-artificial soil or sand as a structure material. The topic of the investigations is the quantification of the water content distribution with a high spatial resolution. In some investigations the imbibition or drying process has been observed in two dimensions as a time series of radiographs, while others consist of three-dimensional recordings of stationary conditions. In two cases the inflow and outflow of water in a sand column has been recorded even in three dimensions and time resolved, at the cost of spatial resolution.

8.2.1 Water Content in a Natural Soil

Massimo Guglielmetti works on a PhD thesis, where the top soil water content is measured by microwave radiometry. The final goal is, to have a method to measure the water content of the soil on a large area from a satellite. In order to gauge the microwave measurements, three soil sections have been investigated with neutron radiography. The advantage compared to the time domain reflectivity (TDR) is the high spatial resolution. Nevertheless, this method is applied too, in order to have a validation for the results.

The soil sections ($15 \times 15 \times 1.6\,\mathrm{cm}^3$) have been taken in the field and brought by car to the NEUTRA facility. In order to prevent evaporation and water redistribution during the transport, the samples are wrapped into a foil and cooled. Additionally, some small balls of boron glass are put into the soil as markers to detect shifts of the soil structure during the experiments.

The three samples have been radiographed in the original wet state and after

Table 8.4: Comparison of the measured masses of evaporated water by radiography (without and with corrections) and by balance.

sample in figure 8.5	evaporated water mass (g)		by balance
	by radiography		
	without correction	with correction	
top	54.0	87.1	102.2
middle	53.9	89.9	102.4
bottom	55.6	93.0	111.5

drying them in an oven, until their mass has decreased to a constant value (~ 1 day). The radiographs are evaluated for the two-dimensional water content distribution without and with corrections, but not for the background scattering, since this method has not yet been elaborated at that time.

The corrected transmission images of the wet soils are shown in figure 8.5 (left). The structure is inhomogeneous and different for all three soil sections. The second column shows the evaluated water content after referencing the transmission images of the wet state with the dry state. The dark spots depict regions in the soil sections with only little water (e.g. stones), while the bright areas have a high water content. The horizontal averages of the water content are drawn as vertical profiles in the right column. Also these diagrams show large variations due to the inhomogeneous soil structures, and all graphs differ from each other. This makes clear that the size of the sections is too small, to obtain a representative vertical profile of the water content.

The evaluations with the corrections for the sample scattering and beam hardening lead to definitely higher water contents than without the corrections (cf. table 8.4). But there is still a significant difference of about 15 % to the correct value measured by balance. This shows the importance of the background scattering, that has not been measured in this experiment.

8.2.2   Water Flow between Soil Aggregates

Biologically active soils are often aggregated. The same applies for soil exposed to frost or frequent swelling and shrinking. The single aggregates have a size between less than a millimeter to centimeters. In order to understand the water storage and flow in such soils, it is necessary to understand the flow between single aggregates. This is the topic of an experiment of A. Carminati (soil physics, ETH Zurich).
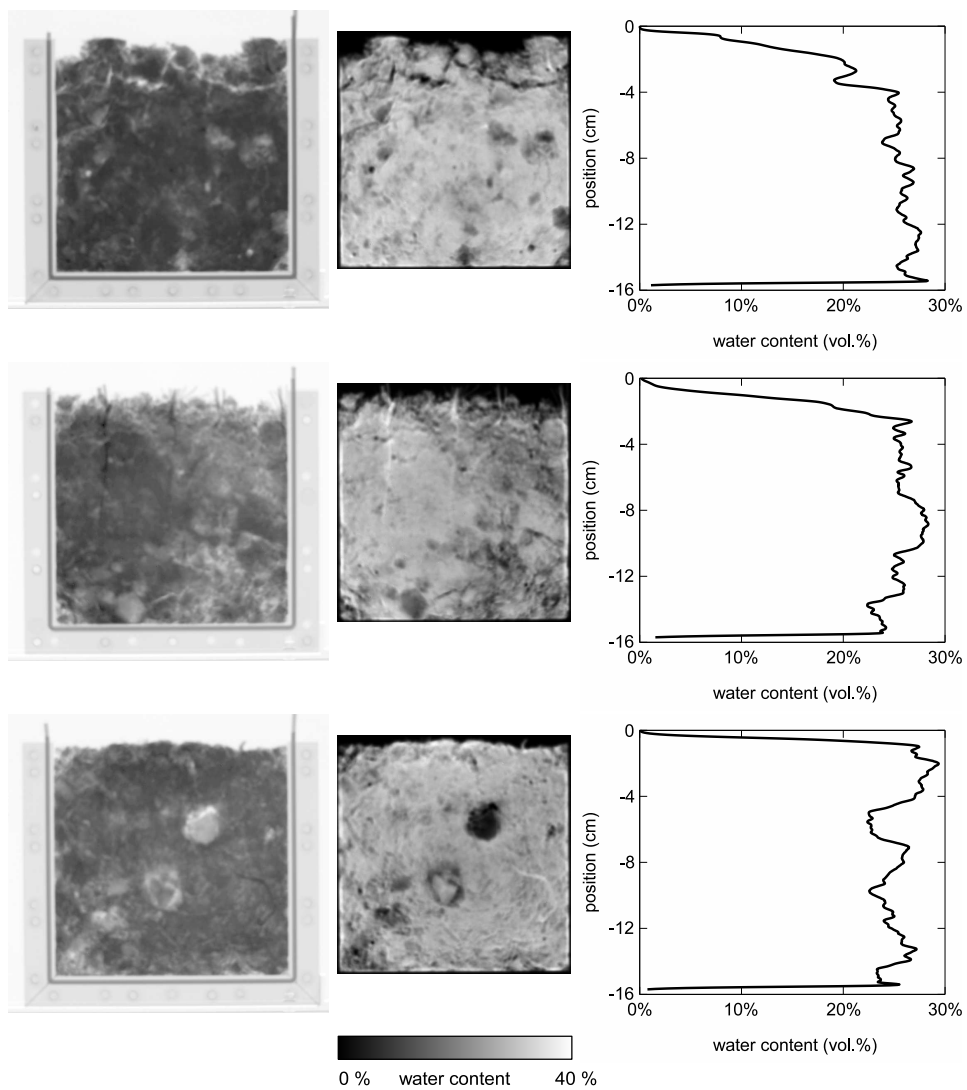
Figure 8.5: Left: corrected transmission images of the three soil sections in the wet state. Center: two-dimensional distribution of the water content (white means high water content). Right: Vertical profile of the water content (horizontally averaged).

Three natural, air dry soil aggregates with a diameter of 4 to 6 mm are placed on top of each other. The water flow after wetting the top aggregate has been measured with a series of neutron radiographs for several replicated experiments. In addition, the aggregates are inspected at the SLS (PSI) [23] by synchrotron X-ray tomography, that reveals the structure of the micropores and also the water distribution at equilibrium. Particularly the contact surfaces between the aggregates are a matter of interest.

Because the attenuation coefficients for synchroton radiation are different compared to the neutron beam, a special choice for the container material is made. While aluminum is a very convenient material for neutron radiography, it strongly attenuates the synchrotron radiation. On the other hand plexiglas is a good choice for synchrotron radiation, but a strong neutron scatterer because of the high hydrogen content. Therefore carbonate and polycarbonate are finally used as container materials. Both synchrotron radiation and neutrons are able to penetrate them easily. Although the polycarbonate contains some hydrogen and attenuates the neutron beam more than the carbonate, it is easier to work on. One goal of the synchrotron tomography is, to visualize the water distrubition in the micropores of the aggregates. But since water is nearly invisible for X-rays, CaI_2 has been solved in the water (4 %) to increase the contrast.

The neutron experiments are performed at the NEUTRA facility. Since the samples are very small ($\sim 0.5 \times 1.5 \, cm^2$) and in order to obtain a good signal-to-noise ratio even for the short recording times of the time series, the experiments have been performed near to the beam exit with a higher flux. The higher flux is at the cost of a smaller collimation ratio. To obtain the best possible image resolution of the small aggregates in spite of that, the sample is placed close to the detector (2.5 cm), what causes in turn a lot of sample scattering on the detector. This disturbation is computationally corrected after the experiments by the described PScF method, in order to obtain the water content of the aggregates.

The background scattering has been avoided very well by an appropriate experimental setup. Due to the small sample size, the beam is limited to about 3 cm diameter. The measured background scattering behind a black body is reduced by that to only a few gray values or $\lesssim 0.5 \%$ of the open beam value.

All radiographs are completely corrected according to chapter 6 and referenced to the dry state. The resulting time series show the water distribution (without soil) during the imbibition process with a pixel size of 45 μm. The mass of the water, that is applied to the aggregates, is not measured in this experiment. Therefore it
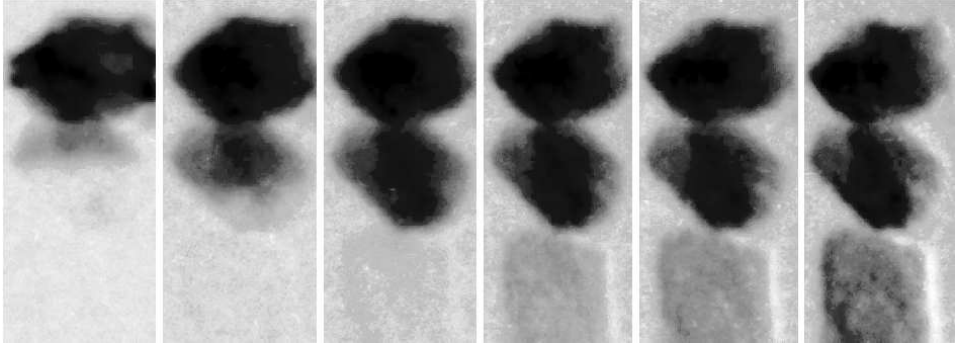
Figure 8.6: Time series of the referenced transmission images of the three soil aggregates. The images are recorded 0 min, 1 min, 10 min, 2 h, 4 h and 8 h after wetting the top aggregate.

is not possible to indicate the accuracy of the quantitative evaluation. But since the background scattering is mostly avoided and the neutron transmission through the small samples is in a good range for the quantification, the accuracy is expected to be within $\pm 5\,\%$.

Figure 8.6 shows the water distributions in the three aggregates at six time steps. It is remarkable that the water flows within a few minutes from the first to the second aggregate, while even after 8 hours the third aggregate is not in a hydraulic equilibrium with the others. Carminati relates this to the effective area of the contact between the wet and the dry aggregates, respectively. As visible in the high resolution ($3.5\,\mu$m) synchrotron tomograms (figure 8.7), the water can flow through a much larger area, if the hydraulic potential is large enough to fill the space between the aggregates with water [24].

8.2.3   Out- and Inflow into Structured Sand Columns

One of the most challenging experiments during the experimental period for this thesis, is an out- and inflow experiment into structured sand columns, that is investigated with neutron radiography and tomography. It has been performed together with I. Neuweiler, M. Vasin (University of Stuttgart) and P. Lehmann (ETH Zurich). Two large columns ($10 \times 10 \times 20\,\text{cm}^3$) are filled with 2000 small cubes of fine (FS, 100 to 500 μm) and very fine sand (VFS, 80 to 200 μm), each $1 \times 1 \times 1\,\text{cm}^3$ [25]. One column consists of a *random* distribution of the small sand cubes, i.e. 32 % of the cubes are filled with fine sand and form an irregular pattern, that is partly connected from the bottom to the top of the column. The
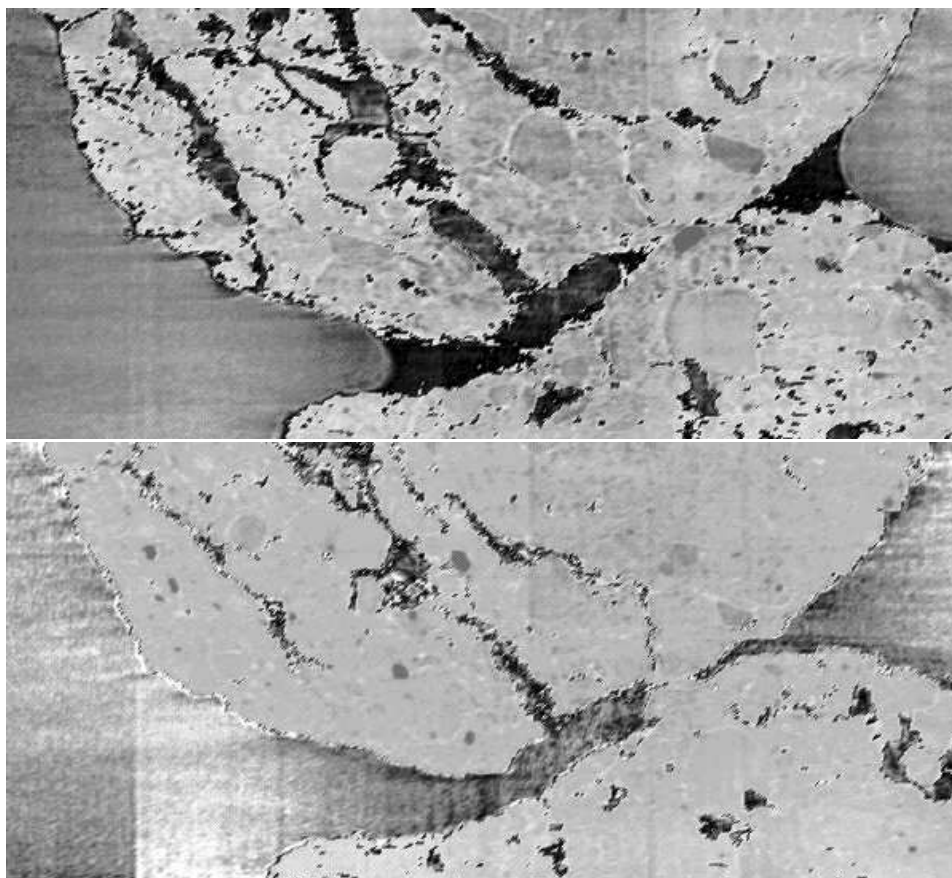
Figure 8.7: Slices through the contact region of two aggregates recorded by synchrotron radiation. The images show qualitatively the soil structure with the micropores and the water (dark).
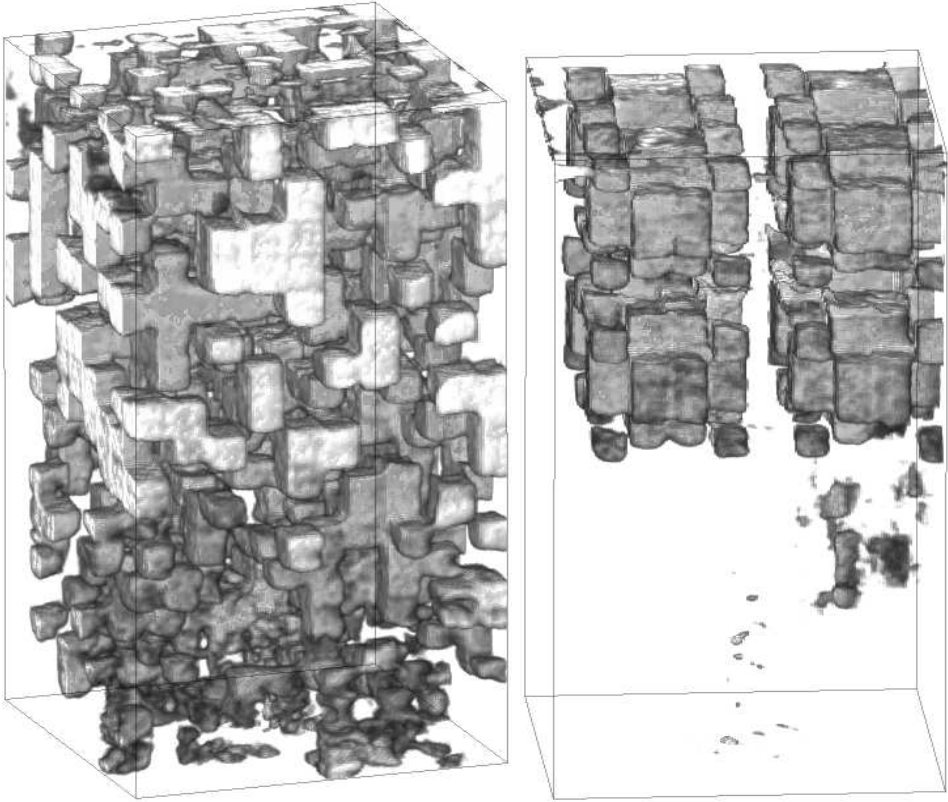
Figure 8.8: The random (left) and periodic (right) sand column drained by a pressure head of $-30\,\text{cm}$, applied at the lower boundary. The segmentation of the tomograms shows the dry sand cubes. All cubes with very fine sand are still wet and therefore set transparent by the segmentation.

other column is *periodically* packed with patterns of fine sand, that is surrounded by very fine sand (figure 8.8).

The main goal of the experiments is, to compare the flow between different soil structures for the same initial and boundary conditions. Since the structures of the sand columns are exactly known, the influence of the connectivity on the flow can be investigated by comparing the results for the two columns with and without connected structures.

In order to have well defined initial conditions, where the whole pore space is saturated with water (no air inclusions), the sand columns are flushed with CO_2 and subsequently with water. Since CO_2 is getting dissolved in water, the CO_2 bubbles disappear and water fills the whole pore space. Beneath the sand

material is a porous plate, that is connected to a water reservoir. This reservoir is adjustable in height by remote control, so that it is possible to change the pressure head applied at the porous plate during the measurements. The pressure head is measured in centimeters below the bottom of the sand column. Additionally, the water reservoir is on a balance, so that the total amount of water drained from the column and collected in the reservoir is known during the whole experiment.

The measurement consists of a stepwise drainage and imbibition of the columns. The applied pressure heads are $+20, 0, -10, -20, -30, -40, -50$ and $-30, -10$ cm. After changing the pressure head, the columns are radiographed each minute, until the mass of the water reservoir remains constant (~ 1 h). When the water content in the column is stable, it is tomographed, to obtain the three-dimensional distribution of the water for each pressure step.

Since the columns are 10 cm thick in beam direction, heavy water (D_2O) is used instead of normal water. The effective attenuation coefficient of D_2O is $\Sigma_{D_2O} = 0.493$ cm^{-1} at the NEUTRA facility and therefore about seven times less than for H_2O. For the sand the effective attenuation coefficient is calculated to $\Sigma_{Sand} \approx 0.3$ cm^{-1}. With a porosity of about 45 %, the total effective attenuation coefficient for the dry sand is

$$\Sigma_{dry} \approx 0.55 \cdot \Sigma_{Sand} \qquad\qquad \approx 0.165 \text{ cm}^{-1} \quad \text{and} \qquad (8.10)$$

$$\Sigma_{sat} \approx 0.55 \cdot \Sigma_{Sand} + 0.45 \cdot \Sigma_{D_2O} \approx 0.387 \text{ cm}^{-1} \qquad (8.11)$$

for the saturated sand. According to the exponential attenuation, the transmission is expected between 19 and 2.0 % for the 10 cm thick sand column. The situation is even harder for tomography, where the maximum transmission thickness is the diagonal of the rectangular columns. The transmission decreases in this case to about 9.7 to 0.42 %.

Therefore the calculation of the scattering contributions has to be very precise. An error of only ± 0.1 % in the calculation of the scattering results in a deviation of about ± 4 % in the water content. By the application of the correction algorithm as described in chapter 6, the scattering contributions are slightly overestimated, so that the transmission values become negative at the diagonal views of the saturated regions. Therefore the background scattering is reduced by 60 % of the mean background scattering value. Reducing the measured scattering by a constant value has the advantage that the gradients are unchanged. If the background scattering is reduced pixelwise by 60 %, the resulting water content values show a clear trend, that is similar to the measured background scattering. The reduction of 60 % is

justified by the fact that in the completely saturated state (pressure head $+20\,\text{cm}$), a thin layer of pure D_2O is on top of the sand. This layer represents a region with a well known attenuation coefficient. Therefore the background scattering is adjusted, until the complete correction algorithm yields the correct values for that region.

Figure 8.9 shows the evaluated thickness of the saturated column with the randomly arranged cubes in the $45\,°$-position before and after the correction. The uncorrected profile is completely smooth due to the scattering. The expected peak along the diagonal of the column reappears after the correction. The maximum thickness corresponds to the diagonal of the sand column ($14.1\,\text{cm}$). It is clearly seen, how strong the statistical noise becomes at these thicknesses.

With that adjustment of the correction algorithm, all the radiographs and tomograms are corrected with the same parameters and evaluated for the water content. Also the total amount of water in the columns is calculated and compared to the masses measured by the balance. The good agreement within $\pm 5\,\%$ for the two measurements is depicted in the diagrams of figure 8.10 for that column. For the measurement of the column with the periodically arranged cubes, the D_2O has been reused, after filtering it. The total masses of D_2O evaluated for that column deviate from the measurements by the balance. Therefore it is assumed that the D_2O has been contaminated with normal water from the air during the filtering. The assumption of $2\,\%$ H_2O and $98\,\%$ D_2O yields then the effective cross section $\Sigma_{\text{eff}} = 0.522\,\text{cm}^{-1}$ and the total masses agree again within $\pm 5\,\%$ compared to the balance measurements.

An example of a reconstructed horizontal slice through the random column is shown in figure 8.11. Again it becomes visible that the noise is increased by the correction. This leads also to more reconstruction artefacts. But the improvements are evident: after the correction, the gray values have defined values, that correspond to the attenuation coefficients of the sample and the typical depression in the center has disappeared. Further, the blurring has been significantly reduced and more details become apparent.

A series of vertical slices through the random column at the tomographed pressure steps is depicted in figure 8.12. It is visible, how the cubes with fine sand are drained before the cubes with the very fine sand. Also the hysteresis is observable for the pressure heads -30 and $-10\,\text{cm}$, by comparing the corresponding slices for the drainage and imbibition.

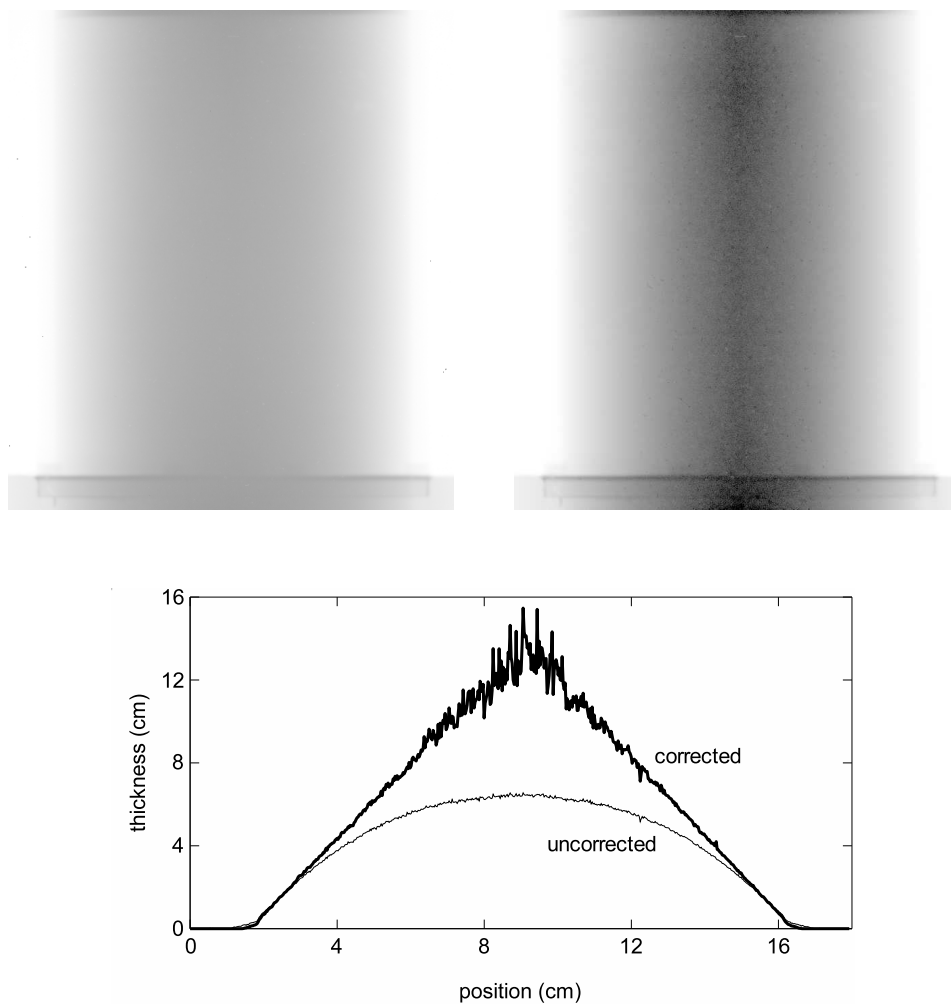In the tomographic slices (d)–(g) of figure 8.12 not only the sand cubes are

Figure 8.9: Top: Images of the evaluated thickness of the saturated random column in the 45 °-position (white means small thickness), before (left) and after (right) the corrections. Bottom: Horizontal profiles through the above thickness images.
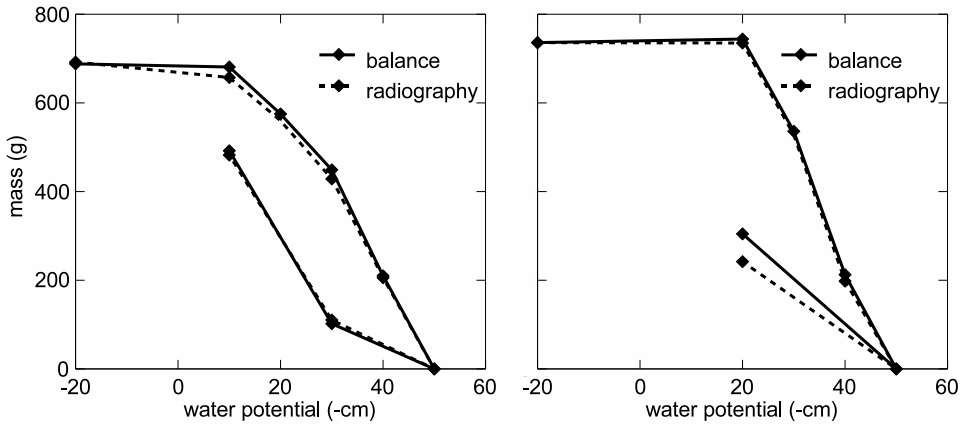
Figure 8.10: Total mass of water in the columns with the randomly (left) and periodically (right) arranged sand cubes, measured by balance (dashed line) and radiography (solid line). The deviations are $\pm 5\,\%$ except the last measurement of the periodic column, where the balance is not reliable, because the setup has been slightly displaced.
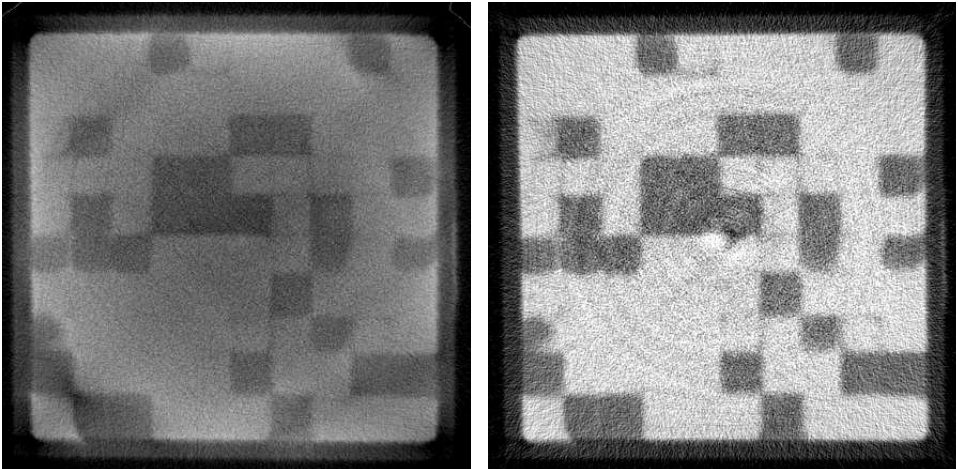

Figure 8.11: Horizontal slices through the drained column (randomly arranged cubes) at the pressure head $-40\,$cm, before (left) and after (right) the correction.

(a) +20 cm, saturated   (b) −10 cm, drainage   (c) −20 cm, drainage

(d) −30 cm, drainage   (e) −40 cm, drainage   (f) −50 cm

(g) −30 cm, imbibition   (h) −10 cm, imbibition   (i) dry
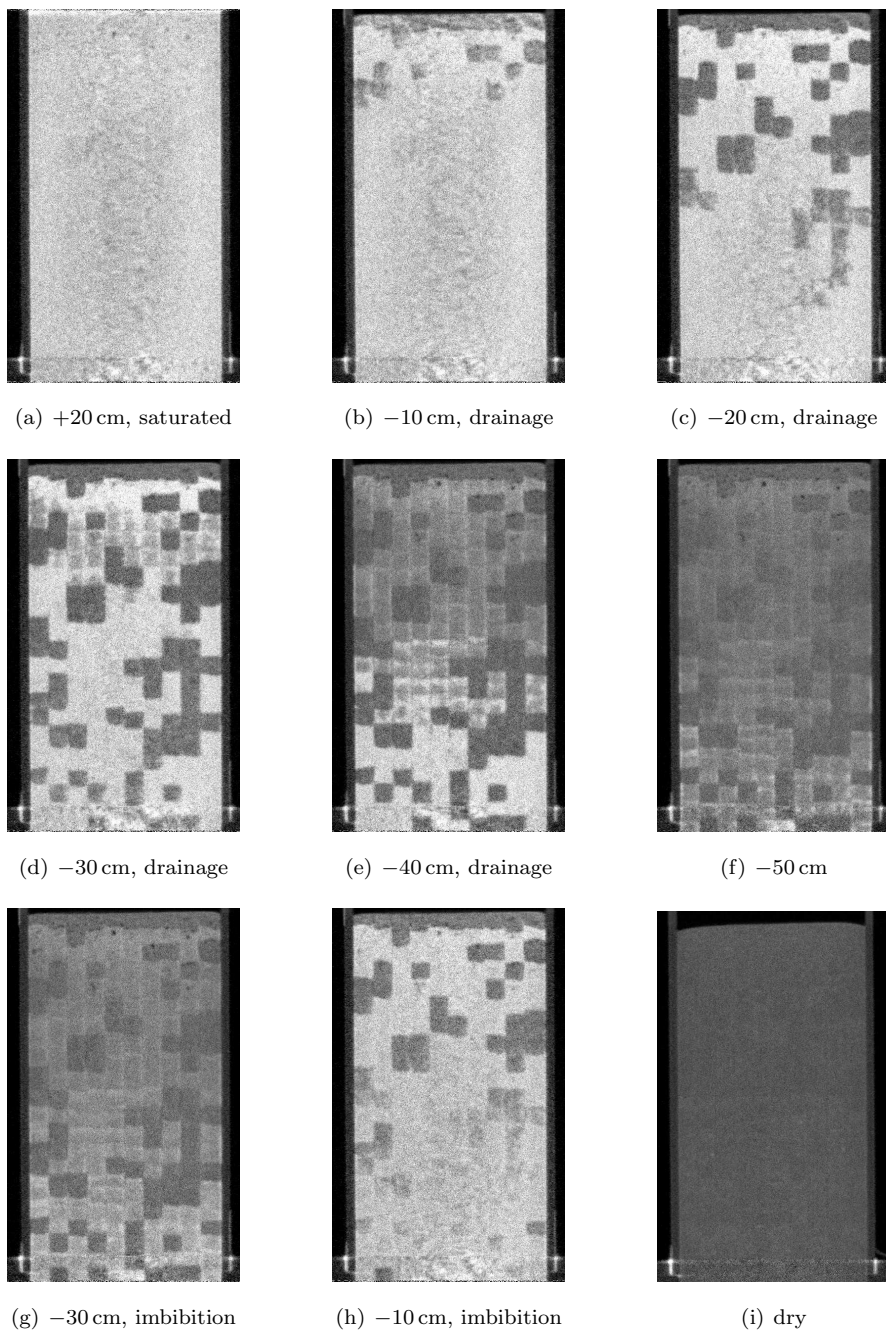
Figure 8.12: Vertical slices through the column with the randomly arragend cubes at the indicated pressure heads (white means high water content). The last tomogram (i) is recorded after drying the column for one week in the oven.

visible, but also the interfaces between the cubes show up as bright lines, i.e. as areas with a higher water content. This effect has been observed the first time in a similar experiment of P. Lehmann and J. Schaap. It has not been expected there, only the neutron tomography has revealed it. The reason for these interfaces is the packing technique for the cubes with thin sheets, that have been used for the separation of the cubes during the packing process. After completing a horizontal layer, the sheets are gently pulled up but leave despite the carful removal areas with a higher porosity. The exact properties of these interfaces and their meaning for imbibition and drainage processes are a current topic of investigations.

More results from the soil physical point of view are published in [26, 27].

8.3   Applicability for Other Facilities

An important goal of this thesis is that the correction algorithm is not only usable for the NEUTRA facility, where it has been developed, but also other facilities should benefit from it. Therefore the teams of the ANTARES (Munich), CON-RAD (Berlin), and SANRAD (Pretoria) facilities collaborate and have performed common experiments with well defined samples.

8.3.1   SANRAD – CONRAD – NEUTRA

One of these common experiments has been performed together with F. de Beer (Necsa, Pretoria) and N. Kardjilov (Hahn-Meitner Institute, Berlin) within the IAEA research project "neutron scattering corrections for neutron radiography" (ref-no. 302-F1.20.15-SAF-12455). Several slabs of stainless steel, aluminum and copper with various thicknesses are radiographed with varying sample-detector distances at the three facilities SANRAD, CONRAD and NEUTRA.

The evaluation of the stainless steel radiographs are presented here as examples. The dimension of the different slabs is $5 \times 5 \, cm^2$ with a thickness between 0.7 and 10 mm, and the chosen sample-detector distances are 0.5, 2, 3 and 5 cm. Although the correction algorithm for the background scattering has already been developed at the time of the measurements, it has not yet been described. Therefore the background scattering behind a black body has been recorded only at the NEUTRA facility. All the radiographs are corrected for the spectral effects and the sample scattering, and the radiographs recorded at NEUTRA additionally for the background scattering. As mentioned in section 3.1.1 the spectrum of the CON-RAD facility is simulated, and for the SANRAD facility the NEUTRA spectrum
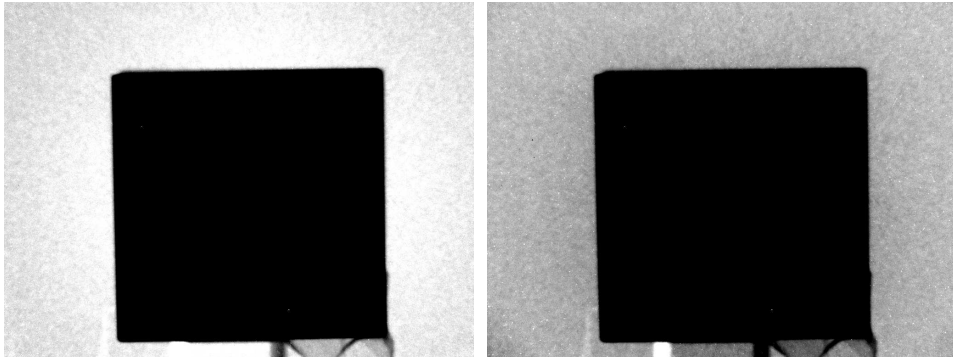
Figure 8.13: Transmission image of a stainless steel slab ($5 \times 5 \times 1 \, \text{cm}^3$), recorded at NEUTRA with the sample-detector distance 2 cm. The image before the correction (left) shows the typical sky shine due to sample scattering. Right: the transmission image after the correction of the spectral effects and the sample scattering (not the background scattering) with the same brightness and contrast settings as left.

is used, since the SANRAD spectrum is neither measured nor simulated yet.

The comparison of an uncorrected and a corrected transmission image shows that the radiographs contain a significant contribution of sample scattering, as visualized in figure 8.13. This is also depicted in the graphs of figure 8.14. For small detector distances, the evaluations after correcting the sample scattering are rather accurate. But for larger distances, the sample scattering is less relevant and the corrected evaluation converges with the uncorrected evaluation. Correcting only the sample scattering underestimates the sample thickness, since the background scattering pretends higher transmission values.

Taking also the background scattering into account for the NEUTRA measurements, yields for the larger detector distances results, that are within $\pm 5 \, \%$ accurate (figure 8.15). For the smaller detector distances, the sample scattering is overestimated and therefore also the evaluated thickness. These deviations have a large effect, since the scattering is distributed approximately like $1/r^2$. This is again the same finding as for the iron step wedge presented in section 8.1.2.

Also the figures 8.14(a) and (b) for the SANRAD and CONRAD facilities show an underestimation of the evaluated thicknesses. It is not clear, how accurate the results would become, if the background scattering was measured. But for sure, the evaluated thicknesses would become greater.
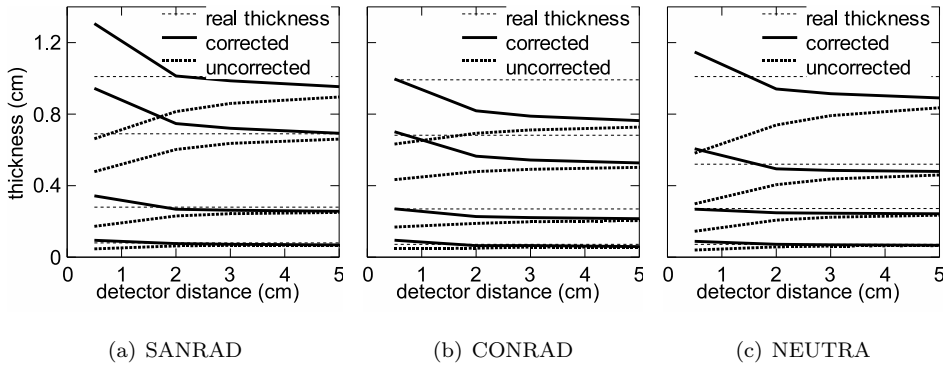
(a) SANRAD   (b) CONRAD   (c) NEUTRA

Figure 8.14: Evaluated thicknesses of the stainless steel slabs recorded at the SAN-RAD, CONRAD and NEUTRA facility. The graphs show the real thickness of the sample (thin dotted) compared to the evaluation without correction (thick dotted) and after the correction of the sample scattering (thick solid).
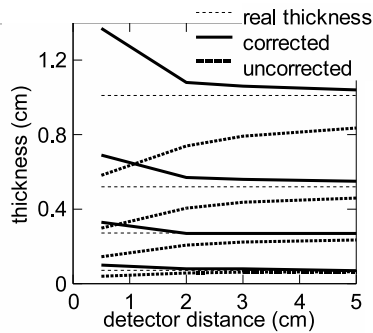

Figure 8.15: Evaluated thicknesses of the stainless steel slabs recorded at the NEU-TRA facility. In addition to the graphs of figure 8.14(c), also the background scattering is considered. The corrected results (thick solid) tend to the real sample thicknesses (thin dotted).

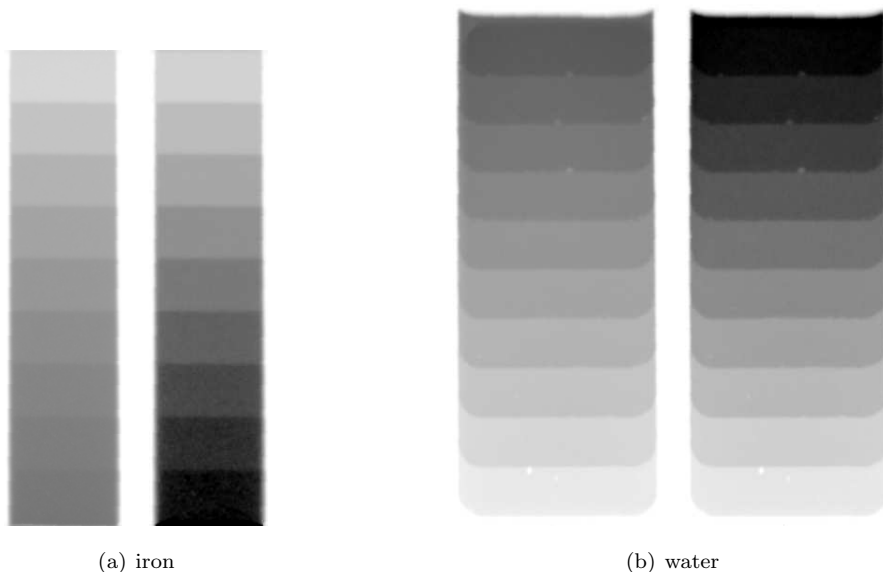(a) iron   (b) water

Figure 8.16: Transmission images of the iron and water step wedges in a logarithmic gray scale (left: uncorrected, right: corrected, both with the identical brightness and contrast settings).

8.3.2   ANTARES

The correction algorithm is tested also at the neutron radiography facility AN-TARES in Munich. Because the ICON facility has been constructed, when these measurements have been performed and the spectrum is expected to be similar to the ANTARES spectrum, these results are also a forecast for the ICON facility. Iron and water step wedges are investigated as typical materials. Since the ANTARES spectrum and the used Li-scintillator are known, the corresponding PScF for these materials are already computed previous to the experiments. With that it is possible to compute the corrections without further access to MCNPX.

Figure 8.16 shows the transmission of the iron and water step wedges. The iron step wedge is the same as used as a test sample at the NEUTRA facility (section 8.1.2). The steps have the thicknesses 1, 1.5, 2, ..., 5 cm, each 1 cm high and 2 cm wide. The water steps have also the height 1 cm, the thicknesses are 0.5, 1, 1.5, ..., 5 mm. The sample-detector distances are varied from 1 to 20 cm. The results after the corrections are very similar for all distances, except for the distance 1 cm, where again the small overestimation of the computed scattering has a large effect.

The radiographs are corrected for the sample scattering, background scattering and the spectral effects. The resulting vertical profiles through the center of the step wedges are depicted in figure 8.17. The remaining error for the iron step wedge (figure 8.17(a)) is 20 to 25 %. This is worse than expected by the measurements at NEUTRA. The reason for this is that the ENDF neutron cross section libraries [28] are implemented in MCNPX and they do not take the Bragg edges into account. Since all cross section data for the corrections are taken from MCNPX, the remaining error after the correction is relatively large for facilities with a cold neutron spectrum. Figure 8.18 shows the Bragg edges for iron, calculated with a programm written by J. Santisteban (The Open University, UK), compared to the ENDF data used by MCNPX. The two graphs deviate below $\sim 4\,$meV, where the ANTARES spectrum has its maximum. Therefore it becomes clear that the effective cross section for the ANTARES spectrum is overestimated, what results in too small evaluated thicknesses.

Fortunately, the cross section of water has no Bragg edges and MCNPX has implemented the $\mathcal{S}(\alpha, \beta)$ libraries for hydrogen in water, that contains accurate scattering cross sections also for low neutron energies. Therefore the evaluation of the water step wedge is again rather precise (figure 8.17(b)). As in the other experiments, the accuracy is here within $\pm 5\,$% for all sample-detector distances from 2 to 20 cm.
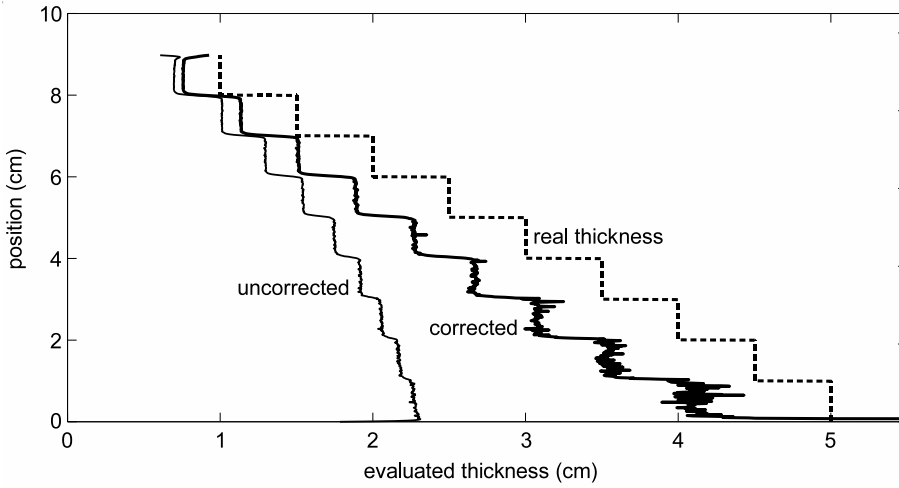
(a) iron
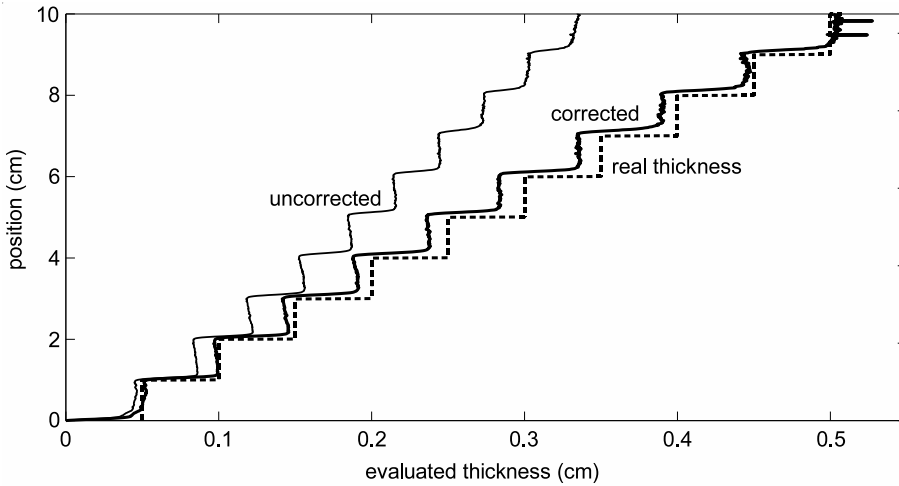
(b) water

Figure 8.17: Vertical profile through the center of the evaluated thicknesses of the iron and water step wedges at the detector distances 6 cm (thin line: without, thick line: with correction). The dashed line shows the real thickness of the steps.
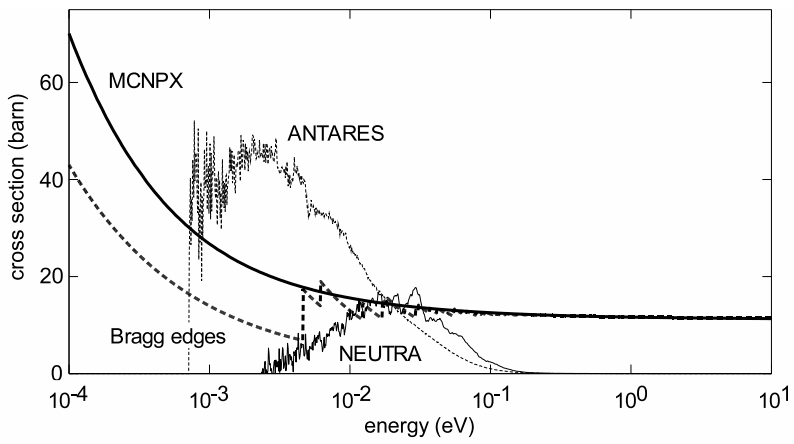
Figure 8.18: Microscopic cross sections for iron used by MCNPX compared to the calculated Bragg edges (fcc structure). The energy spectra of NEUTRA and ANTARES are overlayed, to show the relevance of the Bragg edges for the thermal and cold neutron radiography (thin lines, units 1/eV).

Chapter 9

Conclusions

Neutron radiography is established as a suitable and in some cases most successful tool for non-destructive testing of materials. This is shown by the various scientific applications as well as by the industrial use.

Since the outcome of this thesis is a method, that can be practically used for the evaluation of neutron radiographs and tomograms, the approach is to simplify everything as much as possible and to concentrate on the relevant points. This means that the huge facility, that is requiered to produce a well thermalized, parallel neutron beam, is just described by the energy spectrum and the intensity at the beam exit. Another strong simplification concerns the neutron scattering reactions. Although the single scattering events are physically well understood and described, only the totality of all scattering processes is considered here. This means that only the distribution of scattered neutrons on the imaging detector is inspected, instead of the single scattering events. For this reason, the Monte-Carlo simulations are an ideal tool. They follow each single neutron, considering the physical constraints, but provide as a result only the relevant statistical mean behaviour of the neutrons.

9.1   Facilities

Each neutron radiography facility has its own specific properties. Concerning the correction algorithm, particularly the energy spectrum of the beam and the energy dependent absorption rate of the detector system are interesting. As seen from the experiments at different facilities, the exact knowledge of these properties is decisive. The spectrum can be measured by a time of flight experiment. Since the contribution of the epithermal neutrons is not registered by this measurement,

there is a remaining uncertainty about the calculation of the effective cross sections. It would be possible to calculate the spectrum for higher energies by simulations. However, these calculations are very extensive and because of the complex systems, that are involved, the results must be considered with caution. Therefore these calculated spectra may yield a good estimation, but they should be experimentally verified anyway.

For the satisfying outcome of an experiment, it is most important to have the appropriate detector system available. Depending on the investigated problem, it is important to have either a high spatial or time resolution. Since always a compromise must be found, it is important to have the choice of several different detector types.

For the calculation of the detector absorption rate, it is assumed that the cross section for the neutron detection reaction is much larger than for all other occuring neutron reactions in the detector. Then it is easy to calculate the absorption rate, if the detector material, thickness and atomic density are known. If they are not provided by the manufacturer, it is possible to measure their impact to the absorption rate by a radiograph of the detector itself.

Although neutron and X-ray radiography facilities differ strongly at first view, they have a lot in common, if the beam production and the atomic reactions are disregarded. From the experimental point of view, there are e.g. the same or only slightly modified detectors in use. The main disturbing processes are – from a macroscopic point of view – the same: scattering at the sample or its surroundings and beam hardening. Also the software tools for the evaluation of the measured data are identical. Therefore the sophisticated tomographic reconstruction algorithms can be reused. This allows to focus on the physical distortions of the radiographs instead of the numerical artefacts. As a further consequence, it is conceivable to transfer the presented correction algorithm also to the X-ray radiography.

9.2   Monte-Carlo Simulations

The Monte-Carlo simulation of neutron radiographs has been a very valuable tool for the elaboration of the correction algorithm. It allows to understand the impact of the different neutron interactions in detail, by separating the corresponding effects. Also for the application of the correction algorithm, it is necessary to have a simulation tool available. For every combination of material, neutron spec-

trum and detector, the PScF must be calculated. These simulation results are reusable for later experiments with the same material-spectrum-detector combination. Therefore a library of simulated PScF can be accumulated, so that the use of the simulation software becomes more and more rare.

MCNPX has proven to be a good choice as a simulation tool. It has implemented the neutron cross sections of all natural isotopes, and it offers a great flexibility for the simulated arrangement and various possibilities of neutron tallies. Although the final input files for the simulations look relatively simple, a certain experience is necessary to compose them according with the experimental validations.

Unfortunately, MCNPX provides only for a few materials precise scattering libraries. For all other materials, the free gas model is used as an approximation. Since most of the inspected samples consist of very common materials and do not have predominant atomic structures, that could cause strongly anisotropic scattering, this simplification provides still good results for thermal neutrons. But it causes larger deviations for the cold neutron radiography. Because this method is in great demand due to the higher resolution and sensitivity, already several cold neutron radiography facilities are operated. Therefore it makes sense, to continue the topic of quantitative neutron radiography with the focus on cold neutrons.

9.3 Correction Algorithm

As main causes for the disturbance of the quantitative information in neutron radiography, the neutron scattering in the investigated sample and at its surroundings are identified. The spectral effects due to the polyenergetic neutron beam and the energy dependent cross sections of the sample and detector materials play a minor role for most materials. Nevertheless they must be taken into account for best possible quantification results.

In order to obtain the most accurate quantitative results from a measurement, experimental actions as well as subsequent calculative processing are requiered. Experimentally, the beam has to be limited as narrow as possible around the sample, to minimize the scattering of neutrons from the surroundings or shielding to the detector. The remaining background scattering is measured behind a black body, that is opaque for neutrons. Further, it is possible to reduce the statistical error considerably by the accumulation of several radiographs. This is particularly recommended for the recordings of the open beam, the background scattering and the CCD dark current, if applicable. Of course, it is not always possible to

record several radiographs of the sample at time critical experiments or tomograms. But for single radiographs of a sample, only a small effort is required for multiple recordings of the sample, and they have a large effect.

The computational processing of the measurement removes the measured background scattering as well as the sample scattering, that is composed of the simulated PScF. For the evaluation of the transmitted mass thicknesses, effective attenuation coefficients are used, that take the neutron energy spectrum and the detector properties into account.

The validation of the correction algorithm with radiographs of defined test samples shows that it is possible to reduce the systematic error to about $\pm 5\,\%$. This accuracy is expected also for relevant measurements of unknown samples. If the radiograph includes a region with known sample properties, it is possible to improve the accuracy by "manually adjusting" the scattering contribution. Superposed to the systematic error, there is always a statistical error, that increases after the corrections. Mainly the statistical error gives then the limits for the quantifiable mass thicknesses. Since this error is predictable previous to an experiment, it should be considered in the planning of an experiment.

The measurements at the different facilities show that the correction algorithm is not only applicable to the NEUTRA facility, where the method has been elaborated. If the neutron energy spectrum and the detector properties are known and the experimental recommendations are realized, the algorithm yields accurate quantitative results for any facility.

Appendix A

MCNPX Code

A.1 Neutron Source Modelling

A non-divergent surface source for neutrons with the extension $10 \times 10\,\text{cm}^2$ at $z = -50\,\text{cm}$ is modelled by the data cards

```
c    neutron source
sdef par=n   erg=d1   vec=0 0 1   dir=0    x=d11 y=d12 z=-50
si11 h  -5    5                $ extension in x-direction
sp11 d   0    1                $ uniform distribution
si12 h  -5    5                $ extension in y-direction
sp12 d   0    1                $ uniform distribution
si1 h                         $ measured time of flight spectrum:
     8.07254e-10   8.11311e-10   8.15414e-10   8.19530e-10   8.23685e-10
     ...
     1.58661e-06   2.00805e-06   2.62277e-06   3.56985e-06   5.14061e-06
sp1 d
     0.00000e+00   5.13924e-03   9.09625e-04   6.35442e-04   4.69869e-04
     ...
     1.40068e-02   1.82160e-02   2.57787e-02   3.69753e-02   4.77998e-02
```

The distribution `D1` contains e.g. the ICON spectrum (not all 394 bins are printed here). A divergence of 0.2 degrees is added by the following additional distribution `D10` for the `vec` argument in the `SDEF` card:

```
sdef par=n   erg=d1   vec=0 0 1   dir=d10    x=d11 y=d12 z=-50
si10 h   0.9999939   1   $ uniform angular distribution 0.2 - 0deg (cos)
sp10 d   0           1
```

A.2   Detector Modelling

The code for a detector plane at $z = 10\,\mathrm{cm}$ (surface 520) with the extension $10 \times 10\,\mathrm{cm}^2$ (surface 500) and the pixel size $200\,\mu\mathrm{m}$ (surface 510) is modelled by the cards

```
c     cell cards
50    0    -500    fill=1                imp:n=1           $ enclosing detector box
51    0    -510    fill=2 lat=1 u=1  imp:n=1           $ detector cell
52    0    -520                  u=2  imp:n=1           $ front of detector plane
53    0     520                  u=2  imp:n=1           $ behind detector plane

c     surface cards
500   box  -5 -5  9.9    10     0 0   0 10    0   0 0 0.2 $ enclosing detector box
510   box  -5 -5  9.9     0.02 0 0   0  0.02 0   0 0 0.2 $ detector cell
520   pz         10                                       $ detector plane

c     data cards
f1:n  (520<51[0:499 0:499 0:0]<50)
de1 log
      1.00000e-09    1.77828e-09    3.16228e-09    5.62341e-09    1.00000e-08
      1.77828e-08    3.16228e-08    5.62341e-08    1.00000e-07    1.77828e-07
      3.16228e-07    5.62341e-07    1.00000e-06    1.77828e-06    3.16228e-06
      5.62341e-06    1.00000e-05    1.77828e-05    3.16228e-05    5.62341e-05
      1.00000e-04
df1 log
      9.99300e-01    9.95703e-01    9.83230e-01    9.53344e-01    8.99511e-01
      8.21670e-01    7.25676e-01    6.20855e-01    5.16827e-01    4.20620e-01
      3.35995e-01    2.64562e-01    2.06035e-01    1.59070e-01    1.22031e-01
      9.32176e-02    7.09538e-02    5.39421e-02    4.09569e-02    3.11190e-02
      2.36599e-02
```

The DE and DF cards are the multipliers for a ^{6}Li-detector. They represent the absorption rates A^{det} (DF) for the energies DE (in MeV). Both sequences are logarithmicly interpolated for the energy of an incident neutron.

A.3   PScF Simulation

Figure A.1 shows the simulated geometric setup for the PScF. The outer boundaries are given by the cubic box from -10 to $+10\,\mathrm{m}$ for the x, y, z-coordinates.

```
c     cell cards for the void and the rest of the world
90    0    -300          -900    imp:n=1   $ void in front of the sample
91    0     301   500    -900    imp:n=1   $ void behind the sample without detector
```
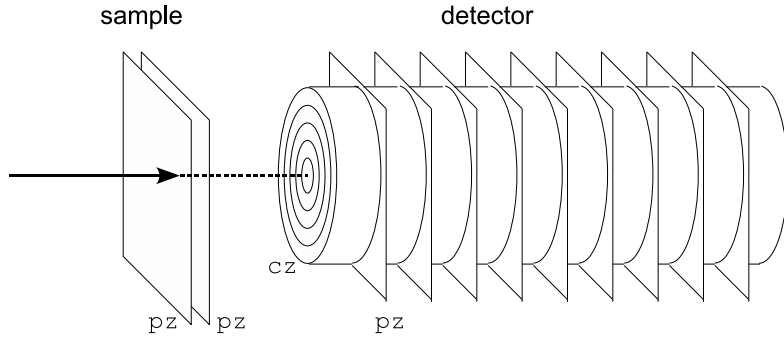
Figure A.1: The simulation geometry for the PScF. The space between the two planes is filled with the sample material and the detector is modelled as concentric rings, that are implemented by intersections of the detector planes with cylinders.

```
99   0                    900    imp:n=0   $ rest of the world


c    surface cards for the simulation boundaries
900  box -1000 -1000 -1000   2000 0 0   0 2000 0   0 0 2000
```

The source is located at $(0, 0, -999 \, \text{cm})$ and directed along the z-axis. The number of particles (NPS) is set to 10^7, which provides a good neutron statistic so that it is possible to approximate the results by analytic functions.

```
c    source
sdef erg=d1   vec=0 0 1   dir=1   x=0 y=0 z=-999
c    number of particles
nps  10e6
c    energy spectrum
si1 h   ...
sp1 d   ...
```

The sample is e.g. a 1 mm thick water layer ($^1\text{H}_2\text{O}$) with the density $1 \, \text{g/cm}^3$. For water the cross section libraries $\mathcal{S}(\alpha, \beta)$ are available (LWTR.01T).

```
c    cell card
30   301   -1      300   -301  -900                imp:n=1


c    surface cards
300  pz -0.1     $ front and back surface. the lateral extension is given
301  pz 0        $ by the boundaries to the rest of the world.


c    material cards for water
m301  1001.60c 0.666667    8016.60c 0.333333    $ H2O
mt301 lwtr.01t
```

The detector surfaces are defined by the intersection of the detector planes (PZ)
with the concentric cylinders (CZ). This is implemented by nested universes. The
universe U=1 consists of the cylinders and is filled by the universe U=2, which
contains the detector planes. The intersection is done in the tally cards, e.g.
f011:n (1501<1001<50) means "the first plane (1501, distance 1 cm) *in* the first
ring (1001, radius 0.1 cm) *in* the detector cell (50)". The tally numbering is so that
F011 has the distance 1 cm, F021 2 cm, etc. (the last digit must be 1, because this
is the designator for a surface tally). The energy dependent absorption rate of the
detector is given in the cards DE*dd*1 and DF*dd*1 (cf. appendix A.2). The FT*dd*1
and FU*dd*1 cards separate the uncollided neutrons (0 scattering events) from the
collided neutrons (1 to 1000 scattering events) in the detector. The F1 tally counts
the total number of neutrons, but for the PScF this value must be divided by the
detector area. This is done by the SD*dd*1 card, which divides the tally values by
the area of the rings.

```
c     cell cards for the detector
50   0    -500              fill=1   imp:n=1   $ whole detector cell
1001 0          -501   u=1 fill=2   imp:n=1   $ ring   1
1002 0    501   -502   u=1 fill=2   imp:n=1   $ ring   2
1003 0    502   -503   u=1 fill=2   imp:n=1   $ ring   3
...
1200 0    699   -700   u=1 fill=2   imp:n=1   $ ring 200
1999 0    700          u=1 fill=2   imp:n=1   $ outside rings
c
1501 0          -1501   u=2          imp:n=1   $ front of plane 1
1502 0    1501 -1502   u=2          imp:n=1   $ between plane 1 and 2
1503 0    1502 -1503   u=2          imp:n=1   $ between plane 2 and 3
...
1520 0    1519 -1520   u=2          imp:n=1   $ between plane 19 and 20
1521 0    1520          u=2          imp:n=1   $ behind plane 20

c     surface cards for the detector
501  cz  00.1     $ detector cells
502  cz  00.2
...
700  cz  20.0
c
1501 pz  1        $ detector planes
1502 pz  2
...
1520 pz 20

c     tally cards
```

```
f011:n   (1501<1001<50) (1501<1002<50) (1501<1003<50) (1501<1004<50)
         (1501<1005<50) (1501<1006<50) (1501<1007<50) (1501<1008<50)
         ...
         (1501<1197<50) (1501<1198<50) (1501<1199<50) (1501<1200<50)
sd011  0.031415927 198i 12.534955
de011  log 1.000000e-09   4.092607e-09   6.151769e-08   1.000000e-05
df011  log 6.870684e-01   4.436086e-01   1.380384e-01   1.180321e-02
ft011  inc
fu011  0    1000
c
f021:n   (1502<1001<50) (1502<1002<50) (1502<1003<50) (1502<1004<50)
...
f201:n   (1520<1001<50) (1520<1002<50) (1520<1003<50) (1520<1004<50)
...
```

Finally, the result is printed to a mctal-file, that is machine-readable:

```
prdmp 2j 1
```

Appendix B

QNI – Implementation of the Correction Algorithm

Beside the scientific elaboration of the correction methods for quantitative neutron imaging, there is a great demand from the neutron imaging groups for using this know-how in the everyday practical work. For this purpose the software tool "QNI – Quantitative Neutron Imaging" with an implementation of the correction algorithms is developed. The program is written in IDL (Interactive Data Language) [29] and provides the following features:

- All correction methods described in section 6.4 are implemented (CCD dark current, median filtering, background scattering, sample scattering, spectral effects, intensity correction, flat-field correction).

- Single radiographs and tomograms can be corrected, as well as series of radiographs and tomograms.

- The output of the program is
  - for radiographs: a transmission image, that obeys the exponential law of attenuation or the evaluated sample thickness, mass or mass thickness, respectively.
  - for tomograms: the attenuation coefficients, densities or material contents as a three dimensional volume.

- Referenced values may be obtained to a given radiograph or tomogram. This allows to see changes within the sample. For example in the experiment

about the out- and inflow into structured sand columns (section 8.2.3), the completely dry column is the reference measurement. The water content in the columns is then obtained by subtracting the attenuation coefficients of the dry column from the attenuation coefficients of the wet column.

- Various spectra, detectors and materials can be managed by the program. It is possible to export / import them, so that they can be exchanged by members within an imaging group and also between different groups.

- Support for the simulation of the PScF with MCNPX:

  - The input files for a combination of spectrum, detector and material are generated.

  - The results of the simulation are read by the tool. This includes the calculation of the effective attenuation coefficient (section 6.3) and the approximation of the simulated PScF (section 6.1.2).

- The parameters for the corrections are fetched by a wizard. Therefore the input is structured and the user is asked only for the values, that are actually needed.

Working with QNI

A general workflow for using QNI is depicted in figure B.1.

1. The properties of the experimental setup must be specified. This includes the neutron energy spectrum of the facility, the detector used for the measurement and the materials occurring in the sample.

2. For all materials of the investigated sample, the MCNPX input files are created. After running the simulation, the mctal output files are read by QNI and collected in the PScF library.

3. The correction methods to calculate and the corresponding parameters are specified.

4. The evaluations are specified. Note that more than one evaluation per radiograph / tomogram is possible. For example, evaluation of multiple regions of interest or evaluation of the transmission image and thickness.

If the needed PScF are already available from a former experiment, one can start directly with the specification of the correction parameters (3).
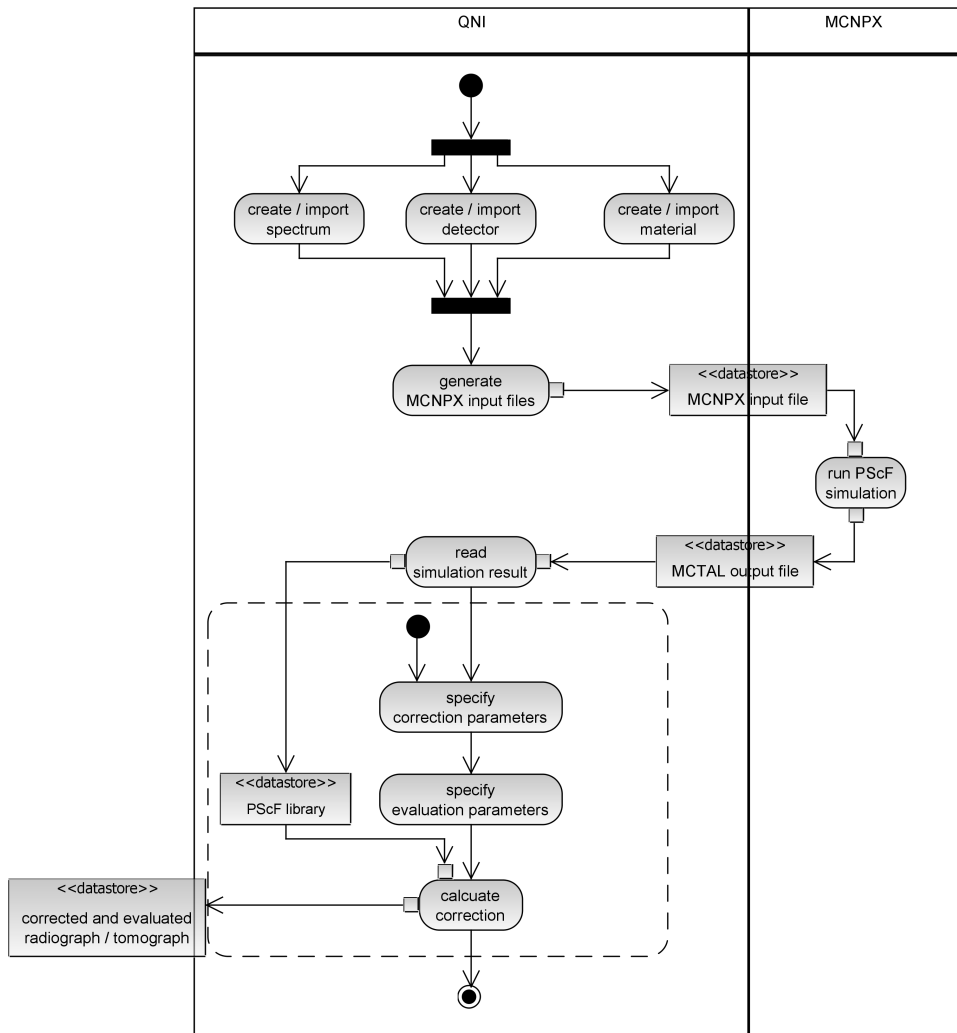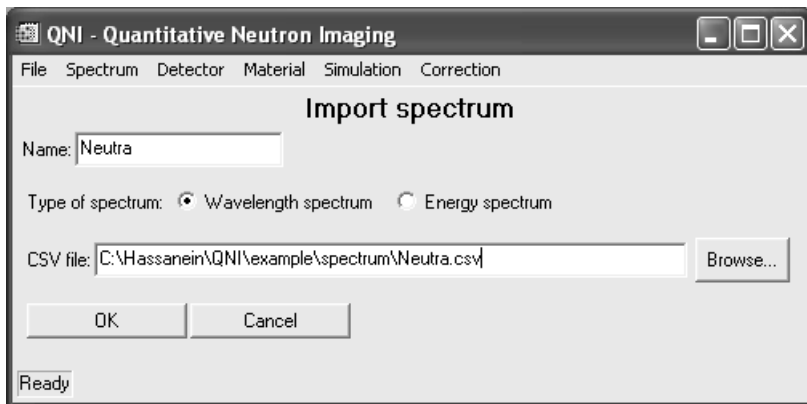
Figure B.1: Workflow for using QNI.

Figure B.2: Specification of the spectrum by a csv file.

Spectrum / Detector / Material Specification

The spectrum is specified by a file with comma separated values (csv), ideally resulting from a time of flight measurement (figure B.2). The first column contains the upper limits of the measurement intervals, either the wavelengths or the energies. The second column contains the neutron counts in the corresponding interval. The first count must be zero, because no neutron is expected below the first *upper* limit.

For the detector specification a wizard for the detector materials ^{6}Li and ^{nat}Gd is implemented (figure B.3). The wizard calculates from the prompted values the mass thickness and the corresponding absorption rates.

The sample materials are specified either by isotopes or by natural elements and their fractions (figure B.4). It is possible to combine an arbitrary number of isotopes and elements, respectively. The isotopes with $\mathcal{S}(\alpha, \beta)$ libraries in MCNPX are also available in QNI. For example "H-1" corresponds to the free gas hydrogen, "H-1-lwtr.01t" to hydrogen in light water, and "H-1-poly.01t" to hydrogen in polyethylene at room temperature.

PScF Simulation

After choosing the combination of spectrum, detector and material, QNI writes the MCNPX input files to the specified directory (figure B.5). Each file contains the simulation of the PScF for a specific material thickness. The generated number in the filename has the format `ett`. The material thickness times the estimated effective attenuation coefficient is then given by $\mathtt{tt} \cdot 10^{\mathtt{e}-1}$. The `000`-file contains
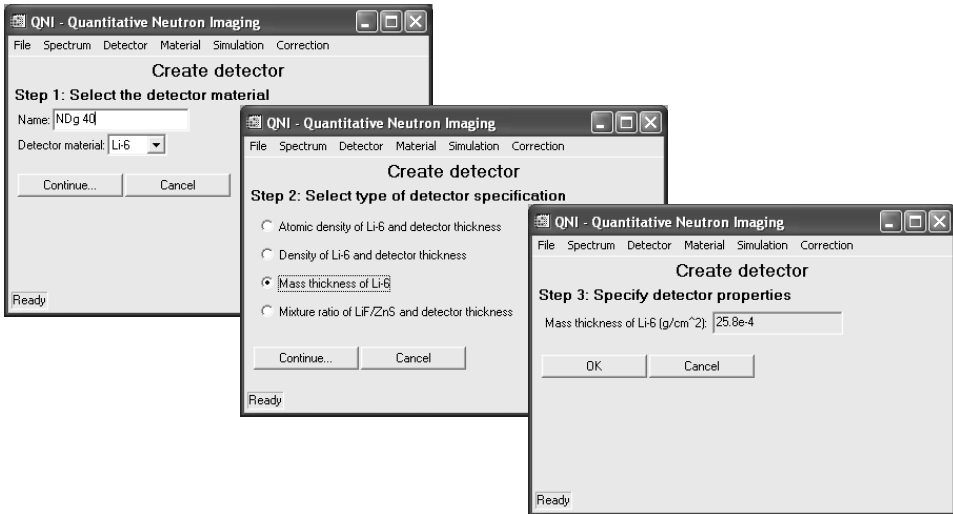
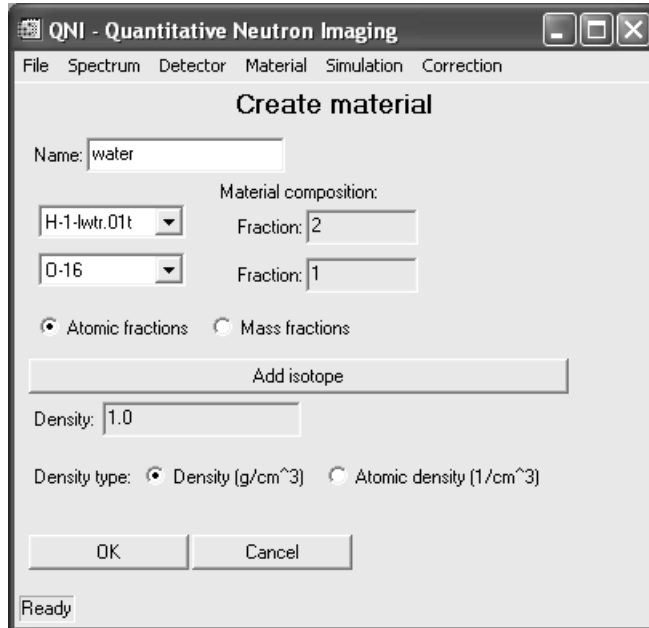Figure B.3: Specification of the detector properties (cf. section 8.1.1).

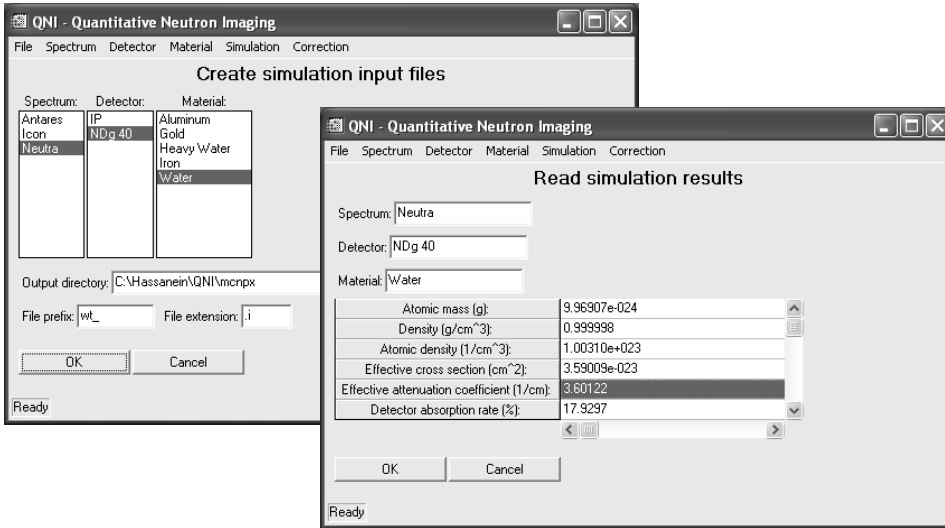Figure B.4: Specification of the sample material.

Figure B.5: Specification of the sample material.

the open beam simulation. Every file must be run in MCNPX and yields a mctal file with the simulation results. These files are read again by QNI, that calculates the effective attenuation coefficients and the approximation of the PScF.

Correction Parameters

So far, the input is independent of the specific experiments and the obtained simulation results can be used for all experiments with the corresponding setup. After correcting some measurements, an extensive library of simulation results is available and doing the corrections becomes more and more comfortable.

If the simulation results for the sample materials are available, one has to decide for the corrections, that are necessary. The wizard prompts then all needed parameters. Screenshots of the parameter input are depicted in figure B.6.

Evaluation Parameters

A set of evaluation methods are available for the corrected transmission images or tomograms, respectively. Figure B.7 shows a screenshot with the evaluation parameters for a radiograph. Several evaluations per radiograph / tomogram can be specified.

The material properties used by QNI (e.g. effective attenuation coefficient, density, atomic mass) are displayed and can be saved to a text file. It is also
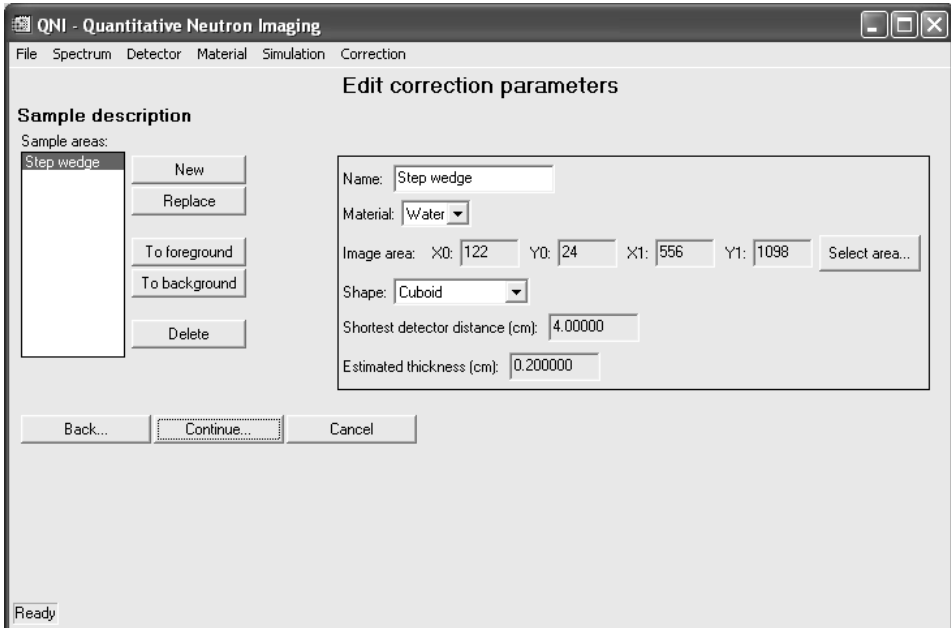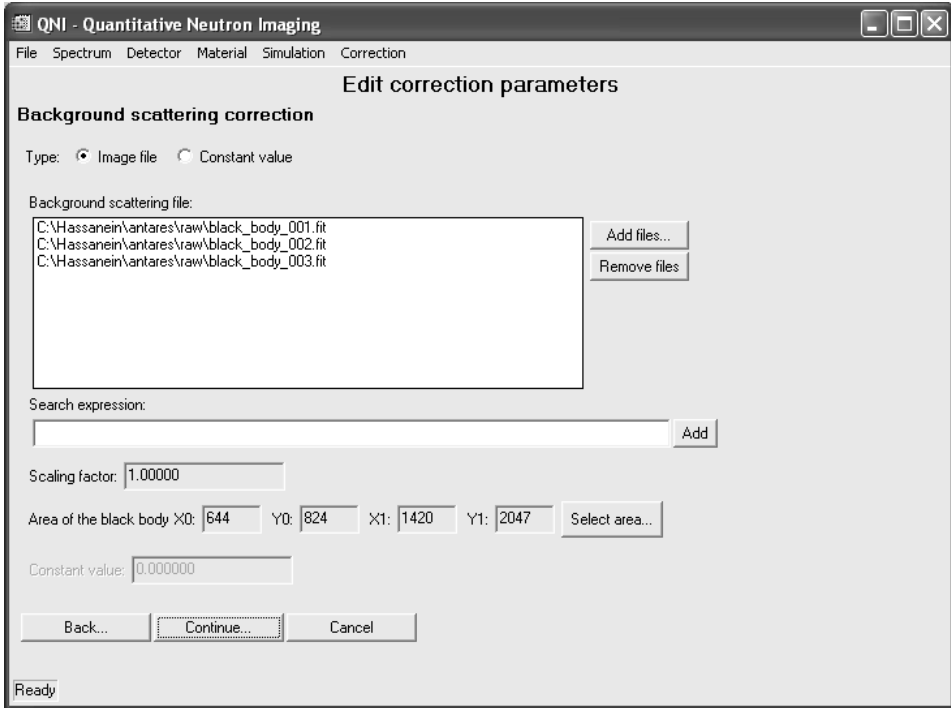
Figure B.6: Parameter input for the background (top) and sample scattering (bottom).
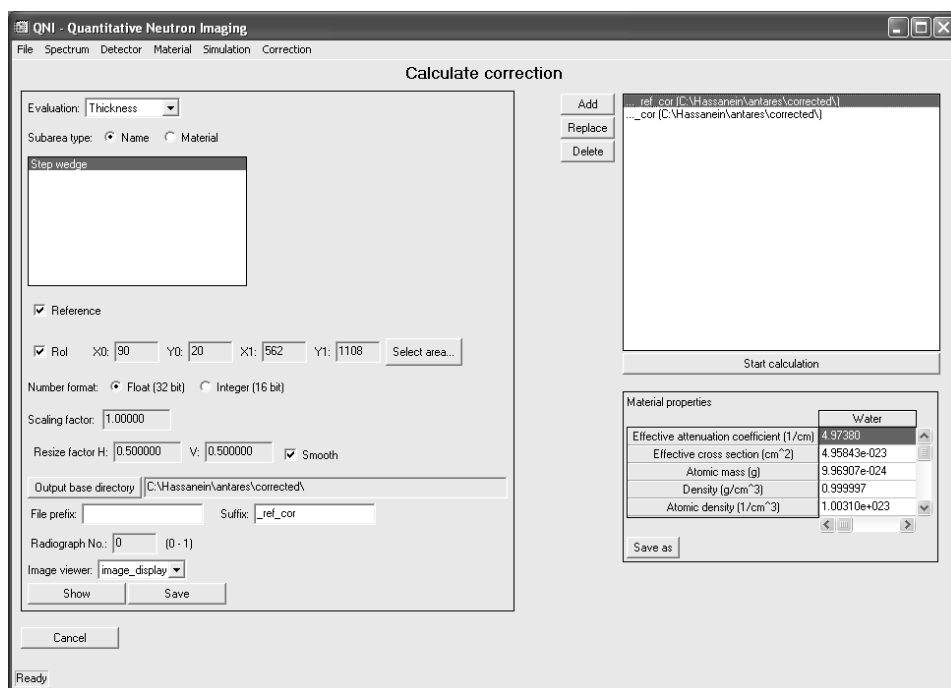
Figure B.7: Evaluation parameters for radiographs.

possible to save the correction and evaluation parameters. Thereby the image analysis is reproducible.

Results

The result are either saved to files for subsequent analysis with other programs or displayed by an image viewer. The IDL viewers iImage and iVolume provide some analysis tools as well as features for a good presentation of the results (figure B.8).
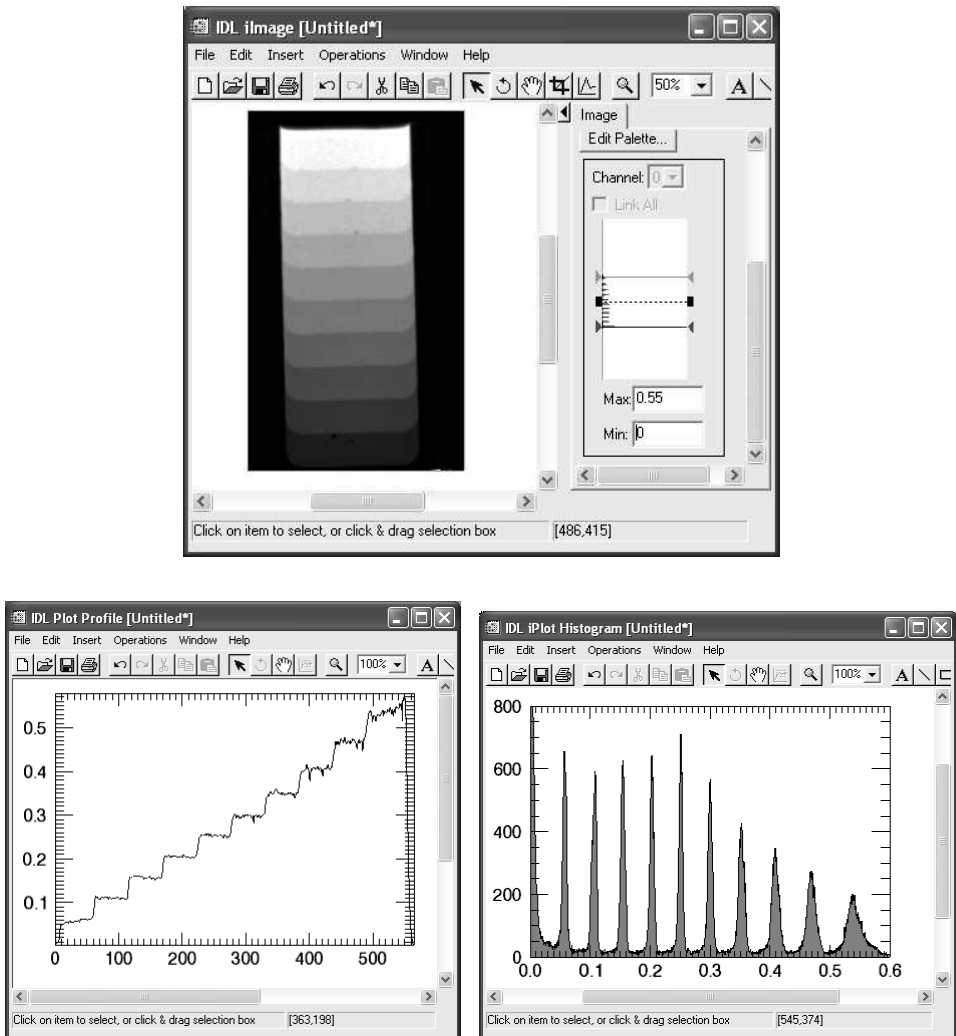
Figure B.8: Evaluated sample thickness of the water step wedge measured at ANTARES, cf. section 8.3.2. The bottom screenshots show a vertical profile through the center and the histogram.

Bibliography

[1] H. Pleinert, Determination of Moisture Distributions in Porous Building Materials – Neutron Signal Transfer Analysis, Aedificatio Verlag, Freiburg, 1998.

[2] N. Kardjilov, Further Developments and Applications of Radiography and Tomography with Thermal and Cold Neutrons, PhD Thesis TU München, 2003.

[3] A.A. Harms, D.R. Wyman, Mathematics and Physics of Neutron Radiography, D. Reidel Publishing Company, Dordrecht, 1986.

[4] A.C. Kak, M. Slaney, Principles of Computerized Tomographic Imaging, IEEE Press, New York, 1988.

[5] `http://neutra.web.psi.ch/facility/icon_index.html`

[6] E.H. Lehmann, P. Vontobel, L. Wiezel, Properties of the Radiography Facility NEUTRA at SINQ and its Potential for Use as European Reference Facility, Nondestructive Testing and Evaluation, Vol. 16, 2001, 191–202.

[7] `http://neutra.web.psi.ch`

[8] `http://www.physik.tu-muenchen.de/antares`

[9] `http://www.hmi.de/bereiche/SF/SF3/methods/ntomo/index_en.html`

[10] `http://www.necsa.co.za/content.asp?catId=18&Id=139&childId=103&node=3`

[11] `http://home.fujifilm.com/products/science/si_imgplate/img_plate.html`

[12] E. Lehmann, P. Vontobel, G. Frei et al., Neutron imaging – detector options and practical results, Nuclear Instruments and Methods in Physics Research A, 531, 2004, 228–237.

[13] E. Lehmann, P. Vontobel, The use of amorphous Silicon flat panels as detector in neutron imaging, Applied Radiation and Isotopes, 61, 2004, 567–571.

[14] L.S. Waters (Ed.), MCNPX User's Manual, Version 2.4.0, LA-CP-02-408, Los Alamos National Laboratory, September 2002.

[15] D.E. Cullen et al., Thermal Scattering Law Data: Implementation and Testing using the Monte Carlo neutron transport codes COG, MCNP and TART, U.S. Department of Energy, Lawrence Livermoore National Labatory, May 17, 2003.

[16] A. Carminati, A. Kaestner, O. Ippisch et al., Water flow between soil aggregates, Accepted for publication on Transport in Porous Media, 2006.

[17] N. Kardjilov, E. Lehmann, P. Vontobel, Representation of the image formation in applied neutron radiography in terms of a PSF superposition, Applied Physics A – Materials Science & Processing 74, 2002, 228–230.

[18] R. Hassanein, E. Lehmann, P. Vontobel, Methods of scattering corrections for quantitative neutron radiography, Nuclear Instruments and Methods in Physics Research A, 542, 2005, 353–360.

[19] R. Hassanein, F. de Beer, N. Kardjilov, E. Lehmann, Scattering Correction Algorithm for Neutron Radiography and Tomography Tested at Facilities with Different Beam Characteristics, submitted to Elsevier Science, 2005.

[20] G. Matthess, Die Beschaffenheit des Grundwassers, Lehrbuch der Hydrogeologie, Borntraeger Verlag Berlin, 3. Auflage, 1994.

[21] K. Harris, L. Woolf, Temperature and Volume Dependence of the Viscosity of Water and Heavy Water at Low Temperatures, Journal of Chemical and Engineerig Data, 49(4), 2004, 1064–1069.

[22] IAPWS Release on Surface Tension of Heavy Water Substance, issued by the International Association for the Properties of Water and Steam, 1994

[23] M. Stampanoni, G. Borchert, P. Wyss, R. Abela, B. Patterson, S. Hunt, D. Vermeulen, P. Rüegsegger, High resolution X-ray detector for synchrotron-based microtomography, Nuclear Instruments and Methods in Physics Research A, 491, 2002, 291–301.

[24] A. Carminati, A. Kaestner, R. Hassanein, P. Vontobel, H. Flühler, Infiltration through series of soil aggregates, Resubmitted after minor revisions to Advances in Water Resources, 2006.

[25] N. Ursino, T. Gimmi, Combined effect of heterogeneity, anisotropy and saturation on steady state flow and transport: Structure recognition and numerical simulation, Water Resources Research, 40, 2004, 291–301.

[26] I. Neuweiler, M. Vasin, Upscaling methods for unsaturated flow in media with connected flow paths, Proceedings of the XVI International Conference on Computational Methods in Water Resources, edited by Philip J. Binning Peter Engesgaard, Helge Dahle, George F. Pinder and William G. Gray. Copenhagen, Denmark, June, 2006.
`http://proceedings.cmwr-xvi.org/getFile.py/access?contribId=171&`
`resId=0&materialId=paper&confId=a051`

[27] M. Vasin, I. Neuweiler, P. Lehmann, R. Hassanein, A. Kaestner, Drainage in heterogeneous sand columns with different geometric structures, to be submitted to Advances in Water Resources.

[28] V. McLane (Ed.), Data Formats and Procedures for the Evaluated Nuclear Data File, ENDF-6, ENDF-102, Brookhaven National Laboratory, April 2001.

[29] IDL, Interactive Data Language, RSI, Research Systems Inc, Boulder, Colorado, USA.

Curriculum Vitae

1966   Born in Interlaken, Switzerland (June, 14$^{\text{th}}$)

1973 – 1979 Primary school, Frauenfeld

1979 – 1981 Kantonsschule, Frauenfeld

1981 – 1987 Gymnasium St. Antonius, Appenzell
       Matura Typus B (Latin)

1988 – 1993 Studies of physics, ETH Zurich
       Diploma thesis in the general theory of relativity:
       Evolution of Spherical Pressureless Collapse Models, supervisor
       Prof. Dr. Christian Schmid

1993 – 2000 Teacher of physics and mathematics, Gymnasium St. Antonius,
       Appenzell

2000 – 2003 Software engineer, hmi informatik ag, Zurich

2003 – 2006 PhD student at the Institute of Terrestrial Ecology, ETH Zurich
       and the Neutron Imaging and Activation Group, PSI Villigen.
       Correction Methods for the Quantitative Evaluation of Thermal
       Neutron Tomography, supervisor Prof. Dr. Hannes Flühler